NASA SP-89

OBSERVATIONS FROM THE NIMBUS I METEOROLOGICAL SATELLITE

NATIONAL AERONAUTICS AND SPACE ADMINSTRATION

NASA SP-89

OBSERVATIONS FROM THE NIMBUS I METEOROLOGICAL SATELLITE

Six papers presented by Goddard Space Flight Center personnel at the western annual meeting of the American Geophysical Union, Seattle, Washington, December 29, 1964

Prepared by Goddard Space Flight Center

Scientific and Technical Information Division 1965
NATIONAL AERONAUTICS AND SPACE ADMINISTRATION
Washington, D.C.

For sale by the Clearinghouse for Federal Scientific and Technical Information
Springfield, Virginia 22151 – Price $1.00

FOREWORD

The first photographs of the earth's surface and of large-scale weather systems taken from orbital altitudes have revealed a great deal of new knowledge merely because large-scale phenomena which had never been observed in their entirety were now brought within the scope of one single observation. These findings stem from a series of TIROS (Television and Infrared Observation Satellites) launched at the rate of about two per year since April 1960. TIROS were primarily intended to serve the operational needs of the meteorologist in the detection and tracking of storms, frontal systems and similar phenomena by means of the cloud patterns associated with these weather features. Space-borne observations of weather have also contributed to fundamental meteorological research. Nimbus I, the first of NASA's "second generation" meteorological satellites, has further advanced the potential application of such observations to meteorological research and to other fields of geophysics. The Nimbus I system proved to be an excellent tool for the remote observation of meteorological and geophysical parameters for several reasons; A sun synchronous, nearly polar orbit, a fully earth oriented, amply powered spacecraft, a set of improved and directly transmitting television cameras and a newly developed high resolution infrared radiometer.

This special report contains six articles dealing with the preliminary evaluation of the data obtained from Nimbus I. These articles were originally presented as individual papers at the Western National Meeting of the American Geophysical Union in Seattle, Washington on 29 December 1964. Since each intended to present in its own field a "first look" at the success of Nimbus I, we felt it worthwhile to collect these articles in a single volume such as this to record comprehensively some examples of meteorological and geophysical applications which we were able to derive from the early Nimbus observations.

W. Nordberg
Head, Physics Branch
Aeronomy and Meteorology Division
Goddard Space Flight Center

Page intentionally left blank

CONTENTS

THE NIMBUS I FLIGHT

Wilbur B. Huston* and Harry Press†

INTRODUCTION

Nimbus I was successfully launched by a Thor/Agena launch vehicle from the Western Test Range (WTR) at Vandenberg Air Force Base on August 28, 1964. The flight marked the first in NASA's advanced series of meteorological satellites. The purpose of this paper is (1) to describe the Nimbus spacecraft and the Nimbus systems, (2) to describe the meteorological sensors carried on this flight, and (3) to define the scope, characteristics, and limitations of the meteorological data collected. This paper will serve as an introduction and background for the more detailed and specific papers which follow and which deal with the meteorological significance of the data obtained from this flight.

NIMBUS PROGRAM

The Nimbus program is a meteorological research and development program of the National Aeronautics and Space Administration. The program involves the flight of a series of large, amply powered, earth stabilized, omnibus spacecraft which are to be launched in relatively low altitude (500-750 nautical miles) near-polar orbits. This orbital choice permits full earth coverage and data collection on a daily basis. The spacecraft and supporting ground complex are configured to facilitate real-time data collection, processing, and application. Subsequent flights will utilize the same basic spacecraft, with an expanding set of advanced meteorological sensors, which are currently under development by NASA and by the scientific community.

THE SPACECRAFT

Figure 1 shows the Nimbus I spacecraft in flight configuration. The spacecraft is roughly ten feet tall from the base of the sensory ring to the top of the command antenna. The weight at launch was 832 pounds. The spacecraft consists of three major elements: the solar paddles which are 8 feet by 3 feet, and provide the basic electric power supply; the upper hexagonal package which contains the complete attitude stabilization and control system for the spacecraft; and finally, the lower sensory ring which consists of a 54-inch diameter toroidal structure. This torus contains eighteen standard-size bays which house the major electronic elements of the spacecraft. Large and bulky elements such as cameras and tape recorders are mounted in the open center portion of the torus.

*Deputy Nimbus Project Manager, GSFC.
†Nimbus Project Manager, GSFC.

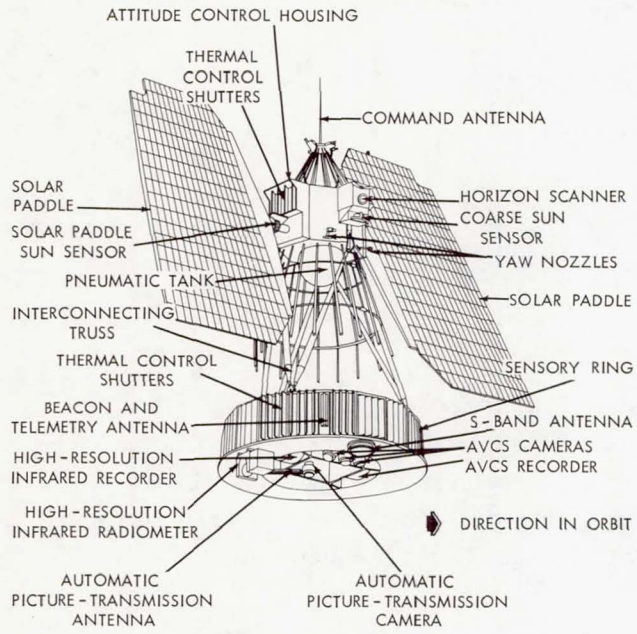

Figure 1—Nimbus I spacecraft.

Solar paddles provide 450 watts under full solar illumination. The attitude control system houses a solar array drive which can provide rotation of the paddles about the pitch axis of the spacecraft. The attitude control system is capable of keeping the spacecraft pointed towards the earth with a pointing accuracy in all three axes of better than one degree on a large part of the mission. In addition, the spacecraft rotational rates are extremely slow, less than 0.05 degrees per second, and well within the requirements for picture taking. The basic spacecraft also contains a command system and a housekeeping telemetry system (4000 data points per minute) for monitoring the engineering performance of the spacecraft in orbit. These housekeeping data include spacecraft attitude error measurements which are required for the interpretation and accurate earth positioning of the sensory data. To provide an optimum thermal environment for the many electronic and solid state devices (4000 transistors, 6000 diodes), thermal control shutters were provided which maintain the temperature of all components at 25°C ± 3° at all times.

The spacecraft carried three meteorological sensors located on the sensory ring as shown in Figure 1. The largest, the *advanced vidicon camera system* (AVCS) was designed to meet the needs of the national meteorological services for global weather data, especially cloud cover. The data are stored on board in a 1200-foot magnetic tape recorder and are played back on command to either of two command and data acquisition sites which are linked to the Goddard Space Flight Center at Greenbelt, Maryland and to the National Weather Satellite Center at Suitland, Maryland by wide-band communication links.

The *automatic picture transmission system* (APTS) provided similar cloud mapping photographs of somewhat lesser resolution to local weather users who employed a simple inexpensive ground station (References 1 and 2) developed as part of the Nimbus program. Some 65 of these stations were in operation throughout the world by the U. S. Weather Bureau (USWB), the Air Weather Service, the U. S. Navy, U. S. Army, national weather services of many countries, and some private users who built their own stations using the design data in Reference 1. Pictures are transmitted continuously during satellite day, the spacecraft command at the local APT stations is not required.

Both camera systems provided pictures taken in daylight. At nighttime the *high resolution infrared radiometer* (HRIR) system provided a continuous scan of the earth to detect emitted thermal radiation. These data are stored on tape in the spacecraft and read out on command over the S-band data link at the same time as the AVCS pictures are read out over this link at the *command and data acquisition* (CDA) sites.

The communication and data handling aspects of the Nimbus system are discussed in more detail in Reference 3; the spacecraft development and qualification are described in Reference 4. Since sensory system development and data characteristics are intimately related to the choice of the desired Nimbus orbit and to the actual orbit achieved, some description of both is indicated prior to a more detailed description of the sensory systems.

THE NIMBUS ORBIT

The design orbit of the Nimbus system - circular, sun-synchronous high-noon (Figure 2) - was chosen to take advantage of the precessional moments induced on the orbit plane of a satellite by the equatorial bulge of the earth. For an orbit of a given semimajor axis and eccentricity, an inclination angle with respect to the equator can be found such that the precession rate of the orbit plane just matches the average rotational rate of the earth about the sun, 0.9856 degrees per day (Reference 1).

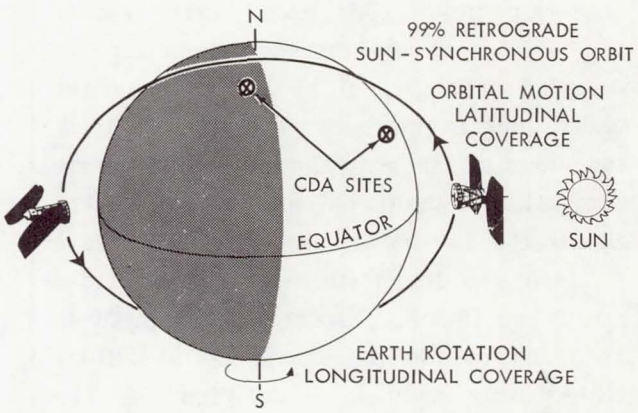

Figure 2—The high-noon sun-synchronous orbit for meteorological satellites.

On the basis of the resolution and coverage constraints imposed by the optical sensor, a circular orbit at an altitude of 500 nautical miles (576 statute miles or 929 kilometers) was chosen for Nimbus I. At that altitude, the required inclination angle to maintain synchronism between the precession of the orbit plane and the mean motion of the sun in right ascension, is 99.05 degrees.

The time of liftoff and thus of injection into orbit, was chosen so that the angle between the orbit plane and the earth-sun line would be small, establishing a "high-noon" orbit. This choice coupled with sun synchronism made all northbound equator crossings occur near local noon, and southbound crossings near local midnight.

Because of an undetected leak in the Agena fuel transfer equipment at the WTR launch pad, approximately 40 pounds of fuel were not loaded as planned, and the desired circular orbit was not obtained. A comparison of the desired and actual orbits is shown in Figure 3. Apogee altitude was within two nautical miles of the desired value, but a short second burn of the Agena resulted in a velocity deficiency which caused the elliptic orbit. Perigee was located initially 20 degrees above the equator on the dark or nighttime portion of the orbit. Northward motion of the agrument of perigee at the rate of 3.1 degrees/day resulted in a drift of the low portion of the orbit toward the command and data acquisition (CDA) station near Fairbanks, Alaska, with a consequent reduction in the duration of passes and of the time available for data readout. As a result, not all data recorded on the spacecraft could be read out and there were gaps in the sensory data coverage for this reason.

SENSORY DATA

Advanced Vidicon Camera System

Each of the three especially developed television cameras in the AVCS has a square field of view of 37 degrees. The central camera points straight down toward the center of the earth; the side cameras are oriented at angles of 35 degrees from the nadir, thus having a two-degree overlap at the sides of the central picture. The earth projection of the three-camera field of view illustrated in the top portion of Figure 4 would at the design altitude have provided nearly continental coverage. The pictures recorded by the three cameras are illustrated in the lower portion of Figure 4. The grid lines shown are written over the pictures by a computer tied into the AVCS ground station. They are computed on the basis of the spacecraft ephemeris, and the time of shutter opening as recorded on the picture timing channel. The grid lines are plotted at two degree intervals; the latitude and longitude legend, also written on the picture by the computer, identifies the intersection shown by the arrow. North and south latitude is distinguished by the letter N; the longitude given by the final three digits of the six-digit field is expressed in degrees east of Greenwich.

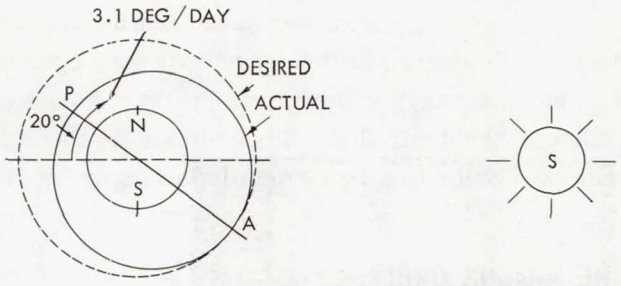

	DESIRED	ACTUAL
ORBIT (MI)	576	579 - 263
(KM)	929	932 - 423
PERIOD (MIN)	103.5	98.7
HIGH NOON	±8°	-8.1°
SUN SYNC. (DEG/MO)	±2.3	+3.3
ORBITS/DAY	13.9	14.7
BLIND ORBITS/DAY	2 - 3	2 - 7

Figure 3—The Nimbus I orbit.

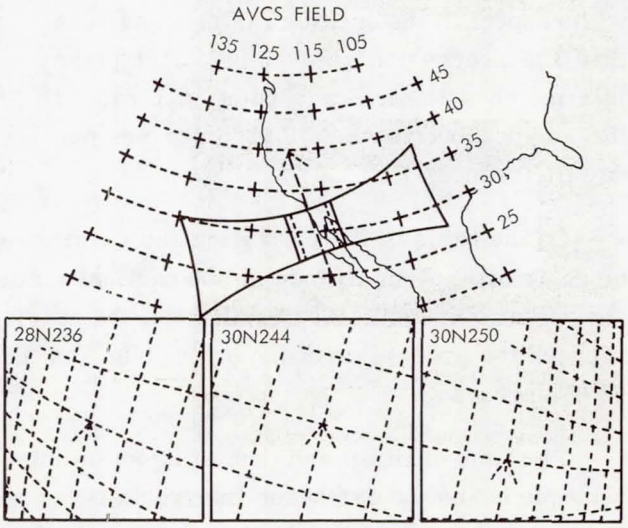

Figure 4—The field of view of the advanced vidicon camera system (AVCS).

An example of a strip of AVCS pictures is shown in Figure 5. Each set of picture triplets has been mosaiced; the gaps between successive triplets result from the lower than design altitude in the elliptic orbit. These pictures, which were recorded over the Nile valley and Eastern Mediterranean on September 16, 1964, were transmitted from the spacecraft tape recorder over the S-band data link to the ground station in Alaska, where they were relayed simultaneously over two 48-kilocycle extremely high quality data links to the Nimbus Data Center at Greenbelt, Md. and the USWB National Weather Satellite Center. As a consequence of the real-time data handling capability of the Nimbus data system, the pictures were available for meteorological use within one hour of the time they were taken. The mosaic of Figure 6 includes only six triplets; a normal set taken from South Pole to North Pole on the daylight portion of the orbit includes 33 triplets taken at 91-second intervals. With 800 lines on the TV raster, the ground resolution at the subsatellite point is better than one-half mile. The wealth of detail

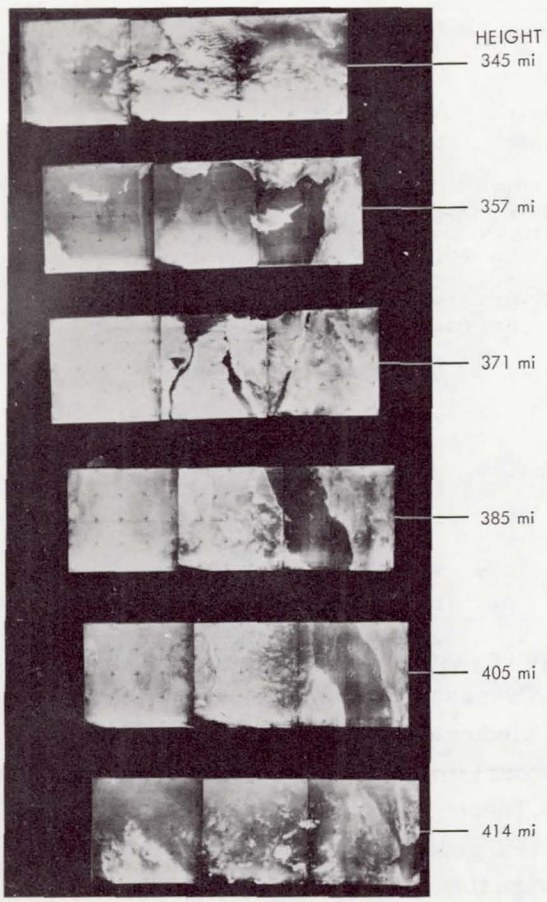

Figure 5—A mosaic strip from the advanced vidicon camera system.

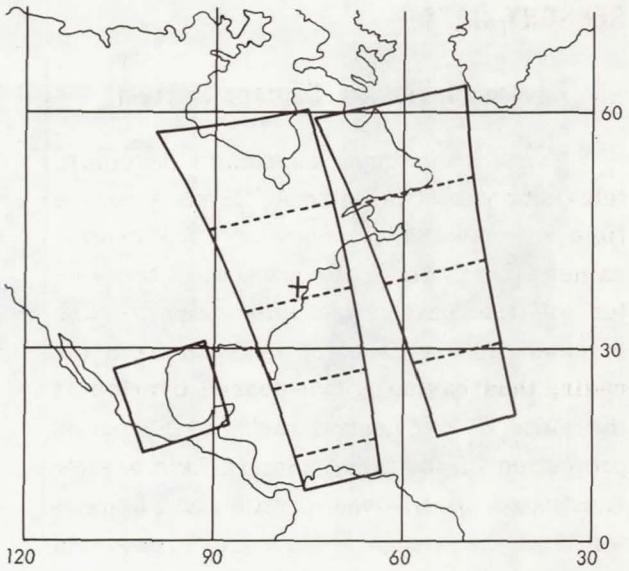

Figure 6—One-day coverage of a representative APT ground station.

in the AVCS pictures, detail in clouds, detail in ice areas and sand areas, detail in geologic formations, of snow cover in mountain areas, all provide a challenging and rewarding reservoir of data which will be of undoubted value to specialized studies yet to be performed.

The single TV camera of the APT system is similar to the AVCS camera, with the exception of a wide-angle lens (108°) and a polystyrene layer which provides storage of the picture image while the vidicon is scanned in the readout cycle. Four line per second readout of the 800-line raster occupies 200 seconds of the 208 seconds between pictures. The APTS transmissions from the spacecraft in the 136-megacycle band are received by a simple ground station and facsimile machine.

The APTS system, announced to the meteorological community in 1962, was developed especially for the Nimbus program by the Aeronomy and Meteorology Division of GSFC, under contracts with the Radio Corporation of America, and Fairchild Stratos, Inc. A first flight test was provided by the TIROS VIII satellite in 1963. Over 60 ground stations have reported reception of APTS data from Nimbus I. These stations, operated by the USWB, the military weather services, various European weather services, and by private users, were uniformity enthusiastic about the quality of the local cloud cover data received, and its ready applicability to local forecast requirements. The camera was designed for coverage of an area 1050 × 1050 nautical miles from the design altitude, with a 300-mile overlap in the north-south direction. At one station pictures were normally received from the overhead pass, and from the previous and the following passes. The coverage obtained in one day at one station is shown in Figure 7.

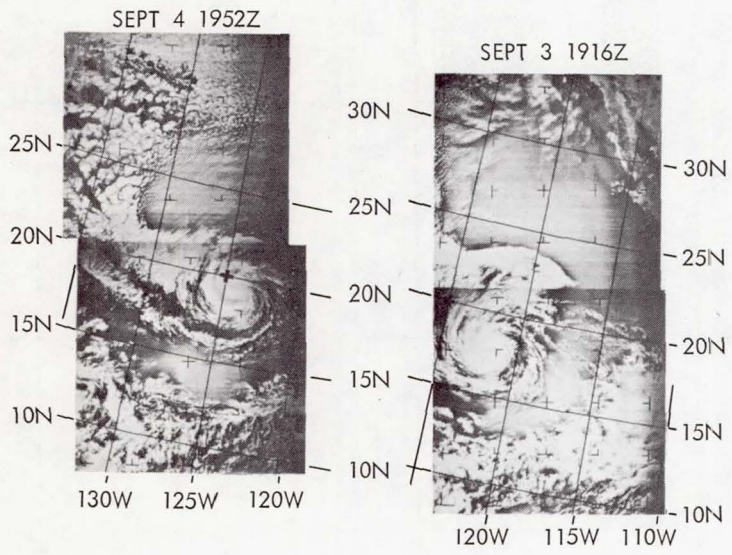

Figure 7—The development of a typical storm as recorded at an APT station 1000 miles from the storm center.

Nine complete and one partial picture can provide very nearly continental coverage. Direct photos of the Caribbean hurricane zone were available in the Washington area at noon each day during the satellite lifetime. Considering the average speed of weather systems as they move during their lifecycle, the APTS coverage of 1500 miles radius provides an exceedingly valuable tool for the local forecaster in even the areas of dense weather stations, as in the Eastern United States. More isolated forecasters reported that the pictures provided information on the location of weather fronts and storm systems not available in any other way.

Unlike the AVCS pictures, the APTS pictures require manual gridding by the user. The gridding process is both quick and straightforward. When use is made of the aids developed for this purpose by the Air Weather Service, precomputed grids are provided for a range of altitudes at 50-kilometer intervals about the design orbital altitude, and for nominal latitudes at 10-degree intervals from the equator to the poles. These grids are adjusted to the 10 inch $\times$ 10 inch frame size of the facsimile machine in the APT ground station. Their use in connection with the spacecraft ephemeris data provided through the meteorological teletype net permits a choice of grids applicable to the time of the start of transmission of each received picture. An example given in Figure 7 illustrates the development and movement of tropical storm Tillie, west of Baja, California on September 3 and 4. These pictures were recorded at the NASA APT station at Pt. Mugu, California. This station, located at 34°N, 119°W was approximately 1000 miles from the storm center on September 3. Based on the demonstrated success on Nimbus I, the automatic picture transmission system has been adopted as one of the basic camera systems for the TIROS operational system (TOS) series of satellites developed by NASA for the U. S. Weather Bureau to meet the interim national requirements for an operational meteorological satellite system.

High Resolution Infrared Radiometer (HRIR)

The key element of the HRIR system, described in detail in a subsequent paper in this volume, is a scanning radiometer which senses infrared radiation at a wavelength of about 4 microns. The radiometer scans a strip perpendicular to the orbital path. The width of the scan strip is about 5 nautical miles at the subsatellite point and increases at the horizon, as illustrated in Figure 8. The radiometer signal, recorded on a spacecraft tape recorder, is

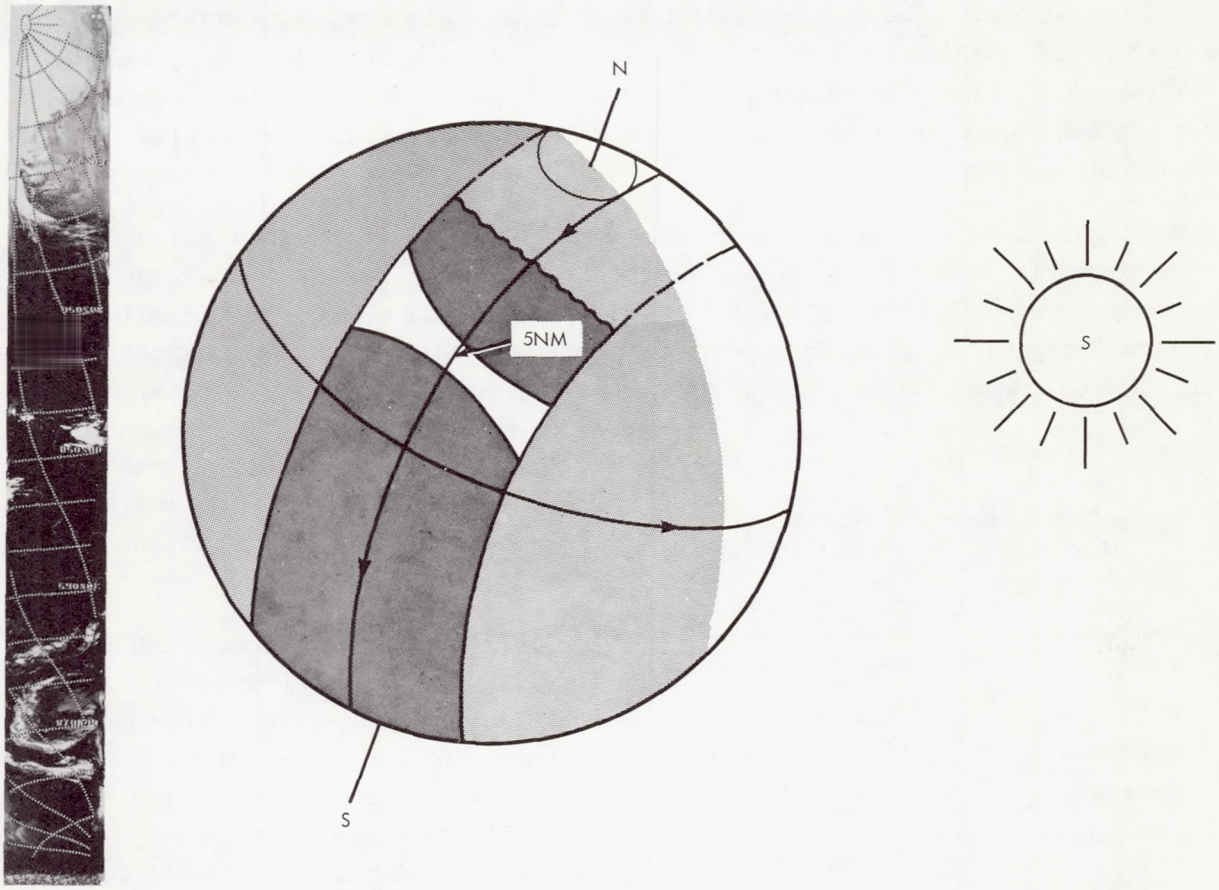

Figure 8—The earth path of the field of the Nimbus high resolution infrared radiometer.

read out upon ground command at the CDA stations. Like AVCS, it is relayed to Washington where the radiometer signal is reconstituted in a facsimile recorder and a picture is formed. The pictorial strip records, which cover a region from the North to the South Poles on the nighttime side of the earth, are gridded automatically, an example of which is shown on the left in Figure 8.

The HRIR for the first time provided accurate, instantaneous pictorial temperature mapping of the earth and of cloud tops. Some initial studies demonstrating the data are reported subsequently in this volume as well as in Reference 2.

The HRIR experiment with its slow-response sensor and the repetitive scan pattern depends heavily on the spacecraft attitude control system. This three-axis earth stabilization system provides the stable platform essential for the automatic reconstitution of the scans to permit a high resolution pictorial presentation of the sensed information.

PERFORMANCE SUMMARY

On September 23, 1964, after 26 days of operation, one of the few electromechanical subsystems on the spacecraft, the solar array drive, jammed and the paddle drive system which

keeps the solar array oriented to the sun failed. Since the solar array stuck in the satellite morning sunrise position, some solar power was received, but not enough to supply the spacecraft with adequate power to operate even the essential spacecraft systems (altitude control, telemetry and command). After seven orbits, battery discharge reached a point where attitude control and telemetry failed.

During the 26 days of operation there were a total of 379 orbits, 125 of which were blind in that spacecraft command was not feasible at either CDA site. With the design orbit only, two passes a day would have been blind, thus 73 of the blind orbits (18%) are chargeable to the eccentric orbit. Of the 254 orbits on which data could theoretically have been obtained, some were missed because of short acquisition times, others because of a conservative doctrine which dictated the turn-off of sensory systems when spacecraft operational problems were encountered. The extent of the data obtained and presently on file at GSFC is shown in Table I.

Table I

Performance Summary of the Nimbus I Spacecraft.
(August 28 - September 23, 1964)

	Orbits	Pictures
Total	379	-
Blind	125	-
AVCS Data	190	12100
HRIR Data	178	6000
APT Data	171	1930

AVCS data were received on 190 orbits. The total of 12,100 pictures which resulted from these 190 orbits indicates that complete coverage (100 pictures per orbit) was not obtained; again a consequence of the elliptical orbit. The count of APT pictures represents those made at stations under NASA control, and for which tapes suitable for reproduction are available. A total count of pictures including all cooperating stations is not available.

Table II

Data Formats Available for the
Nimbus Sensory Systems.

AVCS & HRIR

- Daily Log and Coverage Maps
- Negative Film
- Positive Contact Prints
- Selected 8 x 10 Prints

HRIR

- Digital Magnetic Tape (7090 Compatible)
- Analog Magnetic Tape

APT

- Daily Coverage Maps
- Magnetic Tapes
- Selected 8 x 8 Facsimile Photos

Catalogs of the Nimbus I sensory data are being prepared in order to make the data more readily available to the scientific community (References 5 and 6). The scope of the cataloging effort, and the formats in which data can be made available are summarized in Table II. Daily log and coverage maps of the AVCS and HRIR data designed for ready reference, are contained in these catalogs. Sample catalog pages are shown in Figures 9 and 10 and in Table III.

FUTURE PLANS

Future Nimbus spacecraft provide the opportunity to fly further, more advanced meteorological experiments. The broadest possible participation by the general scientific community is sought in the development of such experiments. The second spacecraft of the series, designated

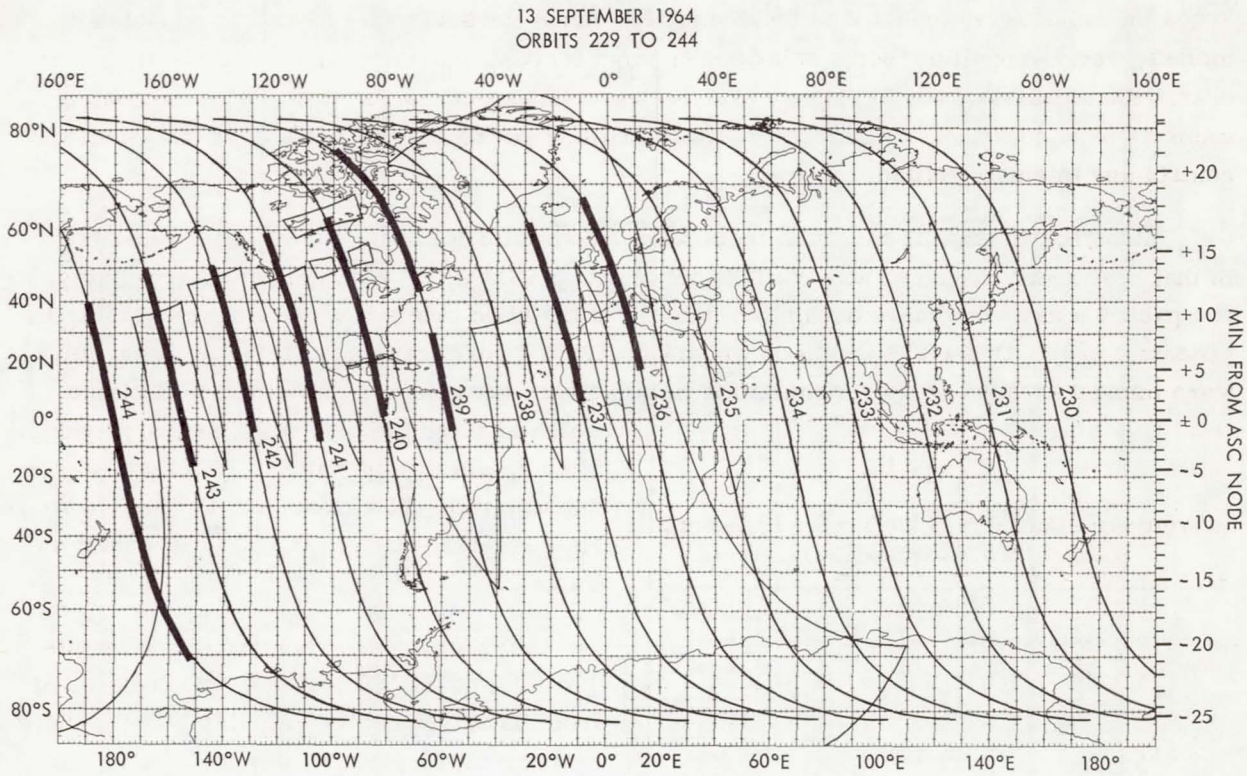

Figure 9—Sample daily coverage map from the AVCS data catalog-equatorial projection.

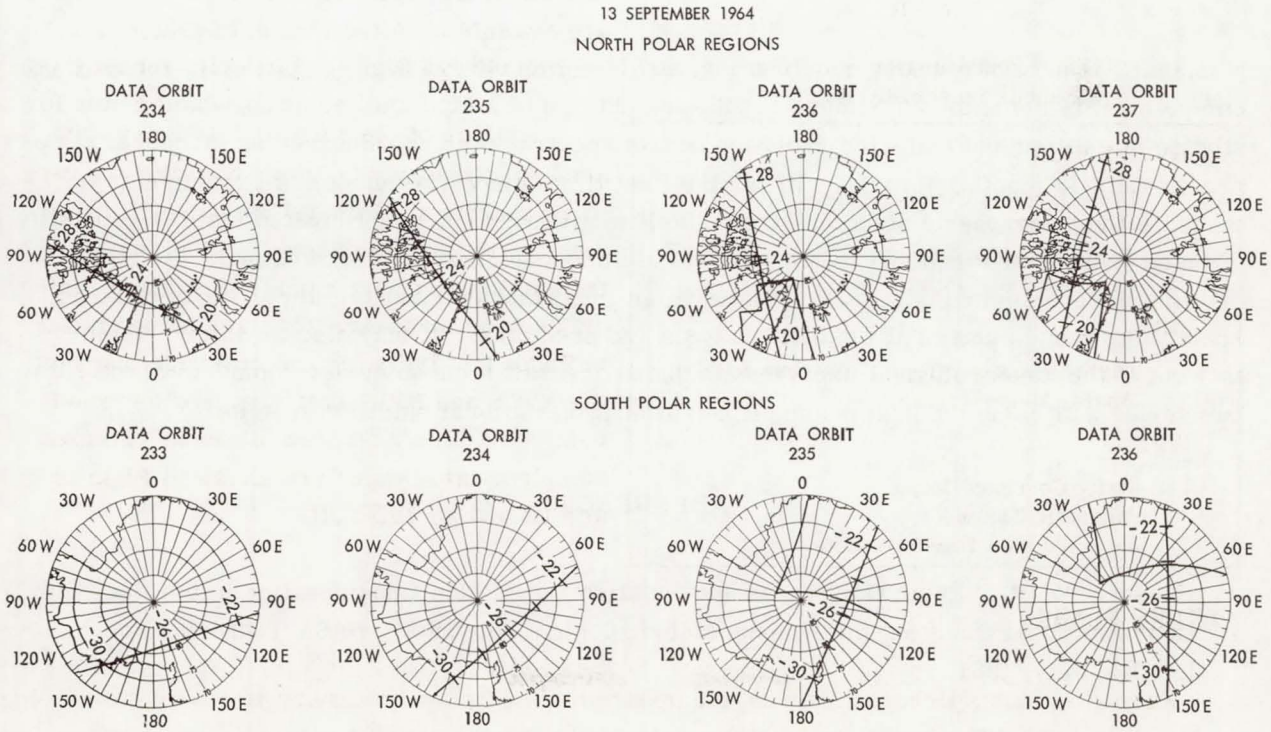

Figure 10—Sample daily coverage map from the AVCS data catalog-polar projection.

Table III

Sample Log Sheet and Index of AVCS Pictures.

DATA ORBIT 210/211
DATE 11 September 1964
ASC. NODE 17 29 49 UT
87.90 W LONG.

CATALOGUE NUMBER	INDEX FRAME	INDEX TIME (UT)	MIN FROM ASC NODE	HEIGHT (KM)	SUN ANGLE	CAM	GEOGRAPHIC FEATURES	METEOROLOGICAL CONTENTS
1-212-60583	1	17 51 45	+21.9	481	12	1		
	1					2	ARCTIC ICE	APPARENT CLOUDS
	1					3		
2-211-60578	2	17 47 12	+17.4	529	29	1		
	2					2		MOSTLY CUFM
	2					3		
3-211-60578	3	17 45 41	+15.9	549	35	1		
	3					2		
	3					3		
4-211-60578	4	17 44 10	+14.4	569	41	1	Saskatchewan, Last Mountain Lake	
	4					2	Saskatchewan, Last Mountain Lake	
	4					3	Lakes Winnipegosis, Manitoba & Dauphin	
5-211-60578	5	17 42 39	+12.8	590	47	1	Yellowstone River	
	5					2	Garrison Reservoir	FRONTAL BANDS
	5					3	Lake Superior	
6-211-60578	6	17 41 08	+11.3	612	52	1		
	6					2		HURRICANE DORA - W. EDGE
	6					3		Frontal Bands
7-211-60578	7	17 39 37	+ 9.8	635	58	1		Cu & Cb Over Gulf States
	7					2		
	7					3		
8-211-60578	8	17 38 06	+ 8.3	658	63	1	S. Texas	
	8					2	Texas - Louisiana Gulf Cst.	
	8					3		
9-211-60578	9	17 36 35	+ 6.8	682	69	1	Mexico Gulf Cst., Lake Madre	
	9					2		
	9					3		
10-211-60578	10	17 35 04	+ 5.3	706	74	1	S. Mexico	
	10					2	Terminos Lagoon	CUFM
	10					3	Yucatan Pen.	Some Cb
11-211-60578	11	17 33 33	+ 3.7	730	79	1		
	11					2	Guatemala - El Salvador Cst.	
	11					3	Honduras & Nicaragua	
12-211-60578	12	17 32 02	+ 2.2	754	83	1		
	12					2		ITC
	12					3	Costa Rica & Panama	
13-211-60578	13	17 30 31	+ 0.7	778	84	1		
	13					2	SOUTH AMERICA	
	13					3	W. Cst.	
14-211-60578	14	17 29 00	- 0.8	801	82	1	Snow on Andes Mts.	
	14					2		CUFM
	14					3		Cellular Field over Water Extending to Cst.
15-211-60578	15	17 27 29	- 2.3	823	77	1		
	15					2		

Nimbus C, is presently under construction, and is scheduled for flight in 1966. Its sensory complement is the same as Nimbus I, with the addition of a Medium Resolution Radiometer for studies of emitted and reflected radiation in five spectral regions. Succeeding launches, at approximately 18 month intervals, will for the first time, employ a number of experiments to measure the atmospheric structure from satellite attitudes. It is anticipated that the capability of these spacecraft for global measurements of atmospheric structure, will make the stabilized orbiting meteorological observation platform an important element in future efforts of large scale, long range numerical weather analysis and prediction. It may also be safely assumed that out of the meteorological experiments and spacecraft technology developments of the Nimbus series will come the next phase of the national operational satellite system.

REFERENCES

1. Bandeen, W. R., "Earth Oblateness and Relative Sun Motion Consideration in the Determination of an Ideal Orbit for the Nimbus Meteorological Satellite," NASA Technical Note D-1045, July, 1961.

2. Stampfl, R. A., and Press, H., "Nimbus Spacecraft System," *Aerospace Engineering* 21(7): 17-28, July 1962.

3. Fujita, T., and Bandeen, W., "Resolution of the Nimbus High Resolution Radiometer," SMRT Research Paper, No. 40, February, 1965.

4. Stampfl, R. A., The Nimbus spacecraft and its communication system, Goddard Space Flight Center Document X-650-65-75, March, 1965.

5. Staff Members, "Nimbus I Users' Catalog: AVCS and APT," Goddard Space Flight Center, March, 1965.

6. Staff Members, "Nimbus I High Resolution Radiation Data Catalog and Users' Manual," Goddard Space Flight Center, January, 1965.

Page intentionally left blank

THE HIGH RESOLUTION INFRARED RADIOMETER (HRIR) EXPERIMENT

L. L. Foshee, I. L. Goldberg
and C. E. Catoe

INTRODUCTION

The Nimbus High Resolution Infrared Radiometer (HRIR) was designed to perform two major functions: first, to map the earth's cloud cover at night to complement the television coverage during the daytime portion of the orbit. Second, to measure the temperatures of cloud tops and terrain features. Nimbus is an earth-oriented satellite which travels in a high-noon, near-polar orbit. The HRIR is mounted at the bottom of the spacecraft so that it has an unobstructed view of the earth. During the 25 days of Nimbus I operation, data for about 50 percent of all nighttime orbits were obtained, each one covering a region from horizon to horizon in width and ranging from North Pole to South Pole. Because the radiometer operates in the 3.4 to 4.2-micron region, measurements taken during the daytime do not reveal true surface temperatures: This is because of reflected solar radiation which is added to the emitted surface radiation. However, reflected sunlight in this spectral region does not saturate the radiometer output and usable, though poorer quality, pictures can be made.

THE HIGH RESOLUTION INFRARED RADIOMETER

The single-channel scanning radiometer, built by ITT Industrial Laboratories, is shown in Figure 1. It contains a lead selenide (PbSe) photoconductive cell which is radiation cooled to -75°C and operates in the 3.4- to 4.2-micron "window" region. The white collars shown in the figure are sunshields to prevent solar radiation from entering the radiometer during spacecraft sunrise and sunset. The scan mirror is located between the sunshields. The cylindrical projection at one end contains the motor which drives both the scan mirror and the chopper. The front of the rectangular pyramid which is part of the radiative cooling assembly can be seen. The electronics are located around this pyramid. The radiometer, which weighs 11.3 pounds and consumes 4 watts of power, can measure

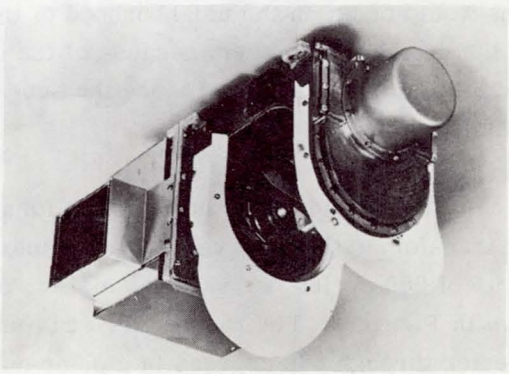

Figure 1—Nimbus I high resolution infrared radiometer.

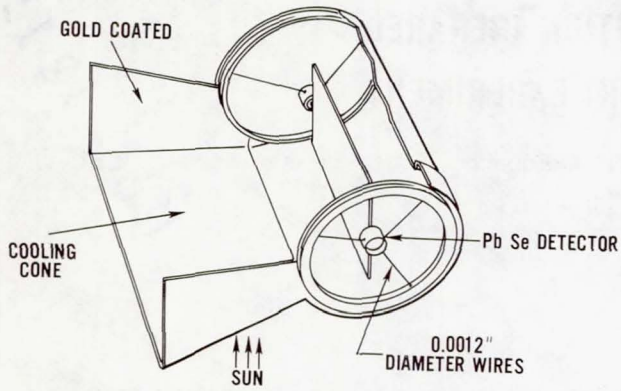

Figure 2—Radiative cooling system for the HRIR lead selenide detector.

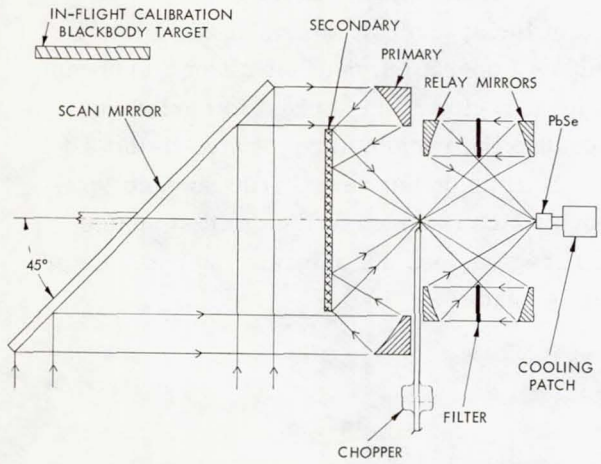

Figure 3—Schematic of the HRIR optical system.

radiance temperatures between 210°K and 330°K with a noise-equivalent temperature difference of 1°C for a 250°K background. The radiative cooling system is shown in Figure 2. Cooling is accomplished by means of a black cooling patch at the bottom of a highly reflective gold-coated pyramid. The pyramid is oriented to view cold space during the entire orbit and the patch is suspended by thin wires to reduce heat conduction from the housing. The detector is connected to the cooling patch by a high thermal conductance transfer bar.

The radiometer has an instantaneous field of view of about 1/2 degree, which at an altitude of 925 kilometers corresponds to a subsatellite ground resolution of 8 kilometers. Figure 3 illustrates the HRIR optical system. The scan mirror is inclined 45 degrees to the axis of rotation which is coincident with the spacecraft velocity vector. The optical scan path thus lies in a plane perpendicular to the orbital motion. The radiation reflected from the scan mirror is chopped at the focus of a 4-inch f/1 modified Cassegrainian telescope. It is then refocused at the detector by means of a reflective relay which contains the 3.4 to 4.2-micron filter. The scan rate of 44.7 revolutions per minute was chosen so that contiguous scanning would occur in the neighborhood of the subsatellite track, with increasing overlap toward the horizon. However, because of the unintentional eccentric orbit of Nimbus I, gaps of about 5 kilometers occurred along the subsatellite track at perigee. Toward apogee the gaps decreased to zero.

In contrast to television, no image is formed within the radiometer; the HRIR sensor merely transforms the received radiation into an electrical (voltage) output with an information bandwidth of 280 cycles per second. A trace of a portion of an actual Nimbus I analog record is shown in Figure 4. The radiometer scan mirror continuously rotates the field of view of the detector through 360 degrees in a plane normal to the spacecraft velocity vector. The detector views the in-flight blackbody calibration target (which is a part of the radiometer housing), outerspace, earth, outerspace, and returns again to intercept the in-flight blackbody target. The space and housing-viewed parts of the scan, which can be identified without difficulty, serve as part of the in-flight check of calibration. Information on housing temperatures, which are monitored by thermistors, are telemetered to the ground stations and for calibration

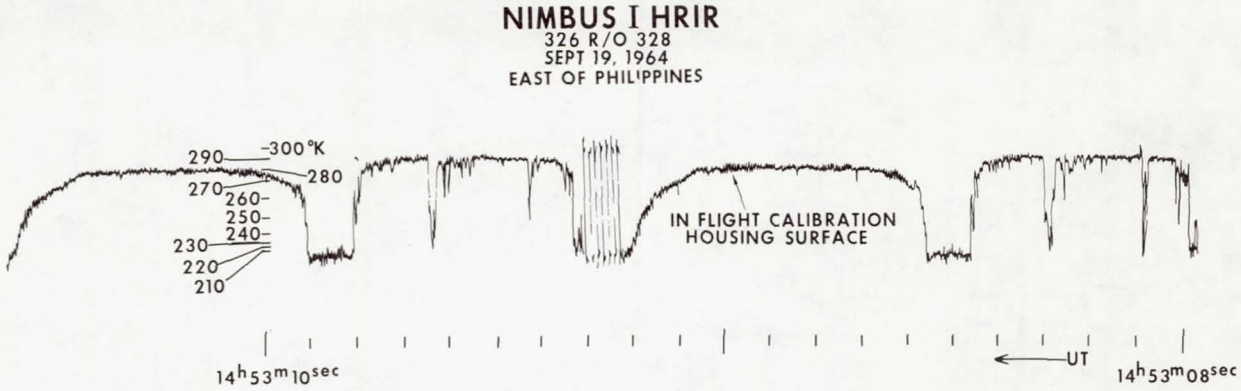

Figure 4—Portion of an analog record showing nearly two HRIR scan cycles.

purposes are constantly compared with the temperatures obtained from the radiometer housing scan. The space scan serves as the zero reference point. During the space sweep a permanent magnet on the scan mirror gear triggers an electronic gate and a multivibrator so that the seven pulses shown in Figure 4 are generated. These pulses are used to synchronize automatic display equipment on the ground.

HRIR SUBSYSTEM

A simplified block diagram of the HRIR subsystem is shown in Figure 5. The radiometer video output (0 to -6.4 v dc) is fed to an FM modulator which converts the radiometer voltage to frequency modulated signals (8.25 to 10 kcps) that are recorded on one track of a 4-track tape recorder. Simultaneously, 10-kilocycle AM timing signals from the Nimbus spacecraft clock are placed on a second track on the tape. When these two tracks are completely recorded, the direction of the tape travel is automatically reversed and the recording continues on the other two tracks. The recorder accepts data at a tape speed of 3.75 inches per second and upon command plays back all four channels simultaneously at 30 inches per second. The 8 to 1 playback speedup causes a directly proportional increase in the FM signal frequencies (66 to 80 kc). The four tape recorder outputs (two video and two time code) are fed into the four channels of the HRIR multiplexer where each channel is translated to its assigned position in the HRIR subsystem base band (i.e., 55 to 69.5 kc and 127.5 to 141.5 kc for the two video channels). The four channels are combined in an adder circuit to produce a composite HRIR subsystem base band which is fed to the Advanced Vidicon Camera System (AVCS) multiplexer. In the AVCS multiplexer, the HRIR subsystem base band is combined with the AVCS base band and the composite signal is fed to the Nimbus S-band transmitter for transmission to the Command Data Acquisition (CDA) station.

At the CDA station, the HRIR information is demultiplexed and recorded on magnetic tape. It is then transmitted to the Goddard Space Flight Center, where the FM signal is demodulated, synchronized and displayed by a Westrex photofacsimile recorder. The facsimile recorder converts the radiometer output electrical signals into a continuous strip picture, line by line, on 70 mm film. Blanking circuits in the Westrex recorder reject unwanted sections of each line scan; only the earth scan and, for calibration purposes, very small portions of the space

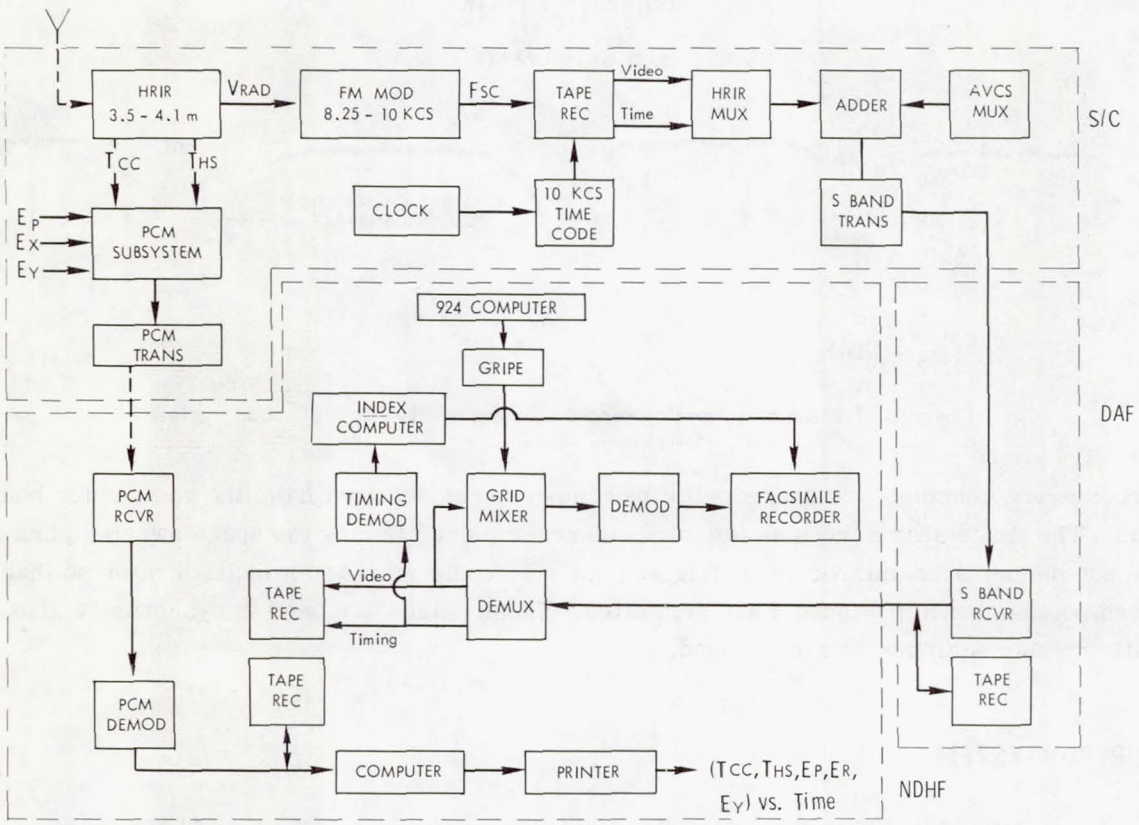

Figure 5—Simplified block diagram of the HRIR subsystem.

scan and the radiometer housing scan are recorded on the film strip. The processing time between spacecraft playback command and display for one full nighttime orbit is about 30 minutes.

Although the signal level resolution in the pictorial display is an order of magnitude poorer than in the corresponding analog record, the picture is invaluable for recognition and qualitative analysis of the meteorological information. Only 10 signal levels can be displayed in the greyshades of the picture while about 100 levels are contained in the original signal. An illustration is given in Figure 6a, which is a reproduction of a selected portion of the photofacsimile display of an orbital strip covered by the HRIR near midnight on September 20, 1964 ranging from about the equator at the bottom to the Gulf of Alaska at the top. The blackness of each picture element varies directly with the intensity of the radiation sensed by the radiometer. The warm waters of the tropical Pacific Ocean can be recognized in the very dark area near the bottom in contrast to the somewhat cooler temperatures of the North Pacific Ocean shown by the dark patches just north and south of 40°N. The "medium gray" around 30°N is a large mass of very low altitude stratus clouds or fog. The string of small, very bright (cold) spots near 137°W and 38° to 40°N indicate isolated, very high altitude cumulus clouds relating to thunderstorm activity.

A much more quantitative picture results when the original analog signals are digitized with full fidelity and the digital data are processed by an IBM 7094 computer where calibration and geographic referencing is applied automatically. Extracts of such automatic,

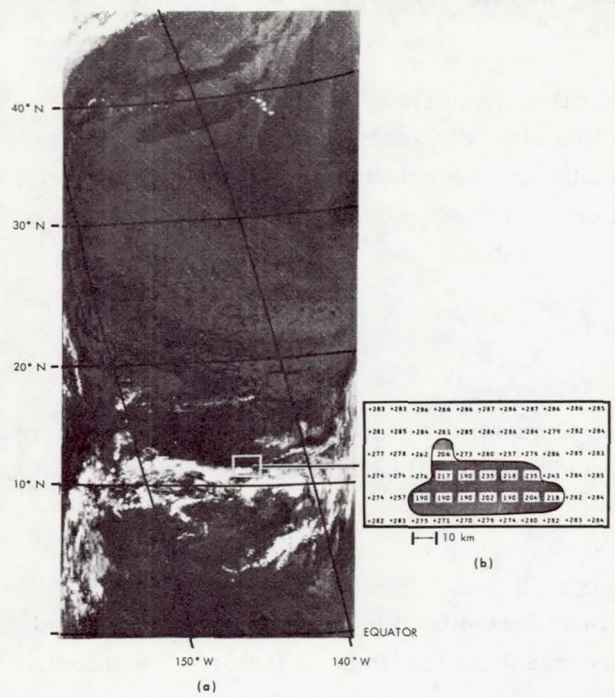

Figure 6—A positive print of nighttime HRIR data: (a) Pictorial presentation of cloud and water temperatures over the North Pacific measured by the HRIR at midnight on 20 September 1964. (Dark shades are warm, white shades are cold.) (b) Automatically produced digital map of cloud surface temperatures.

numeric presentations are shown in Figure 6b. The very highest cloud in Figure 6a, located in the Intertropical Convergence Zone (11.5° -12°N and 145-146°W), is characterized by extremely low radiation intensities corresponding to blackbody temperatures of 190°K near the center of the cloud top (Figure 6b).

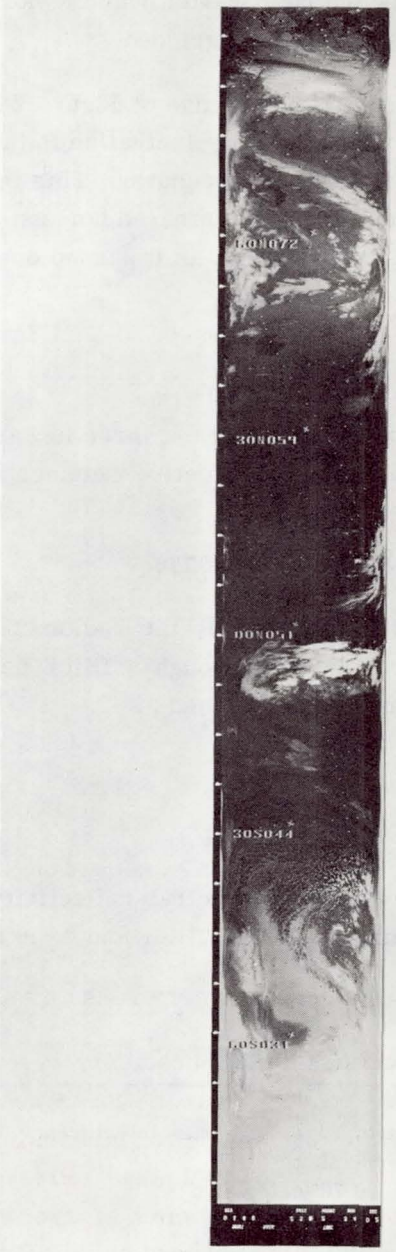

Figure 7—An example of automatic gridded HRIR data.

The absolute and relative geographical locations of each picture element scanned by the radiometer strongly depends on the stability of the spacecraft. The Nimbus controls system has a demonstrated pointing accuracy of about 1 degree for the spacecraft axis. A pointing error of 1 degree corresponds to a subsatellite error of 16 km in the location of a picture element for an altitude of 925 km. On a global basis, this is an acceptable error for meteorological analysis. Automatic gridding of the data is done by the same equipment used to grid the television pictures. For pictorial presentation grid points are computed with a CDC 924 computer and added to the HRIR data in analog form. Each grid point is converted from coordinates of latitude and longitude to coordinates compatible with the electrical signals, i.e., line number and mirror angle. An example of automatic gridding is shown in Figure 7. Because of the

large distortions and poorer data near the horizon, only the central 107-degree portion (as measured at the satellite) is gridded.

The line along the right edge of Figure 7 indicates the horizon seen by the radiometer. There is a clear indication of fluctuation in that line after the spacecraft had passed over the high tropical clouds near the equator. This indicates the disturbances which the high altitude, cold clouds presented to the infrared horizon scanner of the Nimbus controls system causing the spacecraft to roll slightly as it passed over the equator.

CALIBRATION

In discussing the calibration, three fundamental quantities must be defined: the effective spectral response, ϕ_λ, the effective radiance, $\bar{N}$, and the equivalent blackbody temperature, T_{BB}.

Effective Spectral Response

The radiation received by the radiometer is reflected by five front-surface aluminized mirrors and transmitted through a filter before reaching the PbSe detector. The effective spectral response, ϕ_λ, is defined as

$$\phi_\lambda = R_\lambda f_\lambda A_\lambda \quad , \tag{1}$$

where R_λ is the combined spectral reflectivity of all five front-surface mirrors, f_λ is the spectral transmittance of the filter and A_λ is the spectral absorptivity of the detector.

Table I

Nimbus I HRIR Optics.

Filter
Type: Multilayer wide band-pass interference
Substrate: Germanium
Transmission: 0.76 (calculated)
Scan Mirror
Type: Evaporated SiO over hard-coated aluminum
Substrate: Aluminum
Reflectivity: 0.96 (estimated)
Cassegrainian telescope (primary and secondary)
Type: Front-surface Al with SiO protective coating
Substrate: Glass
Relay Optics
Type: Front-surface gold coated with SiO protective coatings
Substrate: Glass
Reflectivity of the 4 mirror surfaces (Cassegrainian telescope and relay optics): 0.92 (estimated)

In the actual computation of ϕ_λ, the spectral reflectivities, R_λ, of all mirrored surfaces were assumed to be constant over the pass band of the filter and hence were normalized to unity. The resultant equation used in computing ϕ_λ, therefore, was

$$\phi_\lambda = f_\lambda A_\lambda \quad . \tag{2}$$

The materials used in the optics are given in Table I. The function f_λ was taken from International Telephone and Telegraph Laboratories measurements of the filter used in HRIR Unit F-2, the instrument flown on Nimbus I and the function A_λ was taken from several typical laboratory curves of PbSe detectors. The effective spectral response is given in Figure 8.

Effective Radiance

Because of its narrow field of view, the HRIR essentially measures beam radiation or radiance toward the satellite along the optical axis. In the preflight laboratory calibration, the field of view of the radiometer was filled by a blackbody target whose temperature could be varied and accurately measured over a range of 190°K to 340°K. From the temperature of the blackbody target, T_{BB}, the spectral radiance of the target is determined by the Planck function B_λ. The integration of this function over the effective spectral response, ϕ_λ, yields that portion of the radiance of the target to which the radiometer responds, the "effective radiance, $\bar{N}$," given by

$$\bar{N} = \int_0^\infty B_\lambda (T_{BB})\, \phi_\lambda \, d\lambda \, . \qquad (3)$$

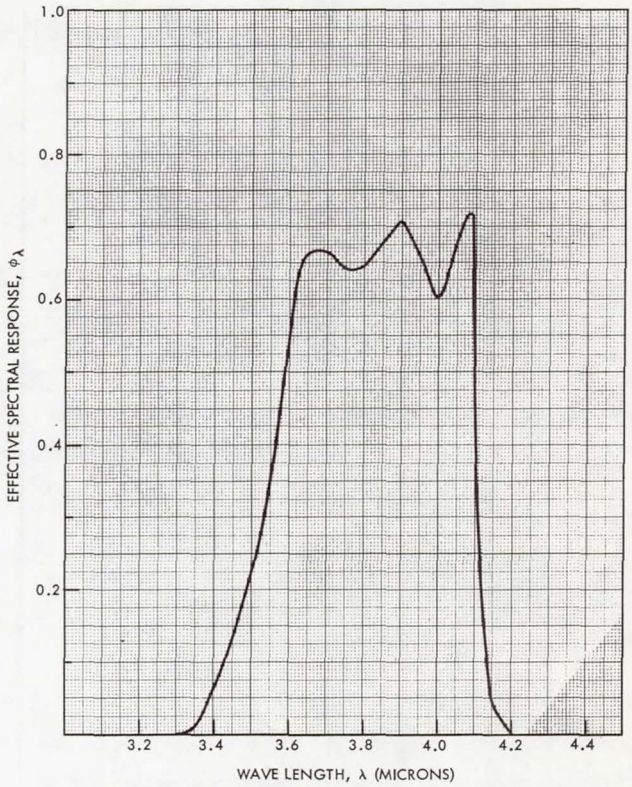

Figure 8—The effective spectral response of the HRIR versus wavelength.

Equivalent Blackbody Temperature

The effective radiance to which the orbiting radiometer responds may be expressed by

$$\bar{N} = \int_0^\infty N_\lambda \, \phi_\lambda \, d\lambda \quad , \qquad (4)$$

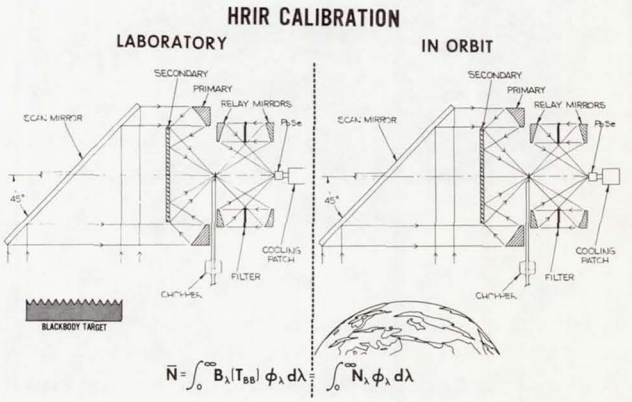

Figure 9—Schematic illustration of the relationships between laboratory calibration and T_{BB} measurements made in orbit.

where N_λ is the spectral radiance in the direction of the satellite from the earth and its atmosphere. It is convenient to express the measurement from orbit in terms of an equivalent temperature of a blackbody filling the field of view which would cause the same response from the radiometer. From Equations 3 and 4 it is seen that this "equivalent blackbody temperature" corresponds to the target temperature, T_{BB}, of the blackbody used in the laboratory calibration. This relationship is expressed schematically in Figure 9. Therefore, the radiometer measurements can be expressed either as values of effective radiance, $\bar{N}$, or as equivalent blackbody temperatures, T_{BB}. The $\bar{N}$ versus T_{BB} function from Equation 3 is given in Figure 10.

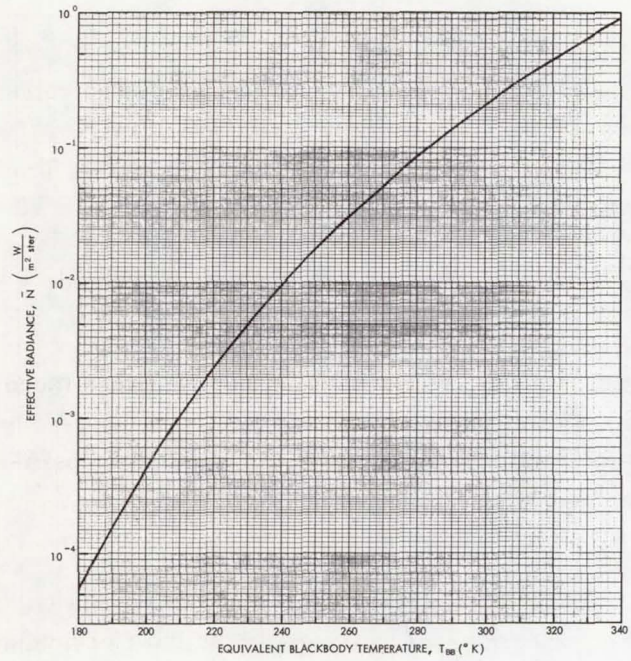

Figure 10—$\bar{N}$ versus T_{BB}.

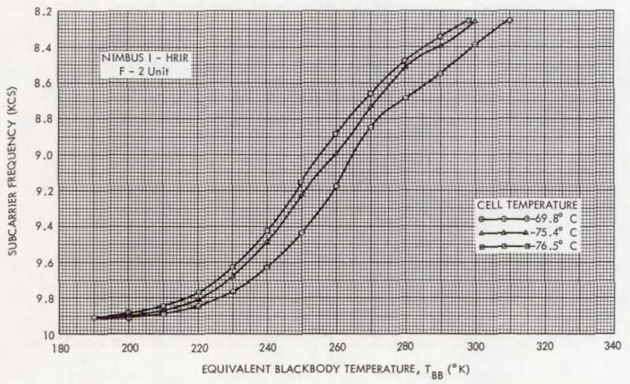

Figure 11—HRIR calibration.

The only independent varying parameter of consequence in the calibration was the cooled PbSe cell temperature. All other temperature and voltage variations were automatically compensated for and/or regulated within very narrow limits. Therefore, separate calibrations were made for several different cell temperatures. The blackbody target temperature, T_{BB}, was varied between 190°K and 340°K in 10°K steps and the radiometer output voltages were recorded for a given cell temperature. Then the PbSe cell was stabilized at a new temperature and the target temperature was cycled again from 190°K to 340°K.

After the radiometer was integrated in the spacecraft and subjected to vacuum-thermal environmental testing, a check of calibration was performed. These data were obtained approximately eight months after the original laboratory calibration of the radiometer. Essentially the same techniques were employed in the calibration check as were used in the original laboratory calibration. The blackbody target temperature was varied from 190°K to 340°K in 20°K steps and the subcarrier frequencies from the FM modulator were recorded on the spacecraft HRIR tape recorder (cf. Figure 5). After one full target temperature cycle, the data were played back through the entire system and transmitted via the S-band transmitter in the spacecraft. The data were received at the ground station, demultiplexed, demodulated and displayed in the form of an analog trace on an oscillographic record, thus simulating as fully as possible, on a system basis, the orbital conditions. Close examination of both sets of calibration data revealed no significant changes over the eight months period during which the radiometer underwent testing and integration with the spacecraft; therefore, we have high confidence in the validity of the calibration. The definitive calibration data for the HRIR F-2 unit which was flown on Nimbus I are shown in Figure 11. Parametric curves for different values of the PbSe cell temperature are given. Values of T_{BB} can be converted to $\bar{N}$ from Figure 10. In orbit the calibration was checked at one target temperature during each scan by means of a blackbody target of known temperature mounted on the upper side of the radiometer (Figure 3).

FLIGHT PERFORMANCE OF THE RADIOMETER

One of the unique features of this experiment was the radiative cooling technique. The cell cooled to its desired temperature of -75°C within less than 3 hours after launch and remained at a satisfactory temperature thereafter. There were no indications of degradation in the gold-coated cell-cooling horn nor was any difficulty experienced in the cell-patch suspension system. The suspension system had been extensively tested prior to launch, having withstood satisfactorily the various types of vibration tests to which the radiometer had been subjected in the test program for some 95 minutes.

The radiometer housing stabilized at its anticipated temperature of 11°C and remained there within 2.5°C throughout its lifetime. The temperature stability of the entire radiometer contributed in large part to the corresponding stability of the PbSe cell temperature. The temperature of the motor end of the casting stayed well above -5°C, which is the lower limit for the successful operation of the motor.

The calibration of the radiometer remained stable throughout its lifetime and there was no discernible degradation of the characteristics of the detector cell, mirrors or the interference filter.

Results have shown that radiance levels corresponding to the equivalent blackbody temperature in the range from 210°K to 320°K were resolved with an accuracy of 2°K or better. Some smoothing of the analog traces of the radiometer signal is required to achieve this accuracy. An arbitrary point measurement taken from the analog trace without smoothing can deviate an additional 2°K due to periodic noise interference induced electronically into the radiometer amplifiers and superimposed on the signal, making the overall uncertainty of a point measurement about ±4°K.

Results from aircraft flights at night with a modified HRIR during January and February 1964 from an altitude of 12 kilometers indicate that stratocumulus and altocumulus cloud equivalent blackbody temperatures were about 2°C cooler than actual cloud temperatures, while ocean equivalent blackbody temperatures were approximately 5°C cooler than measured sea surface temperatures. The overwater flights were made near the Bahamas where the measured water temperature varied between 23°C and 25°C. Data from Nimbus I and calculations by Kunde (see subsequent article) show approximately the same results.

CONCLUSIONS

The Nimbus I High Resolution Infrared Radiometer experiment has extensively mapped infrared radiation emitted during nighttime from the tops of clouds and from land, sea and ice surfaces over the entire world. With a resolution approaching that of TIROS television pictures and with a far simpler scanning geometry than the scanning radiometers previously flown on TIROS, the Nimbus HRIR significantly increased the ability of meteorological satellites to make detailed and accurately placed measurements of emitted radiation and thereby, to infer characteristics of the horizontal and vertical structure of weather systems. In interpreting the photofacsimile data one must initially exert some effort to associate the visible contrasts with

variations in the radiating temperatures of surfaces (and hence their heights and emissivities) instead of variations in the reflectivity of sunlight as in conventional television pictures which the HRIR film strips superficially resemble.

The data from this experiment, in both the photofacsimile format and the digitally processed format, should be of interest not only to the meteorologist as a new tool for operational use and research, but also to the oceanographer, geologist, glaciologist, and other geophysicists in investigating temperature gradients in ocean currents, thermal emission properties of various terrains, the structure and thickness of continental and floating ice in the polar caps, and other geophysical phenomena.

THEORETICAL RELATIONSHIP BETWEEN EQUIVALENT BLACKBODY TEMPERATURES AND SURFACE TEMPERATURES MEASURED BY THE NIMBUS HIGH RESOLUTION INFRARED RADIOMETER

Virgil G. Kunde

INTRODUCTION

In general, radiometric experiments from meteorological satellites have been designed for three basic types of measurements (Reference 1):

1. To map daytime and nighttime surface features and clouds from measurements of radiation emitted by these surfaces through an atmospheric "window."

2. To determine atmospheric structure from measurements made in a spectral region of high atmospheric absorption.

3. To determine the planetary heat balance of the earth from measurements of the incoming solar radiation and the total outgoing long-wave radiation.

Each type of measurement has its associated problems in determining the appropriate meteorological parameter from the radiometric measurement of reflected solar radiation and/or emitted terrestrial radiation. Here we are concerned only with the first type of measurement.

The Nimbus I High Resolution Infrared Radiometer (HRIR) mapped the cloud cover and terrestrial features by measuring their radiating temperatures at night—when there is no solar interference—through an atmospheric window between the 4.26 micron absorption band of carbon dioxide and the 3.17 micron band of water vapor. Because this is a window region, a large fraction of the radiation measured by the radiometer originates from underlying cloud or ground surfaces. For a perfectly clean window region—where there is no atmospheric absorption—all of the measured radiation originates from the surface, and the surface radiating temperature is therefore measured directly. At the other extreme, in a highly absorbing region, all of the surface radiation is absorbed by the atmosphere and, in this case, satellite measurements would not give any indication of the surface radiating temperature. In the range between a perfectly clean window region and a highly absorbing region, the HRIR window region falls very near the perfectly clean window extreme.

The general purpose of this article is to show quantitatively that the overlying atmosphere has little effect on the outgoing radiation observed by the HRIR and that the HRIR measurements, therefore, give a good estimate of the surface temperature. The only atmospheric effect considered here will be atmospheric absorption. The effect of surface emissivity on the observed radiation will also be illustrated since the radiation emitted by the surface depends not only on the true

surface temperature but also on the spectral emissivity of the surface. Therefore, one of the problems associated with determining the true surface temperature from the radiating temperature of the surface is that the surface spectral emissivity must be known. With the computations presented in this article, an attempt will be made to assess the accuracy and validity of

a) HRIR measurement of cloud-top radiating temperatures, where, if the temperature distribution with height is known, the height of the cloud-top can be determined, provided the cloud-top can be adequately defined and,

b) HRIR measurement of ground or ocean radiating temperatures over cloud-free areas.

THE FOUR MICRON "WINDOW" REGION

Before going on to a more detailed discussion of the calculations, a qualitative description of the four micron "window" would seem to be in order. For convenience, we refer to this "window" as the four micron "window" even though it actually extends from about 3.4 to 4.0 microns. The four micron window is shown in Figure 1 where the lower solid line represents an infrared prismatic solar spectrum—a transmission spectrum of the earth's atmosphere with the sun as a source of radiation—taken by Shaw (Reference 2). The upper solid line represents the solar irradiance at the top of the atmosphere assuming the sun radiates as a blackbody at 6,000°K. Because the location of the continuum is not known exactly, the positioning of the solar irradiance curve relative to the solar spectrum is somewhat arbitrary. The darker shaded area represents the solar energy loss, due mainly to molecular absorption, in the earth's atmosphere. The dashed curve of Figure 1 represents the HRIR effective spectral response curve with half power points at 3.55 and 4.10 microns. Qualitatively, Figure 1 shows that the HRIR measurements are made through a fairly clean atmospheric window as the solar spectrum indicates that the transmission through the atmosphere is largest in the region where the HRIR is spectrally sensitive. A slightly cleaner window would result if the short wavelength cutoff of the effective spectral response was sharper, and if the entire effective spectral response curve was shifted slightly to the short wavelength side.

The dominant molecular absorption bands in the four micron region are the overtone parallel $2\nu_2$ vibration-rotation band of H_2O at 3.17 microns and the parallel ν_3 fundamental vibration-rotation band of CO_2 at 4.26 microns. The approximate regions of absorption for these two bands are indicated by the horizontal arrows in Figure 1. Absorption by the isotopic species of carbon dioxide and water vapor also occurs in this region, with the most prominent isotopic band being the ν_1 fundamental of HDO at 3.67 microns. The absorption due to the Q-branch of this band is very evident in the solar spectrum of Figure 1.

Additional molecular absorption in the four micron window occurs because of the minor constituents such as N_2O and CH_4. The wavelength and upper state of the vibrational transitions of the absorption bands due to these minor constituents are also indicated in Figure 1 (Reference 3). These bands have been identified in the solar spectrum, however, not all of them are visible in this particular solar spectrum because the prismatic spectral resolution

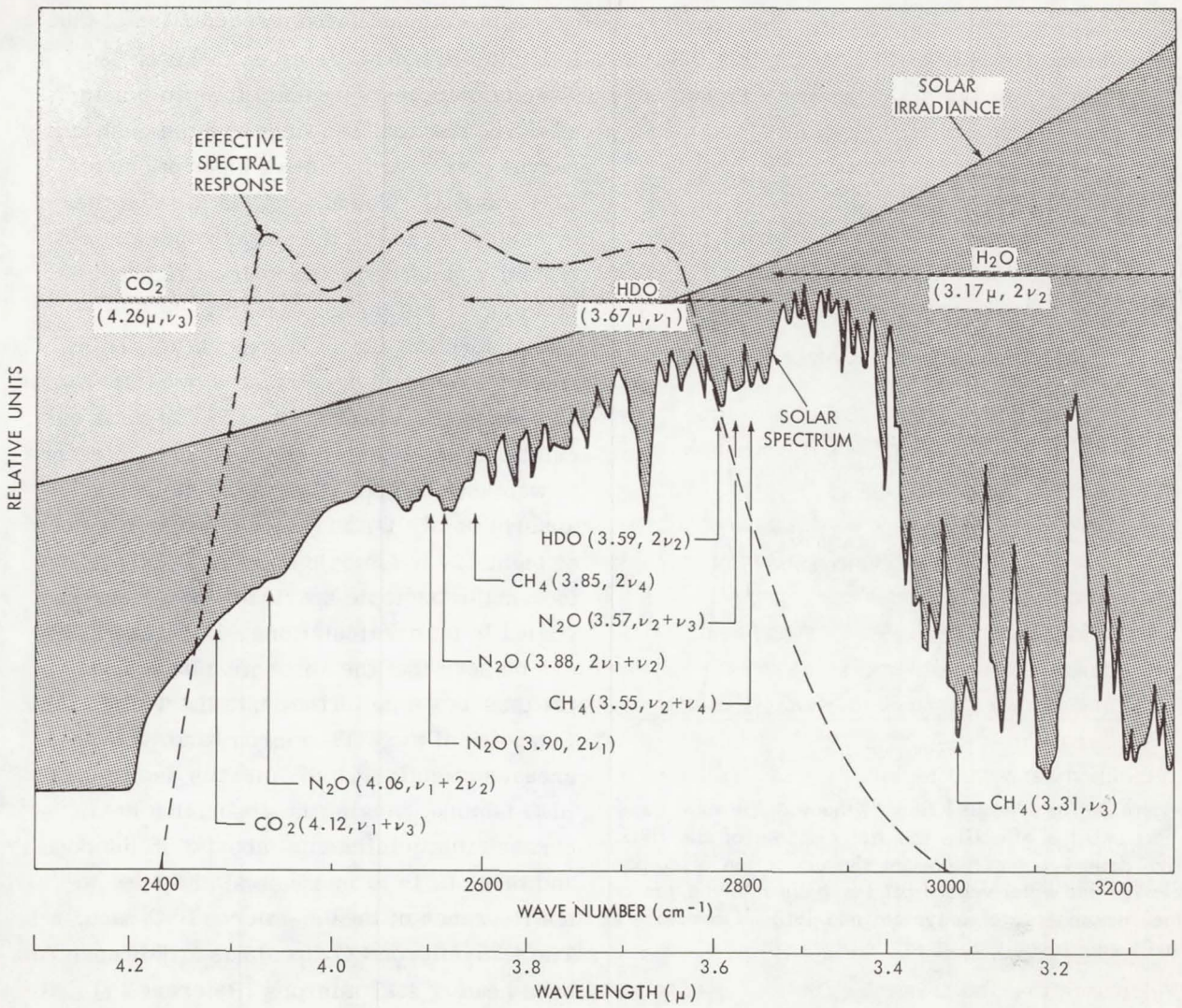

Figure 1—The four micron "window" region. The upper solid curve represents the solar irradiance of a 6,000°K blackbody at the top of the atmosphere and the lower solid curve an infrared prismatic solar spectrum (Reference 2). The darker shaded area represents the solar energy loss, due mainly to molecular absorption, in the earth's atmosphere. The horizontal lines indicate approximately the regions of absorption due to the major absorbing gases. The vertical lines indicate the center of absorption bands due to major constituents (Reference 3). The dashed curve is the effective spectral response of the HRIR.

is not great enough to resolve all the bands. In addition, some of the bands are overshadowed by the strong absorption of H_2O and CO_2.

All of these transitions originate in the ground state with the exception of the N_2O band at 3.88 microns which originates in the ν_2 level. The CO_2 band, at 4.12 microns, is also an upper state band with its lower level being $2\nu_2$. Generally, the minor constituents are considered to be distributed uniformly throughout the atmosphere while H_2O is concentrated mainly at lower altitudes. Thus, while it may be desirable to consider the absorption of the minor constituents at high altitudes, their effect can usually be neglected at low altitudes due to the overshadowing strong absorption by H_2O and CO_2.

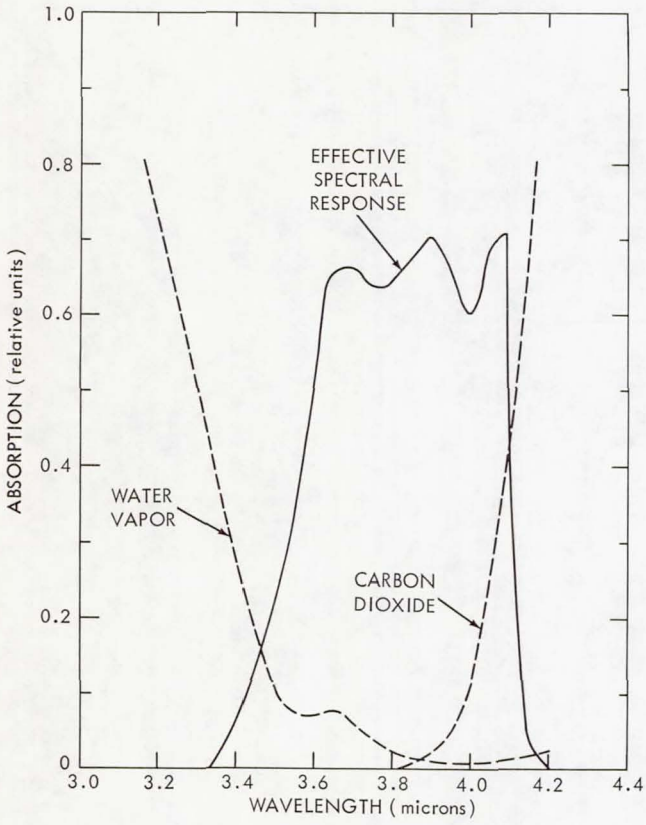

Figure 2—The Nimbus I HRIR "window." The solid curve represents the effective spectral response of the HRIR. The dashed curves represent the absorption of carbon dioxide and water vapor from the ground to the top of the atmosphere for a typical mid-latitude atmosphere and a zenith angle of 0°.

A more quantitative presentation of the four micron window is given in Figure 2. The solid curve represents the radiometer effective spectral response and the dashed curves give representative absorptions for CO_2 and H_2O. The absorption is from the ground to the top of the atmosphere for a typical mid-latitude atmosphere (1 precipitable cm of water) and a zenith angle, 0°. The absorption curves were obtained from transmission tables calculated by Stull, Wyatt and Plass (References 4 and 5). In their calculations, the quasi-random model (Reference 6) was used to approximate the molecular absorption of CO_2 and H_2O. Absorption lines of eight major isotopic species of CO_2 and four major isotopic species of H_2O were included in their calculations. In Figure 2, it can be seen that the absorption by H_2O decreases as we go further into the wing of the P-branch of the 3.17-micron band, then increases slightly at 3.67 microns due to the HDO isotope. Again, the absorption decreases to a minimum at about 3.95 microns and then starts to increase slightly due to the R-branch of the 6.3-micron H_2O band. The 4.26-micron CO_2 band has a R-branch band head at 4.17 microns (Reference 7), therefore, the absorption for wavelengths less than 4.17 microns is due to the wings of strong lines in the R-branch.

In their CO_2 transmission calculation, Stull, Wyatt and Plass (Reference 5) have used the Benedict modification of the Lorentz line shape (Reference 8) to represent the line shape in the wings at distances greater than 2.5 wavenumbers from the line center. For comparison purposes, they have also made calculations at one temperature (300°K) and one pressure (1 atm) for a Lorentz line shape. The comparison of the transmission values for the two different line shapes shows that the Benedict modification gives a substantially higher transmission for long path lengths in window regions. The Benedict modification used by Stull, Wyatt and Plass was determined from experimental data for self-broadened CO_2. Although no detailed calculations exist, there are indications that for foreign-broadened CO_2, which is the condition found in the earth's atmosphere, the form of the Benedict modification may still apply but the correction factors will be substantially different (Reference 8). Thus, it is not known with any certainty which line shape is applicable in the earth's atmosphere. Young (Reference 9) and Drayson (Reference 10), in way of contrast to Stull, Wyatt and Plass, have used the Lorentz line shape for CO_2, deciding there was no justification for using the Benedict modification until experimental

data representative of the earth's atmosphere was available. This problem bears directly on the calculations of the outgoing radiance at the top of the atmosphere in the HRIR window region, since it is in window regions where the transmission differences are most significant.

As transmission tables for CO_2, for the Lorentz line shape, are available for only one temperature and one pressure, it is not possible to compare directly an absorption curve for the Lorentz line shape with the absorption curve of Figure 2 which represents the Benedict modified line shape. However, a comparison of the absorption curves for the Lorentz and Benedict modified line shapes can be made for a temperature of 300°K, a pressure of one atmosphere, and a CO_2 optical path length of 200 cm-atm. This comparison for the four micron window region is shown in Figure 3, where it can be seen that there are very significant differences between the two curves throughout the entire spectral region of interest. The largest difference is about 0.27 at 4 microns. Thus, the variation of transparency of the HRIR window due to the two different line shapes should have a very noticeable effect on the outgoing radiance.

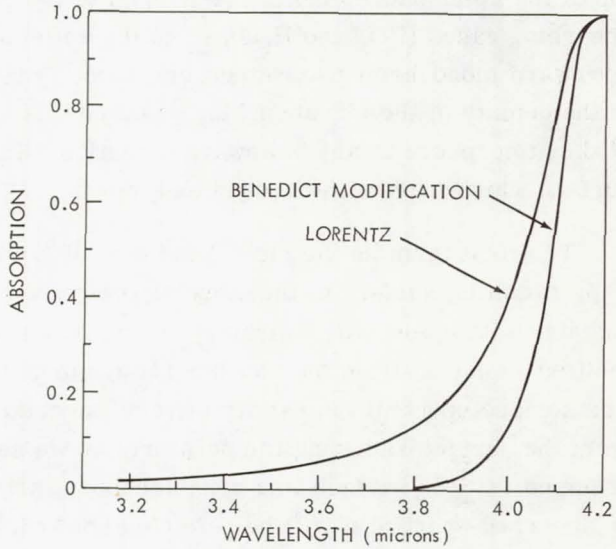

Figure 3—Absorption curves, based on the quasi-random spectral model, for the Lorentz line shape and for the Benedict modification of the Lorentz line shape. The comparison is for a pressure of one atmosphere, a temperature of 300°K and an optical path length of 200 cm-atm, for CO_2.

The calculations of the outgoing radiance, which is discussed in the following section, were made using the Benedict modified line shape transmission values. Comparison calculations using the Lorentz line shape transmission values could not be made because of the unavailability of these transmission values as a function of temperature, pressure, and gas concentration. If these tables were available and if one could eliminate other areas of uncertainty which occur in the determination of the outgoing radiance, than it may be possible to observationally verify one of the line shapes from the HRIR measurements. Because we are working in a fairly clean window, the task of eliminating or at least minimizing the other areas of uncertainty is not necessarily insurmountable.

RADIATIVE TRANSFER EQUATION SOLUTION

The outgoing effective radiance which the HRIR should measure has been calculated theoretically for several model atmospheres using the radiative transfer equation in the form

$$\bar{N}(\ell = 0) = \int_{\lambda=0}^{\lambda=\infty} \phi_\lambda \epsilon_{\lambda_s} B_\lambda(T_s)\, \tau_{\lambda_s}\, d\lambda + \int_{\lambda=0}^{\lambda=\infty} \phi_\lambda r_{\lambda_s} F_{\lambda_s}^{-} \tau_{\lambda_s}\, d\lambda$$

$$+ \int_{\text{Surface}}^{\text{Top}} \int_{\lambda=0}^{\lambda=\infty} \phi_\lambda B_\lambda [T(\ell)] \frac{\partial \tau(\lambda, P, T, \rho_i)}{\partial \ell}\, d\lambda\, d\ell \quad , \qquad (1)$$

where $\bar{N}(\ell = 0)$ is the outgoing effective radiance at the top of the atmosphere and represents the outgoing radiation measured by the HRIR, ϕ_λ is the effective spectral response of the HRIR, ϵ_λ is the spectral emissivity which is considered to be independent of viewing angle, B is the Planck function, τ_λ is the total beam transmission from a given level in the atmosphere to the top of the atmosphere, and is taken equal to the product of the transmissions of the individual absorbing gases (CO_2 and H_2O), r_λ is the reflectivity for a perfectly diffuse reflector, πF_λ^- is the downward monochromatic radiant emittance, λ is wavelength, T is temperature, P is pressure, ρ_i is the density of the i^{th} absorbing gas, and ℓ is geometrical path length measured from the top of the atmosphere in any downward direction. The subscript s represents the lower boundary surface which may be the ground or a cloud.

The first term on the right-hand side of Equation 1 represents the contribution of the underlying radiating surface to the outgoing effective radiance, where it is assumed that the surface radiates with a spectral emissivity which may not be unity. Thus, at a given temperature, the emitted radiation from the non-blackbody surface is less than that from a blackbody surface. The surface spectral emissivity is very important in determining the true surface temperature from the surface radiating temperature, as we shall see in the results. Because it has been assumed that the surface is a non-blackbody, not all of the radiation incident on the surface will be absorbed—part of it will be reflected upward, back into the atmosphere. This component of the outgoing effective radiance is represented by the second term on the right-hand side of Equation 1. The third term represents the contribution of the atmospheric emitting gases to the radiation observed by the HRIR. Because we are in a window region, most of the outgoing radiation is due to the radiating surface, while the atmospheric emission contribution is very small. To anticipate the results somewhat, the surface contributes about 95% and the atmosphere contributes about 5% of the observed radiation. These numbers indicate that the absorption and subsequent re-emission of radiation in the atmosphere is very small, and thus the component of outgoing radiation due to the downward radiation being reflected upward is neglected in the calculations.

Neglecting the second term, the radiative transfer equation (equation 1) takes the form

$$\bar{N}(\ell = 0) = \int_{\lambda=0}^{\lambda=\infty} \phi_\lambda \, \epsilon_{\lambda_s} B_\lambda(T_s) \, \tau_{\lambda_s} \, d\lambda + \int_{\text{Surface}}^{\text{Top}} \int_{\lambda=0}^{\lambda=\infty} \phi_\lambda \, B_\lambda \left[T(\ell)\right] \frac{\partial \tau(\lambda, P, T, \rho_i)}{\partial \ell} \, d\lambda \, d\ell \, . \quad (2)$$

The model atmospheres chosen for the calculations give the temperature and density of the absorbing gases as a function of altitude, h. Given the temperature profile and assuming a surface pressure of 1013.25 mb, the pressure as a function of height is obtained for each model from the hydrostatic equation. If θ, the zenith angle at the ground is specified, the geometry for a concentrically stratified atmosphere gives a relationship between ℓ and h. By using the model atmospheres and the relation between ℓ and h, Equation 2 can be expressed as

$$\bar{N}(\ell = 0, \theta) = \int_{\lambda=0}^{\lambda=\infty} \phi_\lambda \, \epsilon_{\lambda_s} B_\lambda(T_s) \, \tau_{\lambda_s} \, d\lambda + \int_{\text{Surface}}^{\text{Top}} \int_{\lambda=0}^{\lambda=\infty} \phi_\lambda \, B_\lambda(h) \frac{\partial \tau(\lambda, h)}{\partial \ell} \frac{\partial \ell(h, \theta)}{\partial h} \, d\lambda \, dh \, . \quad (3)$$

Defining

$$\psi(h, \theta) = \int_{\lambda=0}^{\lambda=\infty} \phi_\lambda B_\lambda (h) \frac{\partial \tau(\lambda, h)}{\partial \ell} \frac{\partial \ell(h, \theta)}{\partial h} d\lambda \quad , \tag{4}$$

Equation 3 becomes

$$\bar{N}(\ell = 0, \theta) = \int_{\lambda=0}^{\lambda=\infty} \phi_\lambda \epsilon_{\lambda_s} B_\lambda T_s \tau_{\lambda_s} d\lambda + \int_{Surface}^{Top} \psi(h, \theta) dh \quad . \tag{5}$$

The quantity $\psi(h, \theta)$ represents the thermal emission contribution of each atmospheric layer to the observed outgoing radiation. The outgoing, effective radiance at the top of the atmosphere, $\bar{N}(\ell = 0, \theta)$, was then determined for various angles θ, for several model atmospheres from Equation 5. The results of these calculations are expressed in terms of equivalent blackbody temperature (T_{BB}), rather than effective radiance, through the expression

$$\bar{N} = \int_{\lambda=0}^{\lambda=\infty} \phi_\lambda B_\lambda (T_{BB}) d\lambda \quad . \tag{6}$$

The reduction from the non-homogeneous to the homogeneous atmosphere was accomplished by scaling the half-width pressure and temperature dependence of the transmission function into the optical path length, thus allowing a standard transmission function at normal temperature and pressure to be used (Reference 11). The generalized absorption coefficients, which were considered to be temperature independent, were derived from the transmission tables of Wyatt, Stull and Plass (References 4, 5).

The reduced optical path length (u^*) is expressed as

$$u^* = \left(\frac{P}{P_0}\right)^{k_1} \left(\frac{T_0}{T}\right)^{k_2} u, \tag{7}$$

where u is the optical path length, P_0 is standard pressure, T_0 is standard temperature, and k_1 and k_2 are constants. The exponent k_1, varies from 1.0 for non-overlapping lines to 0.5 for heavily overlapping lines. It has been illustrated by Möller (Reference 12), that k_1 is dependent on wavelength, pressure, and on the amount of absorbing gas. For this investigation, k_1 was derived from the transmission data of Wyatt, Stull and Plass (References 4 and 5) for a temperature of 300°K and for pressures of 0.5 and 1.0 atmospheres. The value of k_1 determined for CO_2 was 1.0, independent of optical path length. For H_2O, a mean value of $k_1 = 0.8$ was adopted, as k_1 was found to be extremely dependent on the H_2O optical path length. The exponent k_2, was taken as 0.5 for both H_2O and CO_2. It should be pointed out that the predicted value of the outgoing effective radiance is not very sensitive to the values of k_1 and k_2 because

most of the radiative transfer occurs near the ground, where the (P/P_0) and (T_0/T) ratios are very close to unity.

MODEL ATMOSPHERES

The important properties which distinguish one model atmosphere from another in these calculations are the surface temperature and the total amount of water vapor. Because we are in a window region, the surface temperature is the most influential part of the temperature profile as it essentially produces the outgoing radiation, whereas, the remaining part of the temperature profile has little influence on the outgoing radiation due to the small amount of atmospheric absorption and re-emission. Again, because we are in a window region, it is the total amount of absorbing gas, not the density distribution, which has the largest effect on the outgoing radiation. CO_2 was assumed to be uniform at 0.031% by volume in each model and thus, the total amount of CO_2 was essentially the same in each model (Table I). Therefore, for the atmospheric absorbing gases, it is only the variation of the total amount of H_2O between models that has a varying effect on the outgoing radiation. The model atmospheres were chosen to reflect a representative range of surface temperature and total amount of H_2O.

These models are shown in Figure 4. The left-hand side of Figure 4 presents the temperature as a function of altitude and the right-hand side, the vertical distribution of the mixing

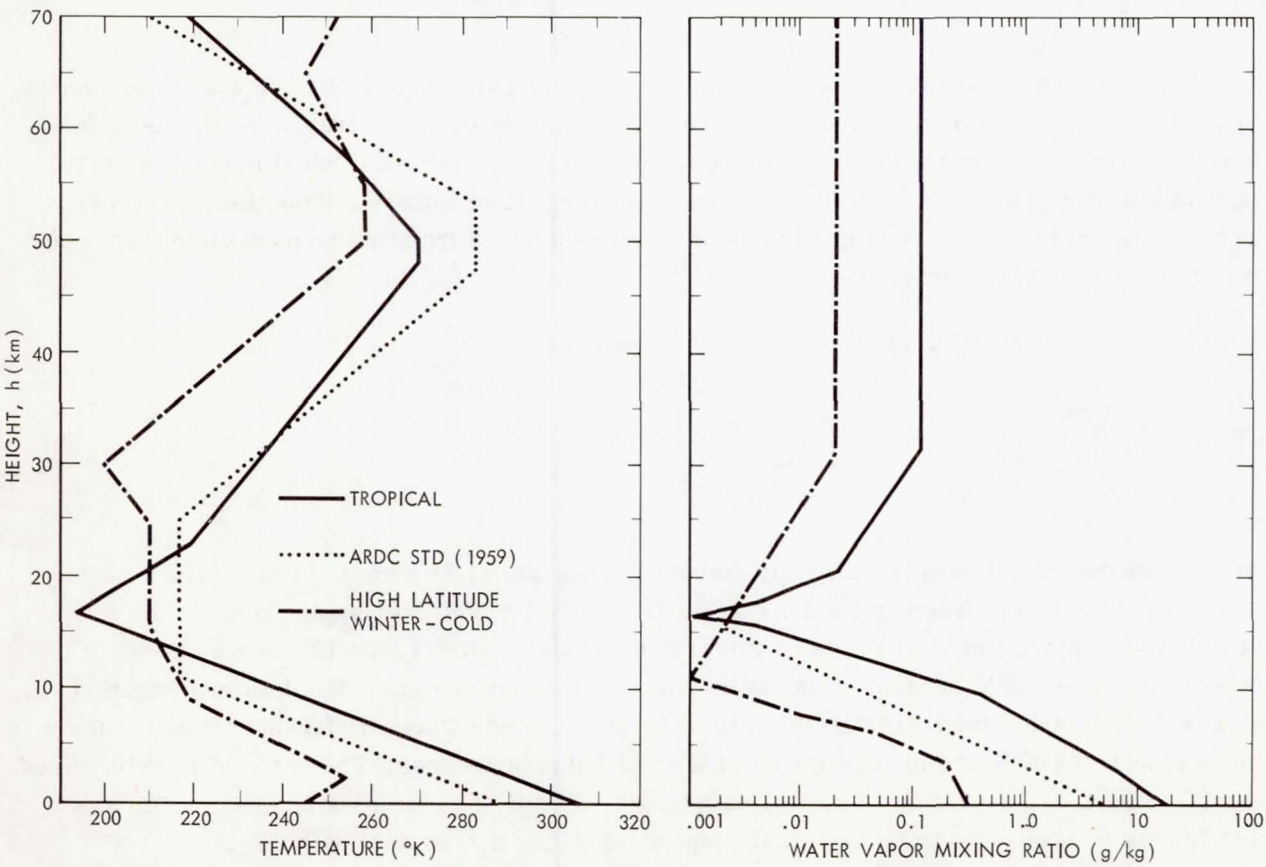

Figure 4—Model atmospheres. The temperature profiles are indicated in the left-hand side of the figure and the water vapor mixing ratio as a function of altitude on the right-hand side.

Table I

Surface Temperatures and Total Gas Content for Model Atmospheres of Figure 4 at Zenith Angle of 0°.

Atmosphere	Surface Temperature (°K)	Carbon Dioxide u(cm-atm)	Water Vapor u(pr-cm)
Tropical	305.0	247.4	4.70
ARDC Std (1959)	288.0	247.3	1.16
High Latitude Winter—Cold	246.5	247.8	0.14

ratio of H_2O. The total amount of H_2O in a vertical column, indicated in Table I, can be obtained by integrating the H_2O mixing ratio profile over altitude. The High Latitude Winter Model (References 13 and 14) represents a case with a low surface temperature of 246.5°K and a low total H_2O content of 0.14 precipitable centimeters (pr-cm); the Tropical Model (Reference 15) a case with a high surface temperature of 305.0°K and a high total H_2O content of 4.70 pr-cm and the ARDC Standard Model (1959) (Reference 15) an intermediate case with a surface temperature of 288.0°K and a total H_2O content of 1.16 pr-cm.

RESULTS

The results of the calculation of the outgoing effective radiance for the model atmospheres of Figure 4 and for several values of the surface emissivity are discussed in this section. It is to be emphasized that these results are for clear sky conditions only and, therefore, are not strictly applicable where partial cloudy conditions exist. In addition, only molecular absorption in the atmosphere has been considered. The effects of high thin cirrus clouds (Reference 16) and/or of extinction and emission by aerosols (References 16 thru 20) have not been taken into account. The difficulties encountered in inferring surface temperature from satellite radiance measurements have been discussed by Wark (Reference 21). A good over-all review of atmospheric radiative processes in the infrared (2 to 5 microns) has been made by the Boeing Company (Reference 22).

In Figure 5, the theoretical surface temperature minus equivalent blackbody temperature differences are given as a function of the zenith angle at the ground for the model atmospheres of Figure 4. The graybody surface emissivity has been taken as unity. The theoretical temperature difference for the High Latitude Winter Model, which had a low total water vapor content and a low surface temperature, is about 0.3°K for zenith angles less than about 75°. Thus, for clear sky conditions and a real atmosphere similar to the High Latitude Winter Model where atmospheric absorption is the only important source of attenuation, the HRIR should measure about 0.3°K lower than the surface radiating temperature. Because the surface emissivity has been assumed to be unity, the surface radiating temperature and the actual surface temperature are equivalent. For the Tropical Model, which had the high total water vapor content and a high surface temperature, the theoretical temperature difference is about 2.3°K for low zenith angles, and increases to about 8.0°K at a zenith angle of 75°. Because of the larger

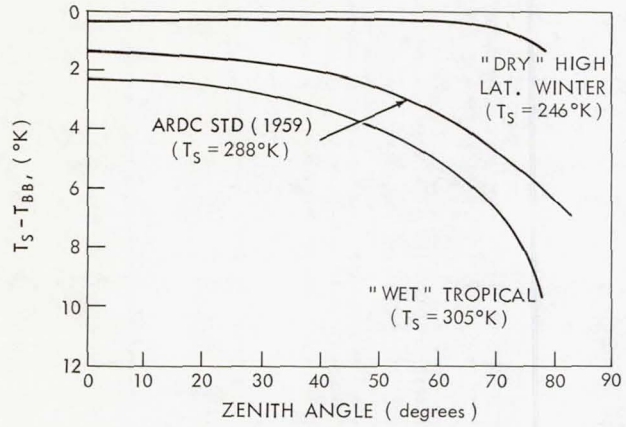

Figure 5—Theoretical surface temperature minus HRIR equivalent blackbody temperature difference as a function of zenith angle for the model atmospheres of Figure 4. A graybody surface emissivity of unity and clear sky conditions have been assumed.

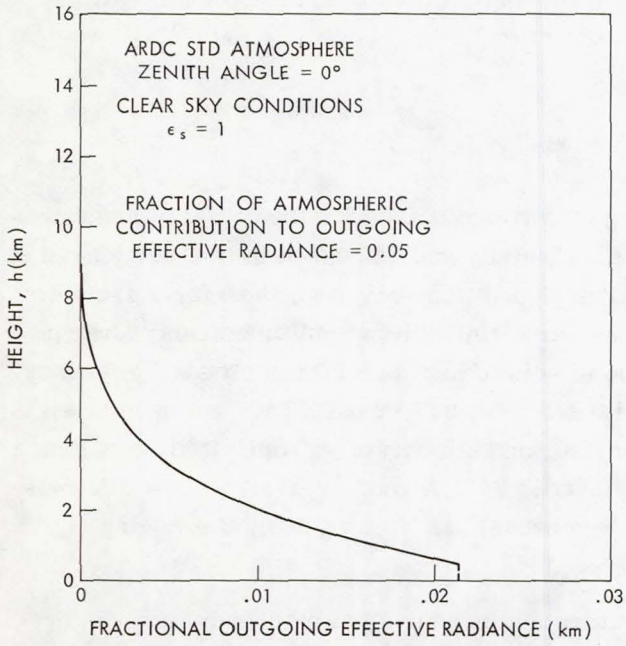

Figure 6—The fractional contribution to the total outgoing effective radiance from each atmospheric layer. The assumed conditions are noted in the upper left-hand corner.

water vapor content, the Tropical Model shows a greater degree of limb-darkening than does the High Latitude Winter Model. Thus, the theoretical calculations predict the HRIR "window" is a very clean "window." This is indicated by the results which show that the observed equivalent blackbody temperature should be within about 2°K of the surface temperature for low zenith angles. How well the observed temperature differences compare with the theoretical temperature differences will be discussed in the following papers.

The vertical distribution of the atmospheric emission is shown in Figure 6 for the ARDC Standard Model (1959) atmosphere, a zenith angle of 0 degrees and a graybody surface emissivity of unity. The abscissa, as determined by the ratio $\psi(h, \theta = 0)/\bar{N}$, represents the fraction of the total observed radiation from an atmospheric layer. For example, the thermal emission of a layer one kilometer thick at a height of one kilometer is about 2% of the total radiation observed by the HRIR, while a layer one kilometer thick at 5 kilometers contributes only about 0.1%. The total observed radiation from the atmosphere is proportional to the area under the curve. In this case, the fraction of the atmospheric contribution to the outgoing effective radiance is about 5%. Thus, most of the radiation observed by the HRIR, about 95%, originates from the ground for the vertical viewing case. As the zenith angle increases to 75°, the ground contribution decreases to about 87% due to the increased atmospheric absorption. The ground contribution for the High Latitude Winter and Tropical Model at low zenith angles is about 98% and 91% of the total observed radiation respectively.

From Figure 6, it can also be seen that for radiating surfaces such as thick opaque clouds at levels above 8 to 10 kilometers, the HRIR equivalent blackbody temperature gives the cloud radiating temperature directly, as there is no atmospheric absorption above these levels. This type of situation, along with supporting meteorological data on the cloud-top temperature,

affords a good opportunity for obtaining an effective graybody emissivity of the cloud in the HRIR spectral region.

The surface minus equivalent blackbody temperature difference depends not only on atmospheric absorption but also on the emissivity of the radiating surface. The effect of surface emissivity on the theoretical temperature difference is shown in Figure 7 for the High Latitude Winter and Tropical Model. The solid line curves represent a graybody surface emissivity of unity and are identical to the corresponding curves of Figure 5. The dashed line curves represent a graybody surface emissivity of 0.9. The results, again, apply only for clear sky conditions. In general, decreasing the surface emissivity to 0.9 increases the temperature differences by about 2.0°K for low zenith angles and less then 2.0°K for very high zenith angles. The temperature difference for the High Latitude Winter Model increases from 0.3°K to 2.0°K and the Tropical Model from 2.3°K to 5.0°K at low zenith angles. At very high zenith angles, the effect of surface emissivity on the temperature difference decreases as the surface contribution to the outgoing radiation becomes smaller. The results of Figure 7 indicate that if the emissivity of the surface is less then unity, which is true to some degree, then assuming the emissivity is unity causes the true surface temperature to be underestimated. Thus the surface emissivity must be known in order to obtain the true surface temperature from the surface radiating temperature.

Satellite radiation measurements have been obtained previously in the atmospheric window at 8 to 12 microns from the TIROS meteorological satellite. A comparison of the TIROS VII 8 to 12-micron window with the Nimbus window is presented in Figure 8. The upper curve represents the Nimbus HRIR window and the lower curve the TIROS VII 8 to 12-micron window. These results are for the ARDC Standard Model (1959) and for a surface emissivity of unity. The temperature differences are about 1.5 and 4.8°K for the Nimbus window and about 9.2 and 14.9°K for the TIROS VII window for zenith angles of 0° and 75° respectively. Thus, the Nimbus HRIR window shows considerable improvement over the 8 to 12 micron window used in the

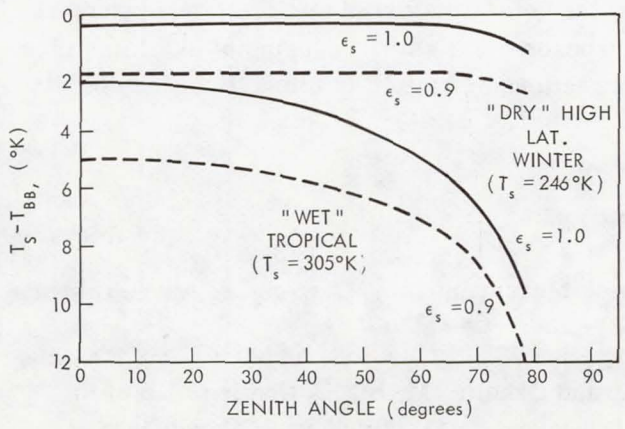

Figure 7—Surface emissivity effect on the theoretical temperature differences as a function of zenith angle. Clear sky conditions and a graybody surface emissivity are assumed.

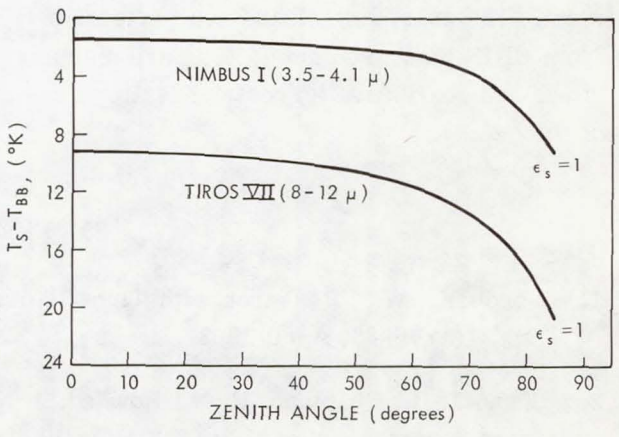

Figure 8—A comparison of the theoretical temperature difference as a function of zenith angle for the Nimbus I HRIR 4 micron "window" and the TIROS VII 8- to 12-micron "window." The results are for clear sky conditions, the ARDC Std. (1959) Atmosphere and a graybody surface emissivity of unity.

TIROS series. Actual results from the Nimbus I HRIR measurements indicate that there is excellent agreement between the known surface temperatures and the radiometrically measured temperatures if the above mentioned theoretical calculations are applied and if completely clear sky conditions can be ascertained.

CONCLUSIONS

The outgoing radiation which should be observed by the Nimbus I HRIR was calculated for several model atmospheres. The results, considering only atmospheric absorption, indicate the equivalent blackbody temperature measured by the HRIR should be within 2°K of the surface radiating temperature for clear sky conditions and low zenith angles which agrees with the actual HRIR observations. Surface radiation contributes about 95% and the atmosphere about 5% of the observed outgoing radiation for the ARDC Standard Model Atmosphere (1959) for clear sky conditions and low zenith angles. Decreasing the surface emissivity from 1.0 to 0.9 increases the difference between the true surface temperature and the equivalent blackbody temperature which the HRIR should measure, by about 2°K.

The Nimbus HRIR 4 micron window represents considerable improvement over the TIROS 8 to 12-micron window in measuring the surface radiating temperature as the correction for atmospheric absorption is much smaller. Because the correction is so small, in practice, a standard correction can be made ranging from about 0.3°K for high latitude regions to about 2°K for equatorial regions. In principle, of course, the TIROS 8 to 12-micron results can also be corrected for atmospheric absorption. However, the correction is fairly large and relatively more sensitive to changes in the atmospheric model so that a standard correction would not be a satisfactory solution. While the Nimbus HRIR 4-micron window does represent an improvement in obtaining the surface radiating temperature, it elevates in importance the problems of surface emissivity and sources of attenuation other than molecular absorption, which must be solved in order to obtain true surface temperatures from a satellite measurement. The preceding discussion pertains only to the determination of surface temperatures from HRIR measurements. For pure mapping purposes, such as the mapping of nighttime cloud cover and qualitative terrestrial features the corrections discussed in this article may be neglected.

REFERENCES

1. Nordberg, W., "Research with Tiros Radiation Measurements," *Astronaut. and Aerospace Eng.* 1(3):76-83, April 1963.

2. Shaw, J. H., Chapman, R. N., Howard, J. N., and Okholm, M. L., "A Grating Map of the Solar Spectrum from 3.0 to 5.2 Microns," *Astrophys. J.* 113(2):268-298, March 1951.

3. Goody, R. M., "Atmospheric Radiation," Oxford: Clarendon Press, 1964.

4. Wyatt, P. J., Stull, V. R., and Plass, G. N., "The Infrared Transmittance of Water Vapor," Newport Beach, California: Aeronutronic Div. Ford Motor Co., Report SSD-TDR-62-127, Vol.2, September 1962. Also, *Appl. Optics* 3(2):229-241, February 1964.

5. Stull, V. R., Wyatt, P. J., and Plass, G. N., "The Infrared Transmittance of Carbon Dioxide," Newport Beach, California: Aeronutronic Div. Ford Motor Co., Report SSD-TDR-62-127, Vol. 3, January 1963. Also *Appl. Optics* 3(2):243-254, February 1964.

6. Wyatt, P. J., Stull, V. R., and Plass, G. N., "Quasi-Random Model of Band Absorption," *J. Opt. Soc. Amer.* 52(11):1209-1217, November 1962.

7. Plass, G. N., "Spectral Emissivity of Carbon Dioxide from 1800-2500 cm^{-1}," *J. Opt. Soc. Amer.* 49(8):821-828, August 1959.

8. Winters, B. H., Silverman, S., and Benedict, W. S., "Line Shape in the Wing Beyond the Band Head of the 4.3μ Band of CO_2," *J. Quant. Spectrosc. Radiat. Transfer* 4(4):527-537, July-August 1964.

9. Young, Charles, "A Study of the Influence of Carbon Dioxide on Radiative Transfer in the Stratosphere and Mesosphere," Ann Arbor, Michigan: University of Michigan, 1964 (Dissertation).

10. Drayson, S. R., "Atmospheric Slant Path Transmission in the 15μ CO_2 Band," Ann Arbor, Michigan: University of Michigan, Technical Report 05863-6-T, N65-20944, November 1964. Also, published as a NASA Technical Note D-2744, April 1965.

11. Elsasser, W. M., and Culbertson, M. F., "Atmospheric Radiation Tables," *Meteorol. Monographs*, 4(23):1-43, August 1960.

12. Moller, F., and Raschke, E., "Evaluation of TIROS III Radiation Data," Munchen, Germany: Ludwig-Maximilians-Universität, Meteorologisches Institut, Interim Report No. 1, July 1963.

13. Cole, A. E., Kantor, A. J., and Court, A., "Supplemental Atmospheres," in: *Interim Notes on Atmospheric Properties-32 (Rev.)*, Bedford, Massachusetts: Air Force Cambridge Research Laboratories, Office of Aerospace Research, June 1963.

14. Manabe, S. and Moller, F., "On the Radioactive Equilibrium and Heat Balance of the Atmosphere," *Monthly Weather Rev.* 89(12):503-532, December 1961.

15. Hanel, R. A., Bandeen, W. R., and Conrath, B. J., "Infrared Horizon of the Planet Earth," *J. Atmos. Sci.* 20(2):73-86, March 1963.

16. Zdunkowski, W., Henderson, D., and Hales, J. V., "The Influence of Haze on Infrared Radiation Measurements Detected by Space Vehicles," Salt Lake City, Utah: Intermountain Weather, Inc., AD 605 688, July 1964.

17. Deirmendjian, D., "Atmospheric Extinction of Infrared Radiation," *Quart. J. Roy. Meteor. Soc.* 86(369):371-381, July 1960.

18. Curcio, J. A., Knestrick, G. L., and Cosden, T. H., "Atmospheric Scattering in the Visible and Infrared," Washington, D. C.: U. S. Naval Research Laboratory, NRL Report 5567, January 1961.

19. Diermendjian, D., "Scattering and Polarization Properties of Polydispersed Suspensions with Partial Absorption," Santa Monica, Califronia: The Rand Corporation, RM-3228-PR, July 1962.

20. Penndorf. R. B., "Scattering and Extinction Coefficients for Small Absorbing and Non-absorbing Aerosols," *J. Opt. Soc. Amer.* 52(8):896-904, August 1962.

21. Wark, D. Q., Yamamoto, G., and Lienesch, J. H., "Methods of Estimating Infrared Flux and Surface Temperature from Meteorological Satellites," *J. Atmos. Sci.* 19(5):369-384, September 1962.

22. McDonald, R. K., and Bell, J., et. al., "Infrared Satellite Backgrounds. Part I. Atmospheric Radiative Processes," Seattle, Washington: Boeing Company, Report D2-90054; AFCRL 1069; AD 273 099, September 30, 1961.

TERRESTRIAL FEATURES OBSERVED BY THE HIGH RESOLUTION INFRARED RADIOMETER

William Nordberg and R. E. Samuelson

INTRODUCTION

It is possible to obtain an excellent nighttime representation of terrestrial cloud and terrain features by means of satellite infrared radiometry. In addition, a quantitative assessment of the effective blackbody temperature corresponding to each feature can be obtained. The Nimbus HRIR has proven to be well suited for these purposes.

MAPPING BLACKBODY TEMPERATURES WITH HIGH RESOLUTION RADIOMETRY

The principle of mapping cloud or terrain features by means of infrared radiation is quite simple: All objects emit electromagnetic radiation, the spectral distribution and intensity of which are unique functions of the object's temperature, T, and its surface configuration. For blackbodies the intensity over a given spectral range is a function of temperature, T, only. This fact is expressed mathematically by Planck's law:

$$I_{BB} = \int_{\lambda_1}^{\lambda_2} \left(C_1/\lambda^5\right) \left(\exp C_2/\lambda T - 1\right)^{-1} d\lambda = \int_{\lambda_1}^{\lambda_2} B(\lambda, T)\, d\lambda \ , \qquad (1)$$

where C_1 and C_2 are constants and I_{BB} is the intensity of the radiation (watts/m^2-ster) by the blackbody surface within the wavelength interval $\lambda_2 - \lambda_1$. The Nimbus HRIR was built to make accurate measurements of I_{BB} from which equivalent surface blackbody temperatures, T_{BB}, could be inferred. To this end λ_1 and λ_2 were selected to correspond to wavelengths of 3.4 and 4.2 microns respectively. The atmosphere is quite transparent in this spectral range. Thus, in the absence of clouds, radiation emitted by the earth's land or water surfaces reaches the satellite with only minor interference by the clear atmosphere. (See V. Kunde in this publication.) When we derive equivalent blackbody surface temperatures, T_{BB}, from the measured intensities, we assume that the radiation is emitted isotropically and that the instantaneous field of view of the radiometer is filled by a surface of uniform temperature. The assumption of isotropy is not rigidly valid but must be used for lack of better knowledge of the directional variation of the measured intensities. The assumption of uniformity restricts the interpretation of the Nimbus I surface temperature measurements to objects which are homogeneous over a distance greater than about 6 kilometers. This is quite adequate for cloud formations associated with large-scale meteorological phenomena (for example, fronts, storms, and fog layers) and for many terrestrial features (for example, deserts, ice caps, and lakes).

BLACKBODY TEMPERATURES AND SURFACE TEMPERATURES

Equation 1 applies only to blackbodies. Water surfaces are sufficiently black in this spectral region that temperatures, T_{BB}, derived from the measured intensities are generally within 2°K of the actual surface temperatures, T. An error of 2°K is commensurate with the error inherent in the measured intensity.

Some other surfaces, however, cannot be assumed as black. Laboratory measurements show that at wavelengths of about 4 microns, certain minerals and soils may absorb only a fraction, ϵ, of the radiation incident upon their surfaces. Kirchoff's law states that in this case the blackbody emission given by Equation 1 must be multiplied by the same fraction ϵ to obtain the radiance (intensity) I_G from a nonblack ("grey") body:

$$I_G = \int_{\lambda_1}^{\lambda_2} \epsilon(\lambda)\, B(\lambda, T)\, d\lambda \quad . \tag{2}$$

The fraction, ϵ, is the emissivity of the surface. Defining an average emissivity ($\bar{\epsilon}$) within the wavelength 3.4 to 4.2 microns we may rewrite Equation 2 as

$$I_G = \bar{\epsilon} \int_{\lambda_1}^{\lambda_2} B(\lambda, T)\, d\lambda = \bar{\epsilon}\, I_{BB} \quad . \tag{3}$$

Using the appropriate values for C_1 and C_2 and for λ_1 and λ_2 in Equation 1 we find that at a blackbody temperature of 290°K, which is typical for the earth's surface seen by Nimbus at low latitudes, the value of I_{BB} is about 1.4×10^{-1} watts/m^2-ster. A reduction of this value by 10 percent corresponds to a T_{BB} value of 288.2°K. This means that a surface of 290°K with an average emissivity of 0.9 emits radiation of the same intensity as a blackbody surface of about 288.2°K. Since the minimum temperature change discernible with the HRIR is about 1° to 2°K, the knowledge of $\bar{\epsilon}$ in the derivation of T from I_G is important only if the emissivity is considerably smaller than 0.9.

Surface emissivities can actually be derived from HRIR daytime observations of reflected solar radiation. In this case the measured radiation intensities are not only due to surface temperatures but also due to the ability of the surfaces to reflect sunlight. The radiation intensity, I_D, sensed by the radiometer during daytime is the sum of the emitted grey body radiation, I_G, and the reflected solar radiation, rI_s. The reflectivity, r, of practically all terrestrial surfaces is given as $1 - \epsilon$. Thus, if we define $\bar{r}$ as the average reflectivity in the 3.4 to 4.2-micron range we may write

$$I_D = I_G + \bar{r} I_s = \bar{\epsilon} I_{BB} + (1 - \bar{\epsilon})\, I_s \quad , \tag{4}$$

where I_s is computed from the solar constant on the basis of purely geometrical considerations. A measurement of $I_D = I_s = 1.33$ watts/m^2-ster would result if the surface were a

perfect, 100 per cent effective, diffuse reflector for solar radiation at vertical incidence. For a reflectivity $\bar{r} = 0.6$, an emissivity $\bar{\epsilon} = 0.4$ and a surface temperature $T = 290°K$, $I_{BB} = 0.14$ watts/m^2-ster and $\bar{r}I_s = 0.80$ watts/m^2-ster. Hence, if the surface emissivity is smaller than 0.4, I_{BB} may be neglected and Equation 3 reduces to

$$I_D = I_s - \bar{\epsilon} I_s \quad . \tag{5}$$

Thus only if the surface emissivity is smaller than 0.4 or if the surface temperature is less than 290°K may the emissivity be derived without any knowledge of the surface temperature. For $\bar{\epsilon} > 0.4$ the emissivity can still be measured very accurately provided that the surface temperature is known. For example if $\bar{\epsilon} = 0.99$ and $T = 290°K$, $I_D = 0.15$ watts/meter^2; if $\bar{\epsilon} = 1.00$ (blackbody), $I_D = 0.14$ watts/meter^2. The difference of 0.01 watts/meter^2 is due to the term $\bar{r}I_s$ in Equation 3 and is equivalent to a blackbody temperature change of about 2°K which is just at the sensitivity threshold of the HRIR. In sunlight, emissivities of 0.99 can therefore easily be discerned from blackbodies and the HRIR which was in operation during daytime for several orbits of Nimbus I provides a very accurate method to measure large-scale surface emissivities at 4 microns.

Preliminary evaluations of these daytime observations indicate the emissivities for large-scale surfaces (oceans and moist vegetated regions) are greater than 0.9. Thus, HRIR measurements permit the world wide mapping of actual temperatures of these surfaces during nighttime and the mapping of emissivities of non-blackbody surfaces during daytime. Global measurements of earth surface temperatures (as opposed to air temperatures measured near the ground) are of considerable value in meteorological research since these temperatures can be used as initial values in the numerical analysis and prediction of weather. At polar latitudes HRIR surface-temperature maps relate to the morphology of ice formations. Such maps are both of practical application to navigation and of fundamental interest to glaciologists. Over oceans surface temperature differences may indicate the location of currents, fronts, etc. This suggests the potential use of Nimbus HRIR observations in oceanographic research. Soil moisture content can be derived at least qualitatively from the Nimbus HRIR observations since appreciably higher soil temperatures are measured in moist areas. Aircraft observations of emitted infrared radiation over regions of volcanic activity in Hawaii (Reference 1) has shown that underground lava beds can be detected with this technique; therefore, the Nimbus HRIR data were also investigated for this purpose. No definite identification of active volcanic areas could be made, however, because the spatial resolution of the HRIR is apparently too coarse. Global mapping of emissivity with such coarse resolution is, nevertheless, of geological interest. Maps of emissivity obtained by the satellite might establish a relationship between: (1) the small-scale emission properties of various minerals and soil constituents measured on samples in the laboratory and, (2) the large-scale properties of the same constituents in their natural state where they are blended with impurities, vary in grain sizes and morphology, and so on. The satellite observations can be considered very useful in determining whether the distribution of mineral and similar deposits can be mapped by measurement of emitted radiation with low spectral and spatial resolution. Any findings in this area may have considerable impact on the expectations for similar measurements of lunar and planetary surfaces.

SEA SURFACE TEMPERATURES

Since the blackbody assumption for water surfaces is quite valid in the 3.4 to 4.2-micron wavelength range, T_{BB} values derived from the radiation intensities relate directly to water surface temperatures. In cloudless regions the HRIR, therefore, can be used to map globally the surface temperatures of various bodies of water. Figure 1 shows an HRIR picture of the southwestern United States at midnight on 30 August 1964. The darkest region in the right center corresponds to a temperature of 301°K for the water surface in the northern Gulf of California. Applying Kunde's corrections for atmospheric absorption we obtain a temperature of 303°K for the waters of the Gulf of California, which is considerably warmer than the Pacific Ocean off the shore of California. There temperatures range from 293°K near the coast to about 280°K at a distance of about 200 km off shore. The low off shore temperatures indicate the presence of fog or dense haze, while the temperature of 293°K measured just west of Los Angeles is in good agreement with the temperature of 292°K measured from shipboard by the U. S. Coast Guard. Even small water features such as lakes can be clearly identified and their surface temperatures can be determined. The four black (warm) dots in the upper left corner of Figure 1 are mountain lakes in the Sierra Nevada. The southwestern most lake is Lake Tahoe; its water surface temperature was measured by the HRIR as 283°K. But, for a small body of water such as this, there is a question whether the field of view of the radiometer was fully covered by the lake. The actual water temperature therefore may be several degrees higher.

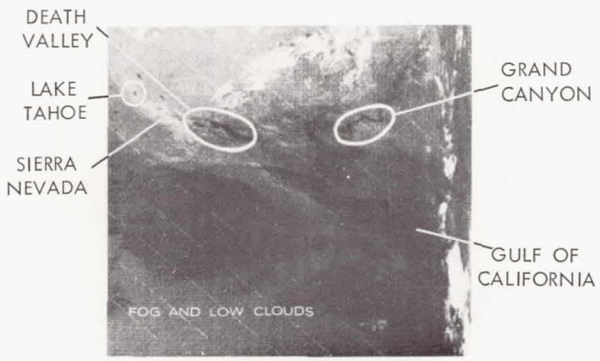

Figure 1—HRIR ocean and terrain temperatures over the southwestern United States near midnight on 30 August 1964. (Dark shades are warm, white shades are cold.)

The ability of the HRIR to map sea surface temperatures suggests that the course of various ocean currents, such as the Gulf Stream, for example, could be detected by the satellite. Unfortunately, during the life time of Nimbus I, clouds obscured most areas of interest. There is, however, the possibility that certain cloud formations themselves may be related to ocean temperatures. A suggestion of this can be found in a number of cases for which Figures 2a and 2b are typical. Very long and narrow clear streaks of open water lie between extensive low altitude stratus cloud decks over the North Pacific in Figure 2a and over the eastern Indian Ocean in Figure 2b. Here the streaks are at least 2000 km long and about 200 km wide. Although the phenomenon is apparently atmospheric it is conceivable that the cloud formations and the peculiar clearings may be influenced by ocean surface temperature differences.

Another example of satellite-observed variations in sea temperatures can be found in Figure 3 where sea surface temperatures over the Mediterranean are found to range from 297°K off the coast of Africa to 290°K near Corsica. Temperatures of the Adriatic and Tyrrhenian Seas are 294°K.

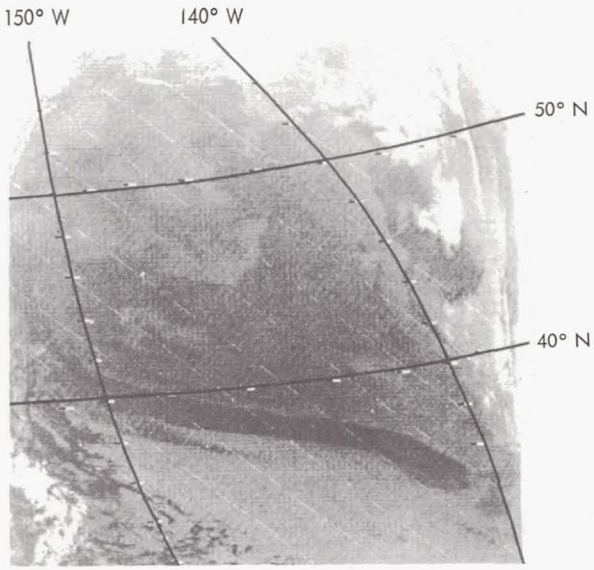

Figure 2a—HRIR cloud and water temperatures over the North Pacific near midnight on 30 August 1964. Clear streak of open water can be seen in the center. (Dark shades are warm, white shades are cold.)

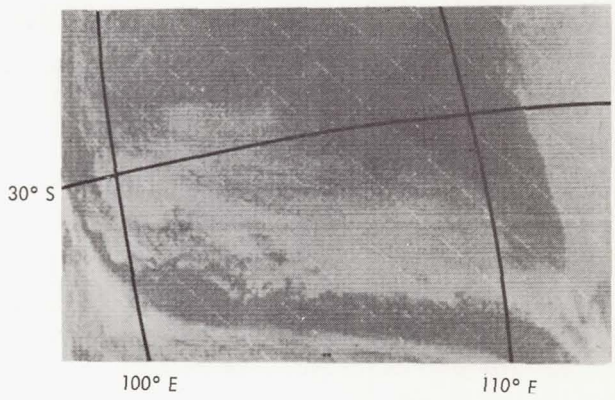

Figure 2b—HRIR cloud and water temperatures over the Indian Ocean near midnight on 9 September 1964. Clear streak of open water can be seen in the center. (Dark shades are warm, white shades are cold.)

TERRAIN FEATURES AND SOIL MOISTURE

Land surfaces are considerably more complex than sea or cloud surfaces. Therefore, under certain conditions, the temperatures derived from radiation intensities measured over land surfaces depend to a large extent not only on terrain heights but also on such parameters as heat capacity, conductivity and moisture content. First, a distinction must be made whether the variations in radiation intensity are due to actual ground temperature, or due to variations in emissivity. In the radiation observations with Nimbus I, most variations may be ascribed to actual surface temperatures. No cases have been found where variations in surface emissivities could be clearly identified in the HRIR measurements. Indeed, we believe from this experience with Nimbus that effective detection of surface features by means of emissivity measurements from spacecrafts will only be possible if the spatial and spectral resolutions of radiometric sensors are improved by several orders of magnitude over the capability of the Nimbus I instruments. On the other hand, a number of the topographic and geological features mentioned above may be inferred from the measurements of relatively broadband thermal emission performed with the Nimbus I HRIR. For example, the dark streaks in the upper portion of Figure 1 showing the Southwestern United States correspond to blackbody temperatures of about 290°K, while the lighter grey in the

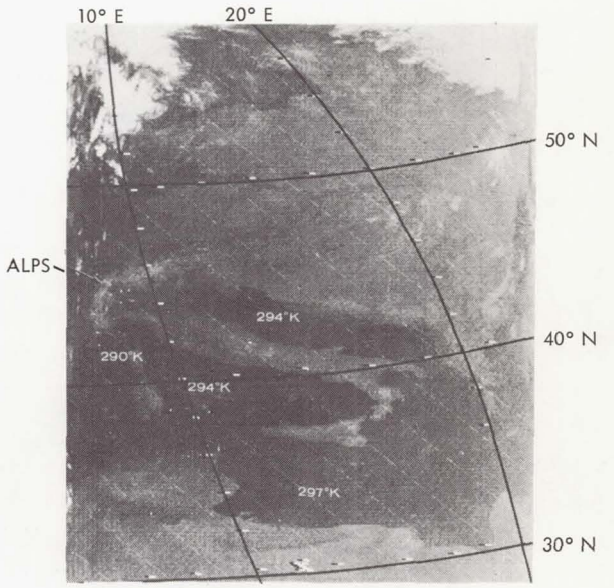

Figure 3—Temperatures over Europe observed by HRIR near midnight on 14 September 1964. (Dark shades are warm, white shades are cold.)

surrounding regions corresponds to about 275°K. The warm streaks were identified as Death Valley (left) and the Grand Canyon (right). Thus the temperature differences seen by the satellite correspond to actual differences in terrain height. Furthermore, a more quantitative interpretation of the temperatures over Death Valley reveals that the temperature difference of about 15°K measured by the satellite corresponds to an altitude difference of about 1800 meters between the valley floor and the surrounding highlands. The measured temperature decrease with altitude is therefore about 8.3°K/kilometer, which is in very good agreement with the expected temperature decrease in the free atmosphere (atmospheric lapse rate). This equilibrium between the soil and atmospheric temperatures leads to the conclusion that the heat capacity of the ground in this area must be generally very large, since only such a large heat capacity will prevent the surface at night from cooling more rapidly by radiation than the overlying atmosphere.

An example where other considerations are involved, in addition to topographic height changes, may be seen in Figure 4. Figure 4 shows a very large portion of western South America as seen by the HRIR on 14 September 1964 when much of the region was essentially free of clouds except for the Intertropical Convergence Zone north of 10°S, an extensive low altitude layer of stratus clouds along the entire west coast, a high-altitude cloud deck off southern Chile and some smaller clouds along the eastern horizon. The broad, white (cold) band through the center of the picture corresponds to the cold, high altitude mountain ranges of the Andes. Average blackbody temperatures of 255°K are measured over the highest elevations between 28° and 32°S. To the northeast there is a remarkably rapid transition from the cold highland with average blackbody temperatures of 270°K to the very warm Amazonas Basin with blackbody temperatures of 290°K. The warm waters of Lake Poopo (19°S) and Lake Titicaca (16°S) are clearly evident in the generally cold highlands. In the plateaus to the east of the mountains (30°-35°S) and in northern Chile (24°S) remarkable fine structure in the temperature patterns may be observed. The crescent shaped figure near 23°S corresponds to the Salar de Atacama, a salt flat in northern Chile. The discrete band of warm temperatures (273°K) surrounding the crescent stands out clearly while the center is quite cold (263°K). The topographic map (Figure 5) shows that the entire Salar covers a region of fairly uniform altitude of about 2300 meters. Thus

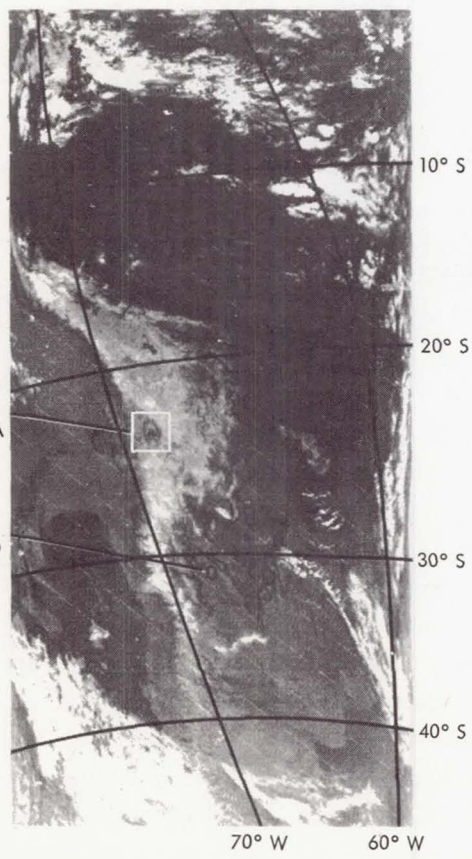

Figure 4—Temperature over South America observed by HRIR near midnight on 14 September 1964. (Dark shades are warm, white shades are cold.)

on the basis of terrain height there is no reason to assume the existence of a temperature difference between the center and the rim. Laboratory measurements by Hovis (Reference 2) have shown that, of many common minerals tested in this spectral region, pure rock salt has the lowest average emissivity. Hovis' measurements give a value of less than 0.5 for $\bar{\epsilon}$. Therefore, HRIR measurements of pure salt with an actual surface temperature of 273°K would give a value of T_{BB} of less than 263°K, while other rock formations at the same altitude and temperature along the periphery of the Salar would yield a T_{BB} measurement very near the actual temperature of 273°K. The difference of 10°K between the cold center and the warm band in Figure 4 could thus be explained. There is still a question, however, if the emissivities measured for pure salts in the laboratory are applicable to naturally impure salt deposits such as this Salar. A more probable interpretation is that the emissivity of the natural salt over the Salar is much greater than 0.5, but that the heat capacity of the salt is considerably less than that of the surrounding rock formulations at the same altitude level. This fact, combined with the very high reflectivity of sunlight and the very low heat conductivity of the relatively fine grained salt deposits, prevents the storage of large amounts of solar heat over the Salar itself, and, after sunset, causes it to cool very rapidly by radiation, resulting in a very low temperature (263°K) at midnight. The rocks along the periphery, however, remain warmer throughout the night (273°K) because of their larger heat capacity and greater conductivity.

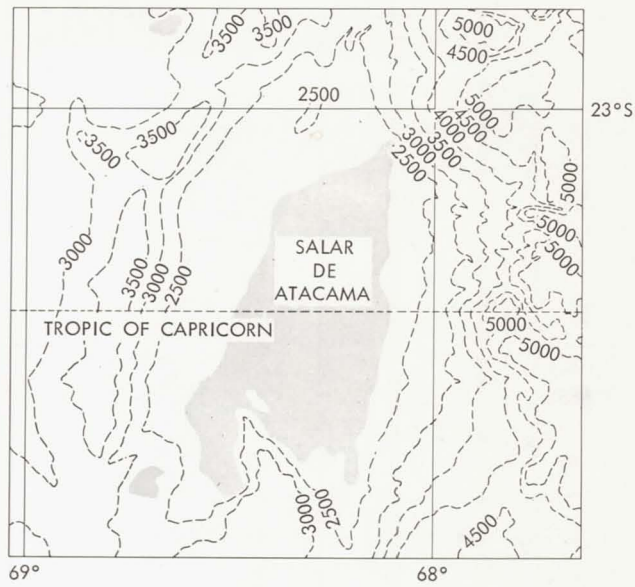

Figure 5—Topographic map of Salar de Atacama in north Chile.

A similar case may be observed in Figure 4 near 32°S and 68°W over western Argentina. Here, again, a nearly circular dark band of about 5 kilometers in width and about 40-50 kilometers in diameter indicates the existence of a high temperature zone along this peculiarly shaped band. The cold temperatures (white spot) in the center of the band can easily be explained by topography. The center of the band corresponds to the Pie de Palo mountain shown topographically in Figure 6. The lowest temperature measured in the center of the band is 268°K and corresponds to the highest elevation of about 3000 meters (Figure 6). The temperature along the band is about 280°K, which is about 7°K warmer than the temperature of 274°K of the surrounding desert. Since the band around the mountain is certainly not at a lower altitude than the surrounding desert plateau (Figure 6), the explanation of the warmer temperatures must again be found in the difference in heat storage between the desert sand and the rocks of the Pie de Palo mountains. A visual survey* revealed that the contrast

*This survey was made possible by the staff of the University of San Juan, Argentina. We are especially indebted to Professor C. V. Cesco who provided us with valuable background material for this investigation.

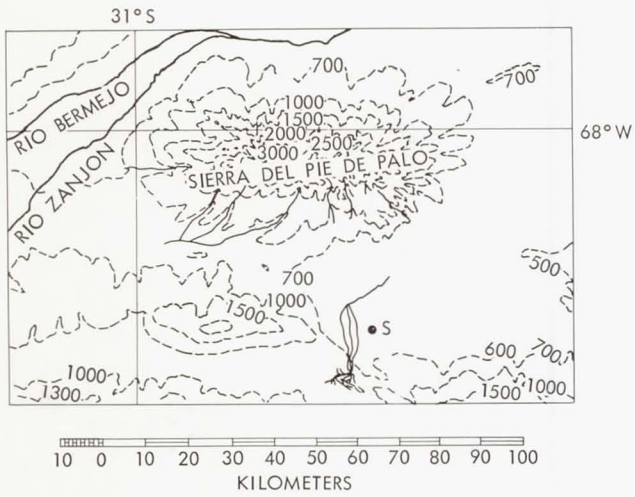

Figure 6—Topographic map of Pie de Palo mountains in western Argentina.

between the precambrian rock formations of the Pie de Palo mountains and the alluvial sand deposits of the surrounding desert is indeed very striking and extends around the mountains approximately along the 1000-meter contour line (Figure 6). The dark band seen by the satellite parallels approximately this 1000-meter contour line. Furthermore, the temperature difference of 12°K between the warm band at 1000 meters and the mountain top rising rapidly to 3000 meters yields an approximate lapse rate of 6°K/kilometer, which corresponds much better to the expected adiabatic lapse rate than the temperature difference of 6°K between the desert plateau at about 800 meters and the mountain top. That latter difference would yield a rather unrealistic lapse rate of 3°K/kilometer. Thus, the temperature over the desert is considerably lower because of the small heat capacity and conductivity of the ground, causing a temperature inversion in the air over the desert, while the solid rocks again remain considerably warmer, resulting in the adiabatically decreasing temperature from the periphery to the center of the mountain.

HRIR pictures over the deserts of North Africa and the Near East exhibit similar fine structure in the emitted radiation with inferred temperature variations of 10° to 15°K. Again, we conclude that these gradients are due to variations in the thermal properties of the soil rather than due to emissivity variations.

In this fashion the satellite HRIR observations on a small scale permit the mapping of geological features which can be distinguished by their thermal properties. On a larger scale these patterns of heat capacity assume meteorological significance since storage of heat in the ground is an important consideration in the numerical description of atmospheric processes.

Moisture content of the soil is also evident in the HRIR observations. It has been very surprising that many rivers of widths of less than 1 kilometer stand out prominently in the radiation pictures, although the linear resolution of the HRIR is generally not better than 5 kilometers. The prominence of the rivers is apparently due to the fact that the heat capacity of the ground along these rivers is altered, probably by moisture in the ground, and that this moisture retains solar heat absorbed during daytime much longer than the adjacent drier regions. Several rivers are noticeable to the east of the Andes in Figure 4. Two rivers are particularly prominent; their confluence is located just to the east of the conspicuous warm band around the Pie de Palo mountains discussed above. These rivers can be identified as the Rio Zanjon and Rio Bermejo in northwestern Argentina. Interestingly, despite their prominence in the radiation pictures, these rivers are only less than a few hundred meters wide and, except for occasional spring flooding, they carry practically no water. Also, the rivers do not form any deep canyons or other depressions in this area, so that their warmer temperatures

cannot be explained by height differences. In the course of time, however, their courses have meandered over widths of several kilometers over the desert plateau. These meanderings have apparently taken place during the flood stages, and have altered the terrain to such an extent as to create a sufficient contrast in the thermal properties between the desert and the river beds that the nighttime temperature differences could be detected by the satellite radiometer. Of course, such contrasts can only be created where the surrounding terrain is very dry and of very small heat capacity. For example, only vague indications can be found in Figure 4 of the Amazonas River which is much wider than the Bermejo and Zanjon rivers that stand out so clearly. In the Amazonas Basin the entire region possesses such a large heat capacity, due to its moisture and heavy vegetation, that a uniform and high temperature is maintained throughout the night. Because of this fact the boundaries between water and land which include the outlines of continents cannot be distinguished in the HRIR observations in tropical regions.

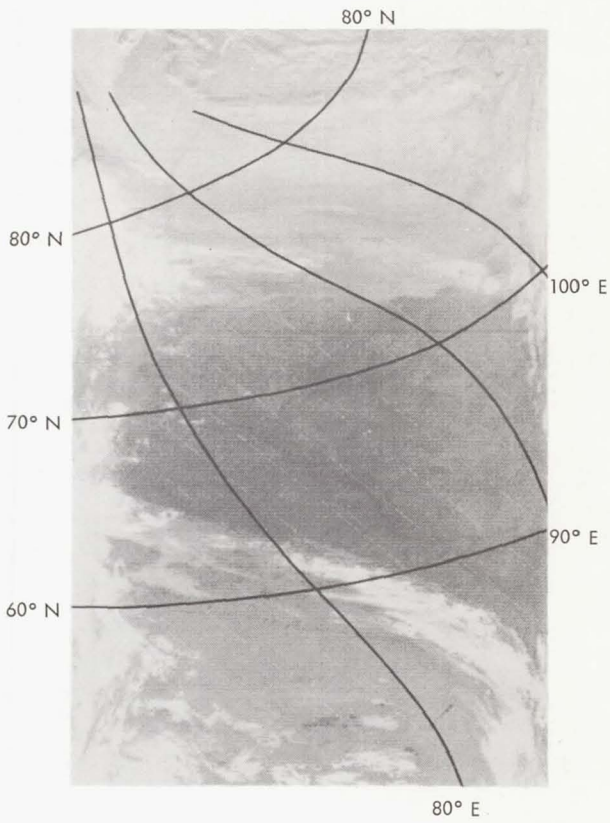

Figure 7—Temperature over Siberia observed by HRIR near midnight on 5 September 1964. (Dark shades are warm, white shades are cold.)

An example of very close equilibrium between soil and air temperatures can be found over the Siberian Tundra as shown in Figure 7. In this figure a band of clouds, manifesting a cold front, crosses western Siberia near 60°N. Cloudless skies prevail both to the north and south, which is indicated by the clearly visible lakes and rivers on both sides of the front. Blackbody temperatures, however, are markedly different on the two sides. To the south of the front temperatures range from 277°K to about 280°K, while to the northwest they are about 287°K. Analysis of surface air data provided by the Hydrometeorological Service of the U.S.S.R. show that surface air temperatures in the southern region were about 279°K, while in the northwest they ranged from 283° to 288°K. This equivalence with the satellite measured soil temperatures suggests a complete equilibrium between air and soil temperatures over this region. Other HRIR Nimbus observations have been obtained over this same area during September 1964, but the temperature contrast was apparent only for this case. This leads to the rather surprising conclusion that the soil temperatures in this case were governed by the temperatures of the overlying air masses.

Thus, a variety of different geophysical and atmospheric facts can be inferred from the observation of temperature variations over the earth's terrain. Over heavily vegetated regions of the tropics the ground temperature can be measured, and, because of the larger heat capacity

of this type of terrain, its effect on air temperatures is similar to that over oceans; the ground acts as a reservoir which heats or cools the air moving over it depending on its temperature. At higher altitudes, especially over dry sandy terrain, the heat capacity of the ground temperature is so small that near midnight, when solar radiation is absent, the satellite measured ground temperature is much less than the air temperature, demonstrating temperature inversions. Over more solid rock surfaces the satellite-measured ground temperatures are more nearly equal to the air temperatures. Contrasts in the thermal properties of the surfaces usually exhibit a very pronounced fine structure in the satellite observations. In many cases these contrasts can be interpreted, qualitatively at least, as a measure of moisture content of the ground, changes in the vegetation, or in the geological formation along the ground.

REFERENCES

1. Fischer, W. A., Moxham, R. M., Polcyn, F., and Landis, G. H., "Infrared Surveys of Hawaiian Volcanoes," *Science* 146(3645):733-742, November 1964.

2. Hovis, W., "Spectral Reflectivity of Common Minerals," (to be published in *Jour. Appl. Optics* 1965).

POLAR EXPLORATION WITH NIMBUS

R. Popham and R. E. Samuelson

INTRODUCTION

Nimbus I is the first weather satellite to provide daily photographic coverage of the polar regions. Representative samples of AVCS ice photography in the eastern Canadian Archipelago, western Greenland and coastal regions of the Antarctic are shown and significant features are noted. In the Canadian Archipelago the observed sea ice features are in excellent agreement with those reported by Canadian aerial ice observers. The advancing edge of the 1964-65 ice pack is easily identified in the AVCS pictures of the Thule, Greenland area; ice boundaries can be plotted to an accuracy of 3 to 7 miles.

Contrast is excellent for both AVCS and HRIR polar photography. Because of shadow effects, clouds are easily discriminated from ice and snow; the former are generally fuzzy in appearance while the latter have sharply defined boundaries. Altitudes of mountain peaks and clouds above the mean terrain level can be determined to within an accuracy of about 100 to 200 feet from shadows cast by the sun at large solar zenith angles.

Approximately 1500 miles of Weddell Sea area coastline in the Antarctic is shown. Large mosaics of ice cracks in the Antarctic pack ice provide large scale stress-strain patterns from which it should be possible to study the major dynamic forces operating in this ice. The apparent coastline of the Antarctic continent is well delineated by a thin, dark border. The width of this border grows or shrinks with time, depending upon the locale. Temperatures along this border are inferred to be around 270 to 272°K from HRIR data, strongly suggesting thin ice or open water. Pack ice temperatures average about 242 to 245°K, while the Antarctic continent proper shows surface temperatures which range from 240°K near the edge to 210°K near the pole.

The McMurdo Sound area of the Antarctic is extremely rich in detail. Very small features, such as the ice-free Taylor and Wright dry valleys and the mountains on Ross Island, stand out in the AVCS photographs with excellent clarity. The first iceberg ever observed from a satellite is shown—both in AVCS and HRIR—along the edge of the Filchner Ice Shelf.

In general, the quantity and quality of the Nimbus I AVCS and HRIR photography over the polar regions provides a wealth of useful information; studies in the fields of polar climatology and oceanography cannot help but benefit greatly from this material.

POLAR EXPLORATION WITH NIMBUS

One of the problems encountered by the satellite picture analyst is the interpretation of cloud patterns when viewed against a snow or ice background. One way to surmount this

difficulty is to produce "background charts" which, in effect, show characteristic features of the surface as it appears under varying conditions of snow or ice cover. In attempting to do this, a number of interesting and significant studies have evolved, and among these, the mapping of sea ice features has emerged as perhaps one of the most significant by-products of the meteorological satellite program.

In March 1961, a Military Sea Transport ship was routed into Stephanville, Newfoundland, largely on the basis of photographs of ice obtained from TIROS II. In February and April 1962, Canada and the U. S. conducted an extensive program to develop satellite ice reconnaissance techniques. In August 1963, some of these techniques were used at a Canadian APT receiving station in Frobisher Bay on Baffin Island to provide sea ice and weather information to ships operating between the northern Hudson Bay and the Labrador Sea. And in the spring of 1964, TIROS VII and VIII photographs were used to follow the breakup of ice in the Great Lakes.

With Nimbus, the problem of cloud-snow-ice identification was extended to include the Arctic and Antarctic regions. Again, the same technique of identifying surface features is being applied, this time both to the AVCS and HRIR photographs. Although the relatively short lifetime of the spacecraft precluded construction of operationally useful ice charts, the combination of high resolution AVCS photography, variable satellite altitude, low sun angle and nighttime HRIR photography resulted in the acquisition of a number of rather striking examples of meteorological, oceanographic, geological and geographic features in the polar regions.

The figures contained in this paper are representative of the type of photography acquired from Nimbus over areas previously unobservable from weather satellites. These figures illustrate the overall nature and quality of observations and have been selected for their general scientific interest.

By far the largest number of satellite ice reconnaissance studies conducted using data from the TIROS series of satellites were carried out over Canadian east coast waters. It would appear appropriate, therefore, to begin our discussion of Nimbus ice photography in the same general area. Figure 1 shows a map of this region; the three marked areas are areas for which we shall show examples of AVCS photography.

Area 1 contains the Foxe Basin region, just north of Hudson Straits. This is the southernmost area of ice viewed by Nimbus I in the Northern Hemisphere. Area 2 is the general vicinity of Thule, Greenland; this is one of the principal regions through which much of the thick polar ice and icebergs reach the North Atlantic. In area 3, the principal feature to be observed is continental ice—the Petermann Glacier in particular. We consider now these areas in succession.

Figure 2b shows the general Foxe Basin region. Note in particular Prince Charles Island just to the right of center and Air Force Island still further to the right. Figure 2a is an AVCS picture of the same area, virtually cloud-free. The southwestern part of Prince Charles Island is located at the center of the picture. The island itself is completely outlined by a thin belt of shore-fast ice. To the right is Air Force Island, completely surrounded by an extensive ice field. The extreme brightness of this area is due in part to fresh, light snow covering the entire frozen region. Just to the north and northwest of Prince Charles Island we have the

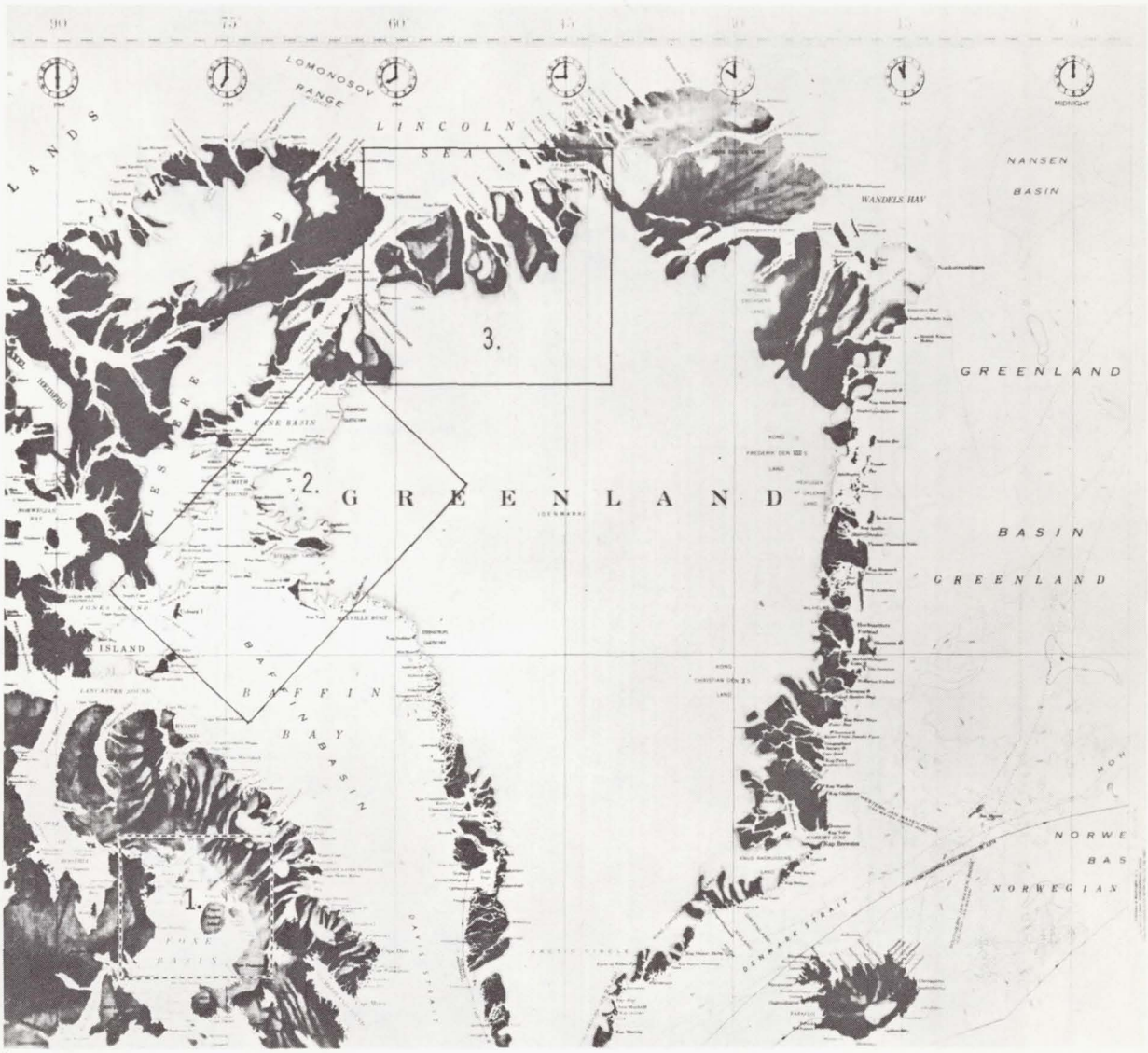

Figure 1—Map of the Greenland-eastern Canada area: Areas blocked off are, respectively, (1) Foxe Basin region, (2) Smith Bay region, and (3) Northwest Greenland region.

same effect. The extent of the ice as determined from this photograph is in very good agreement with sea ice observations reported by the Canadian Department of Transport for August 31 and September 2.

In the extreme upper right-hand corner the southwestern edge of the Barnes Icecap on Baffin Island can be seen. The original photograph shows a very thin grey edge around the cap, believed to be the actual ice of the cap. The snow appears to have been melted off by the sun much as the snow on the southern and western slopes of mountains would melt off first.

The U. S. Air Force Base at Thule, Greenland is located south of the two peninsulas shown in Figure 3b (Area 2). Figure 3a is an AVCS picture of the same area. The grey area on the left side of this figure is the leading edge of the ice pack which by December 1964 completely engulfed the entire water area shown in this photograph.

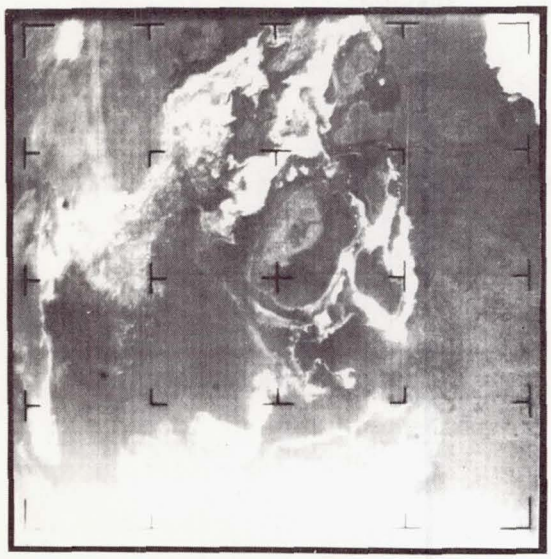

Figure 2a

Figure 2b

Figure 2—Foxe Basin region: (a) AVCS photograph (orbit 048, camera 1, 1425U.T., August 31, 1964), (b) map.

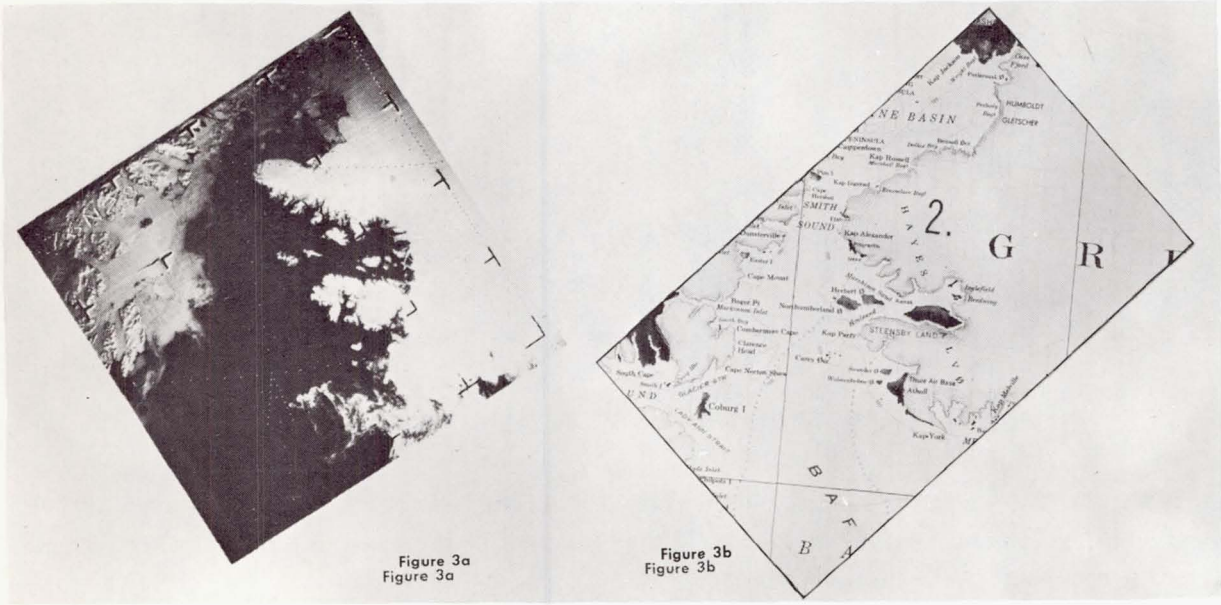

Figure 3—Smith Bay region: (a) AVCS photograph (orbit 253, camera 3, 1445U.T. September 14, 1964), (b) map.

For both long-range ice outlooks (three months or more) and 30-day ice forecasts the ice forecaster makes use of degree-days as well as any ice reports which can be obtained to predict the movement, extent and thickness of the ice. The number of degree-days for a given locale is normally obtained from historical meteorological records. Sea ice reports on the other hand, may be obtained two or three days apart, or a month or more apart, depending upon

weather conditions, flying distance to the ice pack, etc. According to most experts in ice observing and forecasting, photographs of the type and quality shown here, if obtained regularly, could provide much of the sea ice information used in preparing long-range forecasts and presently acquired through aerial ice reconnaissance. From these photographs the ice pack boundary can be plotted to an accuracy of within 3 to 7 miles, which is compatible with, and in some instances better than, the accuracy which can be achieved from aircraft over the open sea.

One of the most striking features of Nimbus photography is the pattern of sunlight and shadows resulting from a low sun elevation at polar latitudes. Examples of such shadows are illustrated in Figure 4. Figure 4a is an AVCS picture of the northwest Greenland area shown in Figure 4b (area 3). Shadows produced by relatively high ridges and mountains are readily seen in the upper portion of the photograph.

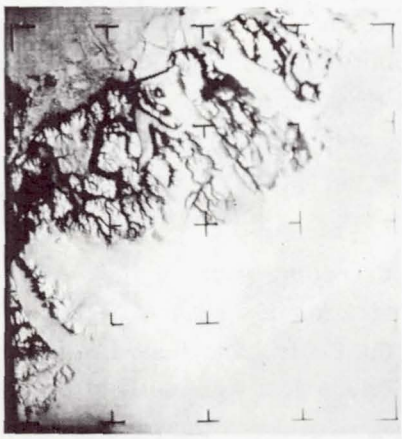

Figure 4a

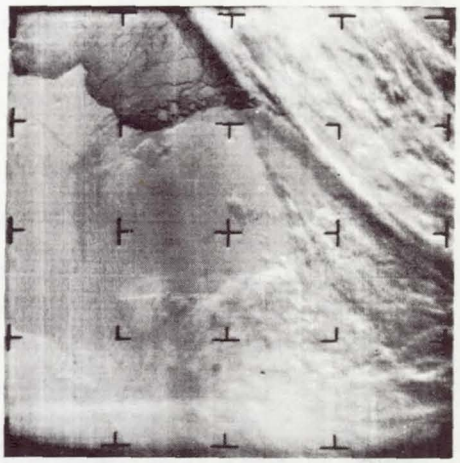

Figure 4c

Figure 4b

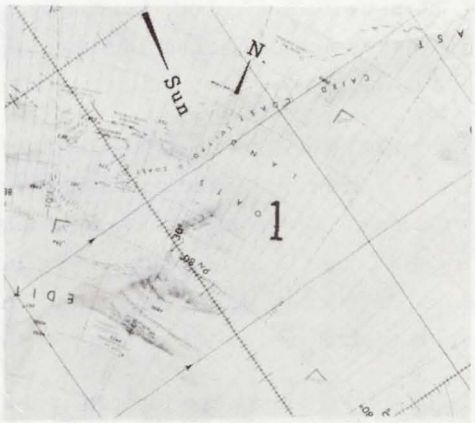

Figure 4d

Figure 4—Northwestern Greenland and Coats Land: (a) AVCS photograph of Northern Greenland showing Peterman glacier in lower left (orbit 089, camera 2, 0945U.T. September 3, 1964), (b) map showing same region as (a), (c) AVCS photograph of Coats Land region of Antarctic (orbit 239, camera 2, 1641U.T. September 13, 1964), (d) map showing same region as (c). The direction of direct sunlight is shown by arrows.

The Petermann Glacier can be seen in the lower left corner of Figure 4a. Note the sharp and detailed outline of the shadows cast by the chain of mountains east of the glacier. We were able to estimate the heights of two of the peaks in this chain in the following manner:

The length of the shadows cast on the top of the glacier were measured with a micro-linear scale. After determining the scale of the photograph and the sun's azimuth and elevation angle the heights of the peaks were determined as a direct consequence of the geometry. One peak was determined to be 3100 feet high, the other, 2600 feet—the lower peak being the more southerly of the two. Since the shadows were measured at the top of the glacier, it is obvious that these heights are not the true heights of the peaks. If the two peaks are of the same height, however, we could deduce from these measurements that the top of the glacier was 900 feet higher in the vicinity of the more southerly peak. It should be possible to determine the slopes of glaciers by this method if one knew the heights of surrounding mountains.

Unfortunately, at the time this experiment was performed, the true heights of these peaks were not known with sufficient accuracy to draw any definite conclusions. The only charts of this region available showed 3000-foot contours in the vicinity of these peaks. From a close examination of Nimbus photographs of the Nile Delta region we know that the resolution of the center camera of the AVCS is close to a quarter of a mile, and better in areas of high background contrast. For a resolution of one-quarter of a mile the estimated error in the measured heights of the two peaks is between 100 and 200 feet.

Another instance in which the method described in the preceding paragraphs might be applied is in the determination of cloud heights. A good illustration of a shadow produced by clouds is shown in Figure 4c. The figure corresponds to the Coats Land region of Antarctica, shown in Figures 4d and 5 (Area 1). In the top center of Figure 4c a well-defined cloud shadow extending across the ice pack just off the coast can be seen. Cracks in the pack ice are clearly visible. In a manner analogous to that in the preceding paragraphs the height of the top of the cloud casting the shadow is estimated to be approximately 6600 feet.

In contrast with the Arctic, relatively little is known about the Antarctic. Before proceeding with a discussion of Nimbus pictures obtained over the Antarctic, it would appear germane to discuss some of the known major facts about the Antarctic.

The continent of Antarctica has the highest mean height of any continent—approximately one mile. Cold air flowing off the continent sometimes reaches hurricane velocity by the time it reaches the coast. Average snowfall is only five inches per year. Although a temperature of as low as -88°C has been recorded in the interior, temperatures occasionally rise to a few degrees above freezing along the coast. This area is often referred to as the "Banana Belt" by individuals stationed in the interior of the continent.

If the Cascade Range were located in the Antarctic instead of North America, Mount Ranier would appear as a hill 400 feet high and Mount Shasta, about 150 feet high. Although not all of the Antarctic glaciers are 14,000 feet thick, many extend to sizeable depths. Unlike the Arctic, where glaciers tend to calve off at the water's edge, Antarctic glaciers may extend a few miles to several hundred miles into the ocean, forming huge ice tongues or high ice shelves sometimes 600 to 800 feet thick. The Ross Sea ice shelf is perhaps the best known example, but much of the apparent coastline of Antarctica is in fact a series of ice shelves.

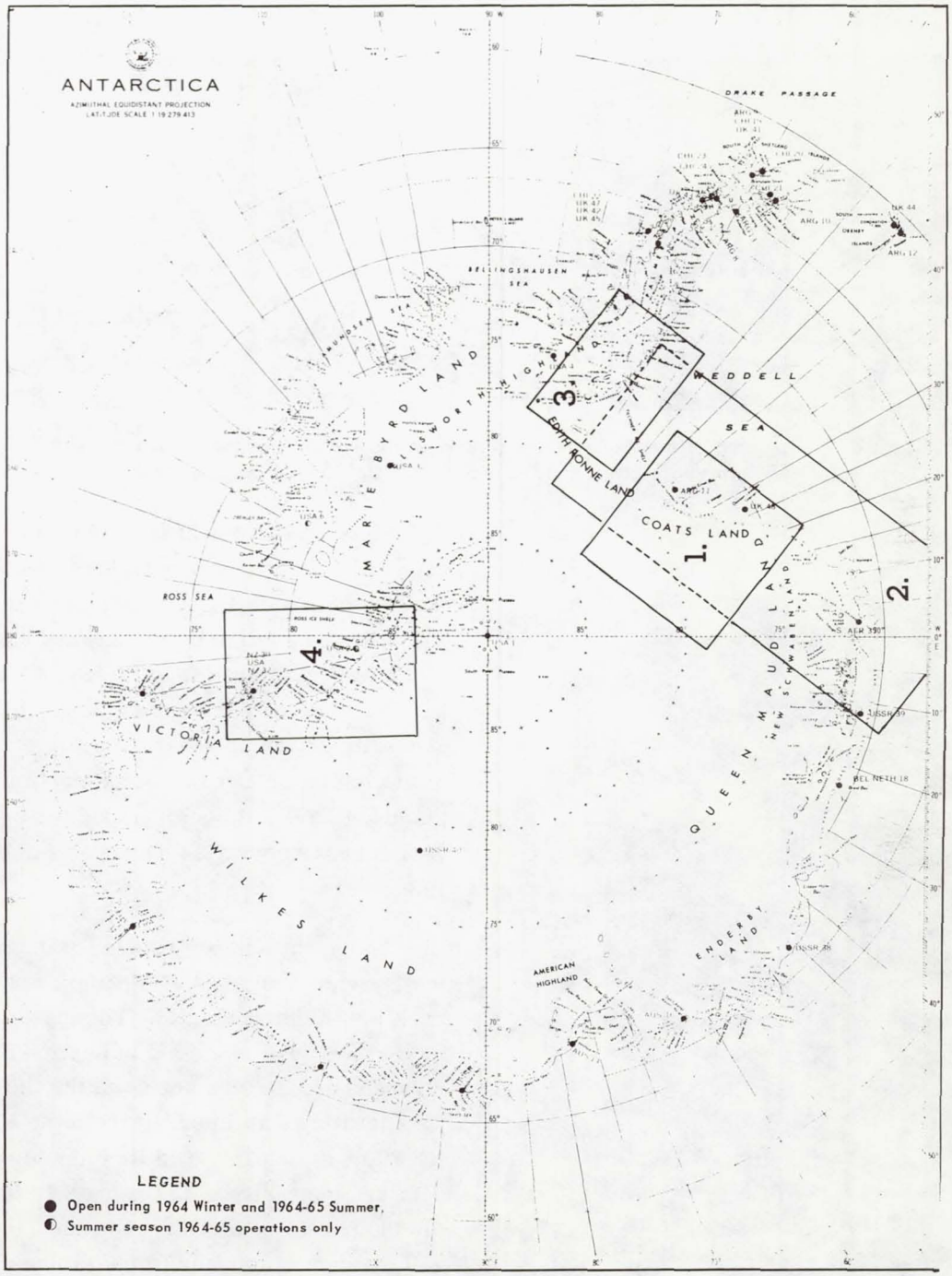

Figure 5—Map of Antarctica. Areas blocked off are, respectively, (1) Coats Land, (2) Weddell Sea coast, (3) Southeastern Antarctica Peninsula, and (4) McMurdo Sound area.

The continent of Antarctica is outlined in Figure 5. Area 1 in the figure has been shown in Figures 4c and 4d. Areas 2 through 4 are shown respectively in Figures 6 through 8.

Figure 6—Photographs of the Weddell Sea (cracks in the ice pack are readily apparent): (a) AVCS, orbit 195, cameras 1, 2, and 3, 1630U.T. September 10, 1964.

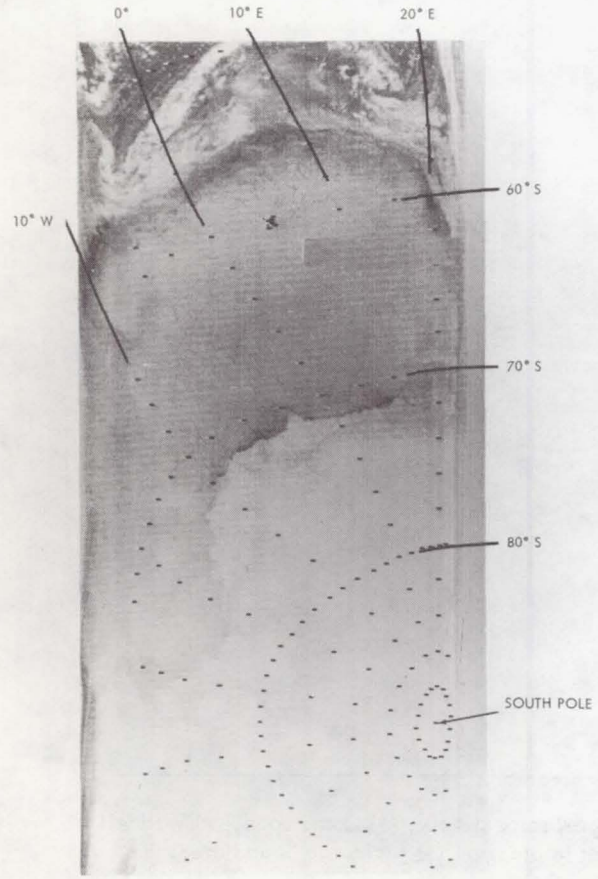

Figure 6—Photographs of the Weddell Sea (cracks in the ice pack are readily apparent): (b) HRIR, orbit 023, August 29, 1964.

Figure 6a (Area 2) is an AVCS photograph of the apparent coastline of the Weddell Sea, which is actually comprised of the Filchner ice shelf and the seaward extension of smaller glaciers along the coast. This is in effect a semi-permanent coastline and is generally shown as a fixed feature on charts of the Antarctic Ocean. Some portions of the coast have not been mapped for several years, one observation dating as far back as 1939.

The great number of cracks in the pack ice is evident on all AVCS photographs of pack ice in the Antarctic. The pattern shown by these cracks is a good indication of the stresses and strains set up in the ice itself. Temperatures as inferred from the Nimbus High Resolution Infrared Radiometer (HRIR) data are generally in the range 242 to 245°K for the pack ice in contrast to the 210 to 240°K range of surface temperatures for the Antarctic continent proper. Whether these differences in the effective radiometric temperatures are entirely real or whether they are due in part to the different emissivities of different types of surface materials is not known at present.

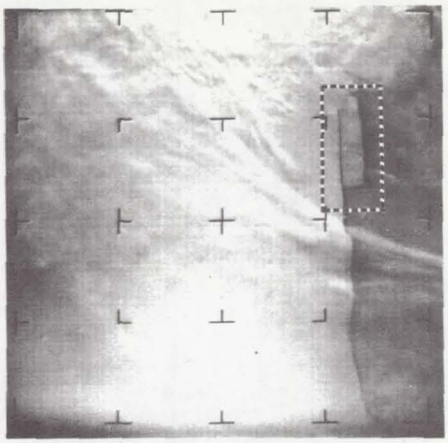

Figure 7a

Figure 7c

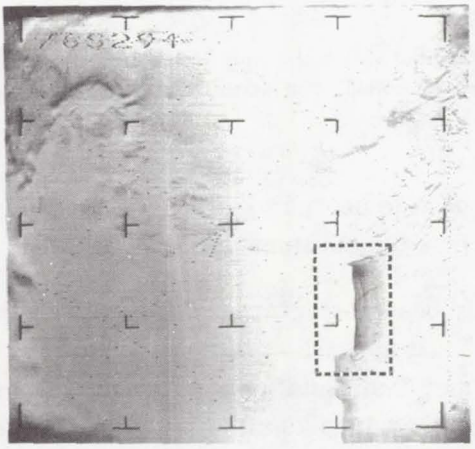

Figure 7b

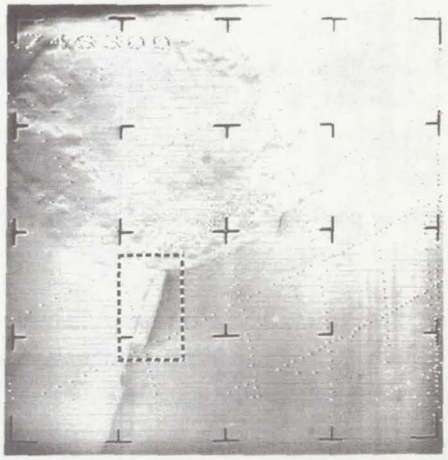

Figure 7d

Figure 7—AVCS and HRIR photographs of an iceberg in the Weddell Sea area (first known satellite photographs ever obtained of an iceberg): (a) AVCS, orbit 167, camera 2, 1834U.T. September 16, 1964, (b) AVCS, orbit 284, camera 2, 1831U.T. September 16, 1964, (c) HRIR, orbit 288, September 16, 1964, (d) AVCS, orbit 285, camera 3, 2008U.T. September 16, 1964. The contrast in the HRIR photograph (7c) is typical of HRIR photography over the Antarctic.

The apparent coastline of the Weddell Sea area as shown in Figure 6 is generally evident around the entire periphery of the continent, both in AVCS and HRIR. The temperatures inferred from the HRIR data indicate that the ice is either very thin along this border or that we are actually seeing open water. These temperatures range from 259 to 272°K, the lower temperatures prevailing in all cases where the apparent coastline is now wide enough to completely fill the field of view of the radiometer; in these cases, contributions from regions lying outside the immediate border contribute to the detected radiation, thereby reducing the inferred effective temperature. In those cases where the border is wide enough to completely fill the field of the HRIR radiometer, temperatures in the range 270 to 272°K are consistently inferred from the radiation data. The ice cracks, although observed as distinctly warmer than the

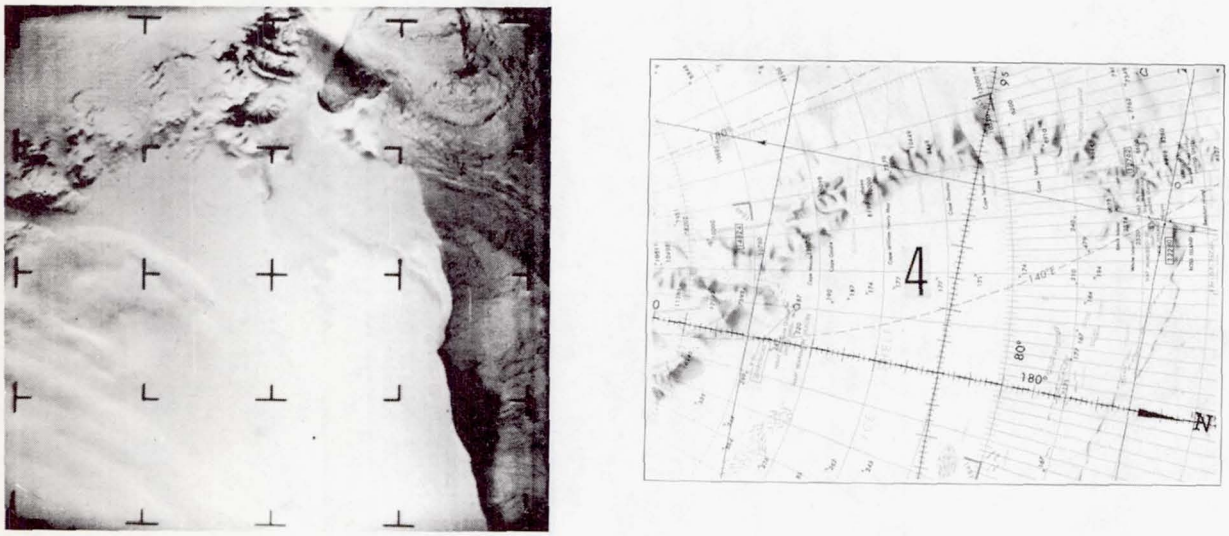

Figure 8—McMurdo Sound region (area 4 of Figure 5): (a) AVCS photograph showing Ross Island (upper right), Taylor and Wright dry valleys (dark, parallel features near upper center), and edge of the Ross Sea ice pack (along right side), (b) map showing same region as (a).

surrounding pack ice in the HRIR measurements, are not wide enough to allow reliable temperature determinations. The pack ice itself has a surface temperature of about 244°K.

The first known case in which an iceberg has actually been photographed from a satellite over either the Arctic or Antarctic is shown in Figure 7. It appears to have calved off the Filchner ice shelf near the southeastern end of the Palmer Peninsula (or the Antarctic Peninsula, as it is known). It is approximately 70 miles long and 15 to 20 miles wide. From its dimensions we can estimate that it is probably about 200 feet high.

The pictures in Figures 7b and 7d were taken about 1-1/2 hours apart and eight days later than the picture in Figure 7a. The dark region on the seaward side of the berg is not a shadow. We know this even without checking the sun angle, because the HRIR photograph in Figure 7c shows the same effect indicating that the dark region is comparatively warmer than its surroundings. The crack between the berg and the ice shelf proper also appears warmer than the surrounding region.

Figure 8a shows two very interesting geological features on South Victoria Land near McMurdo Sound. These are the rather famous Taylor and Wright dry valleys (dark, short parallel features near top center of photograph). These valleys are glacier carved and almost completely void of ice and snow; they do contain some small frozen fresh-water lakes. The dividing ranges are also almost completely ice-free, while the surrounding areas are fully glacierized. The edge of the glaciers for which the valleys are named are found at the head, or western end, of the valleys.

Figure 9a is an HRIR picture of the Ross Ice shelf in the Pacific sector of Antarctica. Although these observations were made three days after those shown in Figure 6b, the temperatures

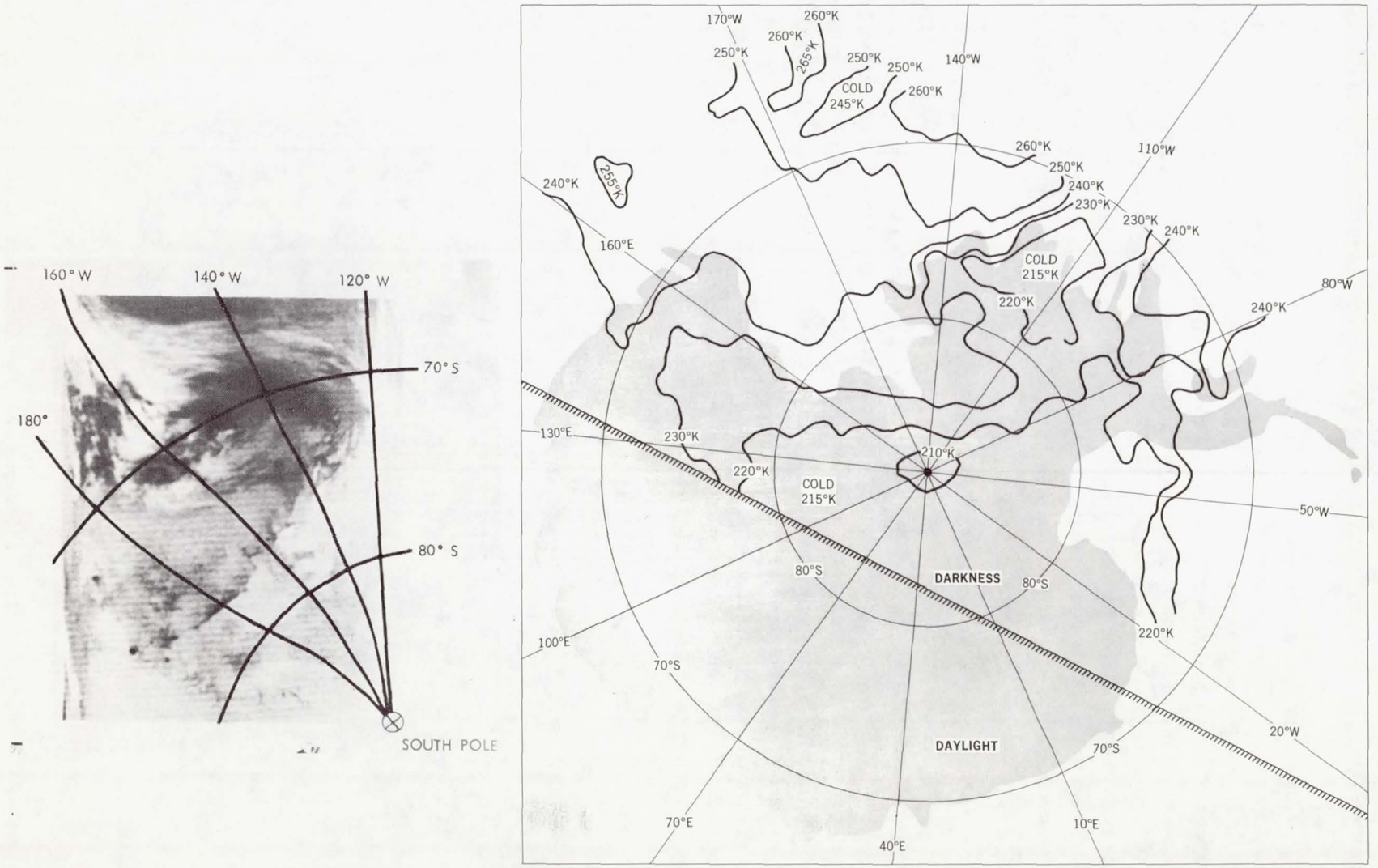

Figure 9—Ross Sea area: (a) HRIR photograph, orbit 058, September 1, 1964, (b) temperature contour map of the same area and the surrounding region.

are nearly the same over the interior ice. Surface temperatures of the Ross Ice Shelf range from 225°K near 85°S to 245°K near 70°S. The latter value compares well with the temperatures of 244°K measured four days earlier over the Weddell Sea pack ice (Figure 6b). Figure 9b is a temperature contour map of the Pacific sector of Antarctica derived from the automatically plotted digital data for the picture shown in Figure 9a. The very low temperatures (215°K) over the high plateau surrounding the South Pole are obvious. The warm tongue reaching toward the pole near 180 degrees longitude coincides with the Ross Sea where the shelf ice is located at a much warmer temperature than the higher and thicker inland ice. The high clouds seen in Figure 9a to the east of the Ross ice shelf show a temperature of about 215°K, which corresponds to a cloud top altitude equal to that of the interior plateau, namely about 3000 meters. The 260°K line indicates pockets of broken ice and open water which are found in the Pacific Ocean sector.

In Figure 10a a number of very isolated high temperature spots can be seen along the coast of Victoria Land. The most pronounced one near 76°S and 165°W has a temperature of 260°K. Since this spot is located near Mt. Erebus, it was originally suspected that these isolated warm regions might be related to volcanic activity. However, as the same regions were observed in subsequent HRIR pictures, it became evident that some of the spots became enlarged and formed small bands along the edge of the continent. Finally on 21 September 1964 the spot near Mt. Erebus had enlarged to such an extent that it filled the entire field of view of the HRIR (Figure 10b) and the measured temperature was approximately 270°K. The fact that this is conspicuously close to the temperature of freezing water and that the same spot was photographed 12 hours later in sunlight with the AVCS (Figure 10a) leads to the definite

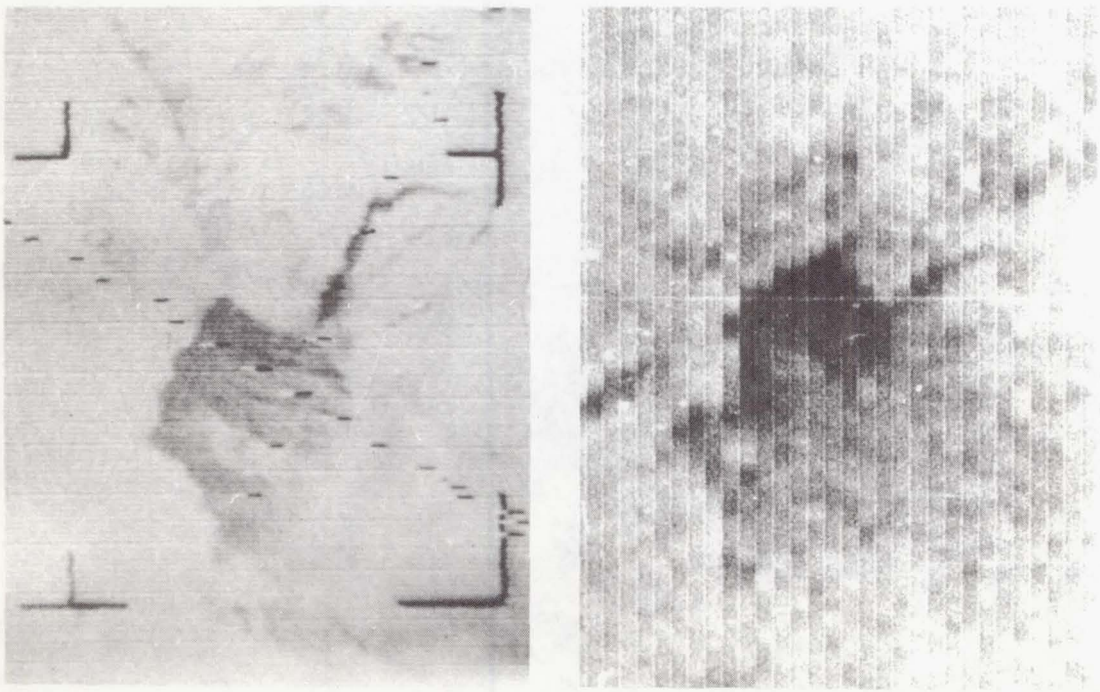

Figure 10—AVCS and HRIR photographs of a high temperature spot near Mt. Erebus: (a) AVCS, orbit 352, September 21, 1964, (b) HRIR, orbit 351, September 21, 1964.

conclusion that the spots indeed are open water. Note the identical shape of the open area in Figures 10a and 10b, despite the difference of one order of magnitude in the resolution capabilities of the AVCS and HRIR.

In general, both the AVCS and HRIR photographs from Nimbus are of excellent quality and coverage over the Antarctic is fairly complete. It appears quite feasible to map the entire Antarctic ice pack as well as the ice shelf surrounding the continent from these photographs. Such maps, together with an analysis of cloud cover over the south polar region, could be most helpful in studies of the meteorology and oceanography of the Antarctic area. Surface temperatures and snow and ice emissivities as determined from HRIR data should yield a wealth of information about actual surface characteristics. We now have in the Nimbus spacecraft a remarkable tool in evaluating many of the interesting and important features of one of the last frontiers on the earth's surface.

ACKNOWLEDGMENTS

The authors were very fortunate in being able to call upon a number of individuals with extensive experience in Arctic and Antarctic research to help with the identification of some of the various features photographed by Nimbus I. We are particularly indebted to Dr. A. P. Crary and Mr. Walter Seelig of the National Science Foundation for their comments on the Antarctic photography, to Mr. Frank Reilly of the Naval Reconnaissance and Technical Support Center for performing the shadow measurements, to Lt. William Dehn and Frank Lott, AG1, both from the U. S. Naval Oceanographic Office, Suitland, Maryland, and to Mr. Herbert Neiss and Edward Ferguson of the National Weather Satellite Center for help in assembling and analyzing much of the material.

Page intentionally left blank

EXAMPLES OF THE METEOROLOGICAL CAPABILITY OF THE NIMBUS SATELLITE

Lewis J. Allison
James S. Kennedy, Capt., USAF*
George W. Nicholas

INTRODUCTION

The purpose of this paper is to describe some of the meteorological capabilities of the Nimbus sensors. Nimbus I was the first meteorological satellite to be earth-oriented in a near-polar, sun-synchronous orbit. Nimbus was therefore able to view all parts of the earth and to record data continuously from an optimum attitude to reduce distortion and minimize the need for rectification of the data.

The meteorological sensors carried aboard the spacecraft consisted of two television systems, the AVCS and APT, and an infrared detection system, the HRIR. The television systems yielded information of unprecedented clarity and resolution but since, in principle, the meteorological information resulting from the Nimbus television pictures was similar to that obtained in the TIROS television cameras, this report will be mainly concerned with interpretations from the new high resolution infrared observations.

The High Resolution Infrared Radiometer (HRIR) was able to produce detailed depictions of cloud features on the dark side of the earth. In this regard, the HRIR acted as the nighttime counterpart of the television system but with a vital distinction. HRIR cloud observations introduced the important vertical dimension. In this report, several characteristic meteorological features, ranging from the mesoscale to planetary scale, are examined in light of this new observational method, with implications for future research and operational capabilities.

CLOUD HEIGHT MEASUREMENTS WITH THE HIGH RESOLUTION INFRARED RADIOMETER

When the HRIR views a cloud-covered region and a uniform cloud fills the instantaneous field of view of the radiometer, the average blackbody temperature of the cloud top surface can be derived (Foshee, Goldberg and Catoe, Paper No. II NASA SP). If the temperature in the troposphere decreases monotonically with altitude, and if the clouds do not penetrate to altitudes above the troposphere where the temperature generally increases with height, blackbody cloud-top temperatures can be directly related to height on the basis of climatologically assumed or independently measured temperature-height profiles. The derivation of cloud heights from

*USAF, Air Weather Service Member on temporary assignment to Goddard Space Flight Center.

satellite-borne radiometric measurements has been demonstrated previously with TIROS observations (References 1 and 2) but the better spatial resolution of the Nimbus radiometer permits, for the first time, a detailed pictorial presentation of the vertical structure of cloud tops on a large scale.

Figure 1 shows the relationship between accurate blackbody temperature (T_{BB}) measurements presented in the analog signal for a single scan, and the height of the cloud formation seen in the associated photofacsimile depiction of Hurricane Gladys.

The photofacsimile depiction of Hurricane Gladys and the analog trace are of the same horizontal (west to east) scale in Figure 1 and a given feature in the picture corresponds to the same feature in the analog trace directly underneath. This scan covers a strip of 5km width across the center of the storm and increasing widths toward the horizons. The observed radiation intensities expressed in degrees K, are measured along the ordinate. The blackbody temperatures were converted to height on the basis of actual temperature soundings performed by radiosonde balloons in the vicinity of the storm and the corresponding heights are shown along the right hand ordinate. The photofacsimile presentation of the storm in Figure 1 is

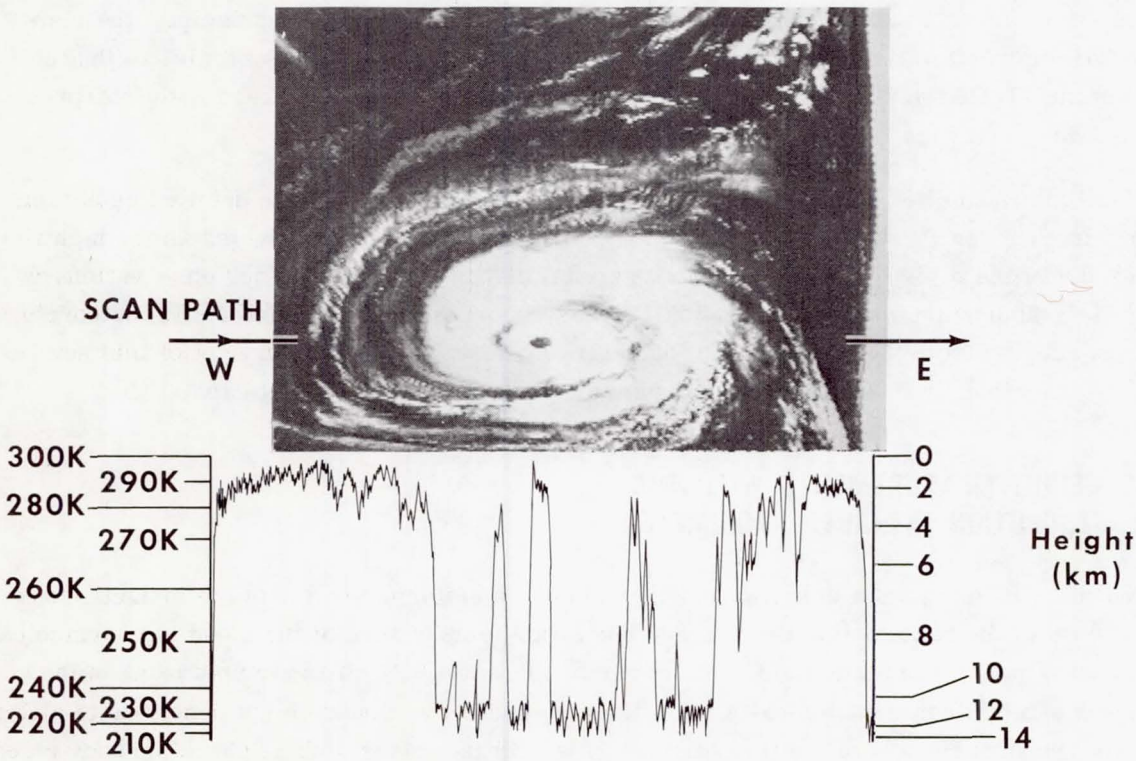

Figure 1—An HRIR depiction of Hurricane Gladys. The HRIR photofacsimile picture of the hurricane is compared to a single analog trace through the eye of the hurricane. The shades of gray in the photofacsimile display are related to blackbody temperature values by the gray-scale wedge on the right, and the analog trace is related to blackbody temperature given on the lefthand ordinate. Height above sea level (righthand ordinate) is related to blackbody temperature by the 0000 U.T., September 18, 1964 radiosonde sounding from Kindley Air Force Base, Bermuda. The HRIR data were recorded on orbit 305 at 0422 U.T., September 18, 1964.

composed of a total of about 200 such scans. On this particular orbit, the spacecraft passed directly over the eye of Gladys where the response of the radiometer is shown dramatically by the highest central spike. The highest temperature recorded in the eye was about 285°K so that the HRIR was able to distinguish drastically between the underlying cloud surface, at an altitude of about 2km, and the very high clouds surrounding the eye. In the central region of the storm, quite cold temperatures were recorded over the high dense cloud shield. These temperatures were in the vicinity of the noise-equivalent temperature of the instrument at 210°K, which is the low limit of accurate resolution.

To the west of Gladys may be seen thin wispy spiral bands of couldiness. In the absence of conventional weather data, this cloudiness was judged to be thin cirrus. It is of interest to note that the lowest T_{BB} values recorded in this region do not fall below 270°K. The cirrus is semi-transparent and allows radiation from the warmer regions below to pass through it. The problems this poses in cloud height interpretation will be discussed more fully in the next section.

It may be noted that at each end of the analog trace, there is a slight falloff of temperature. This is due to limb-darkening and is consistent with Kunde's theoretical analysis (Paper No. III, in this NASA SP). The total length of the scan shown in Figure 1 represents a length of 5000 km on the surface of the earth, since the altitude of the satellite was approximately 540 km. The scan and the photofacsimile depiction are both linear with respect to the radiometer mirror rotation rate from left to right, and as a result, there are large distortions near the horizons. The central 2500km of the analog trace occupies 92 percent of the length of the analog trace.

SELECTED EXAMPLES OF NIMBUS OBSERVATIONS OF METEOROLOGICAL SIGNIFICANCE

Several case studies of meteorological features ranging from planetary scale to mesoscale are discussed in this section.

Hurricane Dora

In the previous section, the relationship between radiometer determined cloud-top temperatures and cloud heights along a single analog trace was illustrated. In this section, an analyzed field of equivalent blackbody temperatures chosen from a large number of scans will be discussed.

The region from approximately 20°N to 50°N in Figure 2 was chosen for the analysis. Incidentally, this figure shows how a portion of a single orbital strip can be used to identify and locate large scale synoptic features. An old occluded cyclone is clearly shown over northeastern Canada near 60°N, 70°W, with stationary frontal cloudiness trailing over the Great Lakes. At about 5°N, there is a band of cloudiness approximately 1500km long, associated with the Intertropical Convergence Zone (ITC). Near the center of the figure may be seen the large, nearly symmetrical, tropical cyclone, Hurricane Dora.

Dora apparently developed from a weak low pressure disturbance which moved off the west African coast on August 28, 1964 (Reference 3). The first view of Dora recorded by the

NIMBUS I HRIR
174 R/O 178
9 SEPT. 1964 0530Z
HURRICANE DORA

Figure 2—An HRIR photofacsimile film strip showing Hurricane Dora for orbit 174 at 0530 U.T., September 9, 1964.

Nimbus HRIR was at 0255 U.T., September 2, shortly after Dora had intensified to tropical storm stage. This is shown in Figure 3a where Dora is near 12°N, 48°W. Slightly more than 24 hours later, Dora was again observed by the Nimbus HRIR, as shown in Figure 3b. Dora had been classified a hurricane just shortly before the time of the later photograph.

Both views of Dora show that the central region of the storm was covered by a widespread canopy of apparently opaque cirrus. The uniformity of the cirroform canopy suggests that either the cloud tops were at a fairly uniform temperature or that the cloudtop temperatures fell below the noise equivalent temperature of 210°K.

TROPICAL STORM DORA
70 R/O 75
2 SEPT. 1964 0255 U.T.
(a)

HURRICANE DORA
85 R/O 90
3 SEPT. 1964 0330 U.T.
(b)

NIMBUS I
HRIR

Figure 3—HRIR photofacsimile depictions of Dora; (a) shortly after tropical storm stage had been reached on orbit 70, 0255 U.T., September 2, 1964, (b) shortly after hurrican stage had been reached on orbit 85, 0330 U.T., September 3, 1964.

Riehl (Reference 4) and Yanai (Reference 5) have constructed models of hurricane genesis in which an initial, cold core disturbance is transformed into a warm core disturbance. Riehl, in particular, has suggested that the effect of a high cloud deck on outgoing longwave radiation, together with the release of latent heat of condensation, may be instrumental in the transformation to a warm core. Yanai's model shows the warming occurring first at the 300 to 400 mb level and gradually expanding downwards.

Atmospheric radiation effects are relatively slow processes but according to Yanai's examination of Typhoon Doris of 1958 (Reference 5), the warming of the core was an extremely slow process during which there was no abrupt change of the characteristics of the disturbance. Yanai found that during the creation of the warm core, the warming effect due to latent heat of condensation and the cooling effect due to ascending motion was nearly balanced. The near balance of convective effects, again, suggests that radiative effects might be important in tipping the balance towards net warming. In this regard, the Nimbus HRIR is a potentially valuable source of information on lateral extent and height of the cirrus canopy.

Dora was next viewed by the Nimbus HRIR at 0530 U.T. on September 9, 1964, as was seen in Figure 2. Figure 4 is an enlarged view of the region chosen for an analysis of equivalent

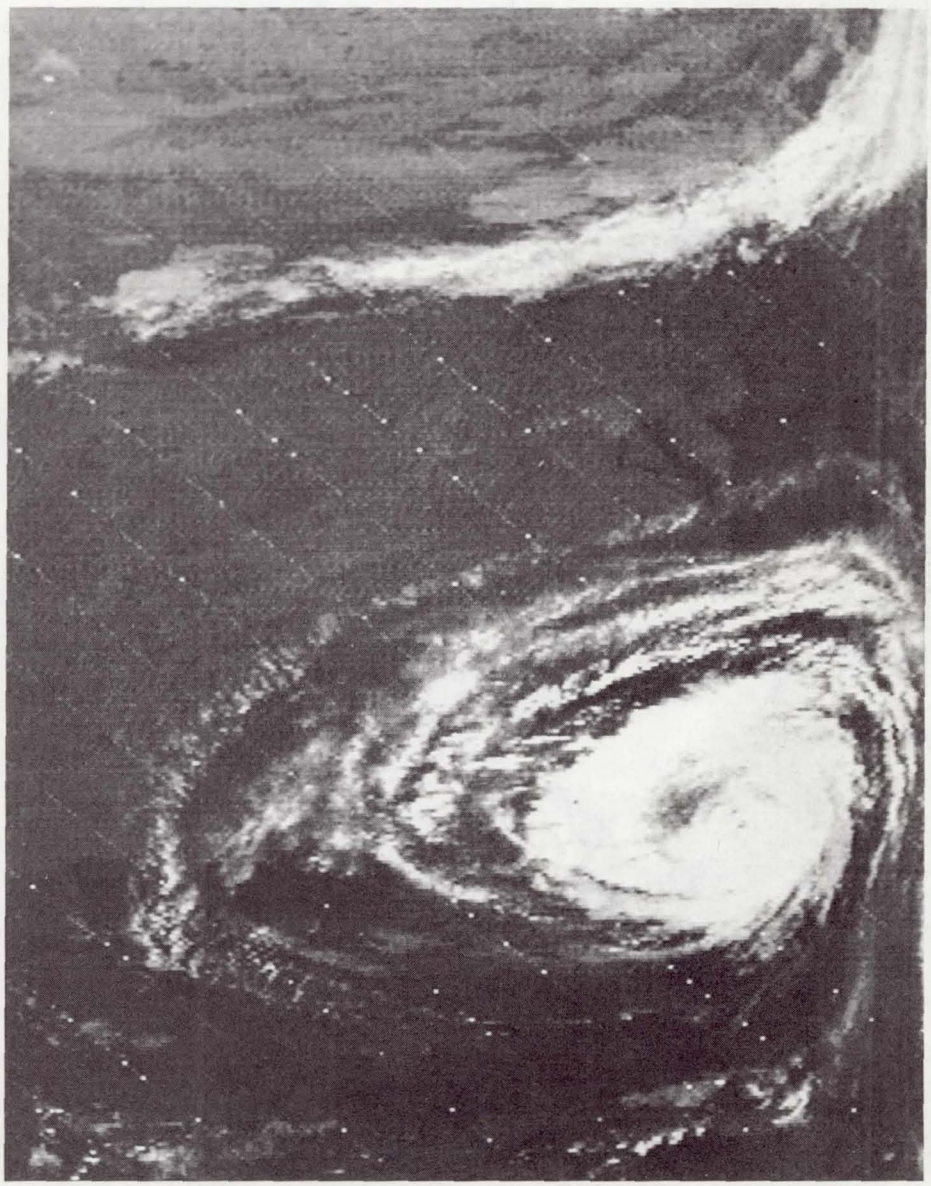

Figure 4—An enlarged HRIR photofacsimile depiction of Hurricane Dora and the eastern United States taken on orbit 174, 0530 U.T., September 9, 1964.

blackbody temperatures. The eye of Dora was approximately 90 miles east of Daytona Beach, Florida at this time. In the northwest quadrant of the storm, there are several bands of cloudiness becoming more diffuse as distance from the center of the storm increases. The outermost band crosses the Gulf coast near Appalachicola, Florida and the Atlantic coast near Norfolk, Virginia. Beyond the outer band of cloudiness, the skies appear clear over the eastern United States and the coastlines from New York to Norfolk and portions of the Gulf coast are visible. The frontal cloudiness appears well organized as far west as 80°W, where the cloud pattern becomes broken and diffuse. North of the front, there appear patches of lower clouds, but the pattern is ill defined.

There is a large kidney shaped break in the clouds near the center of the storm. This is not the eye of the hurricane. By closely examining the cloud streaks and apparent circulation in the HRIR depiction, the true eye was estimated to be approximately 60 miles to the southeast of this break. The estimated position of the eye was verified by radar and aerial reconnaissance observations. as may be seen in Figure 5. The radar depiction of Dora fourteen hours later also shows a large dark gap in the spiral bands northwest of the eye.

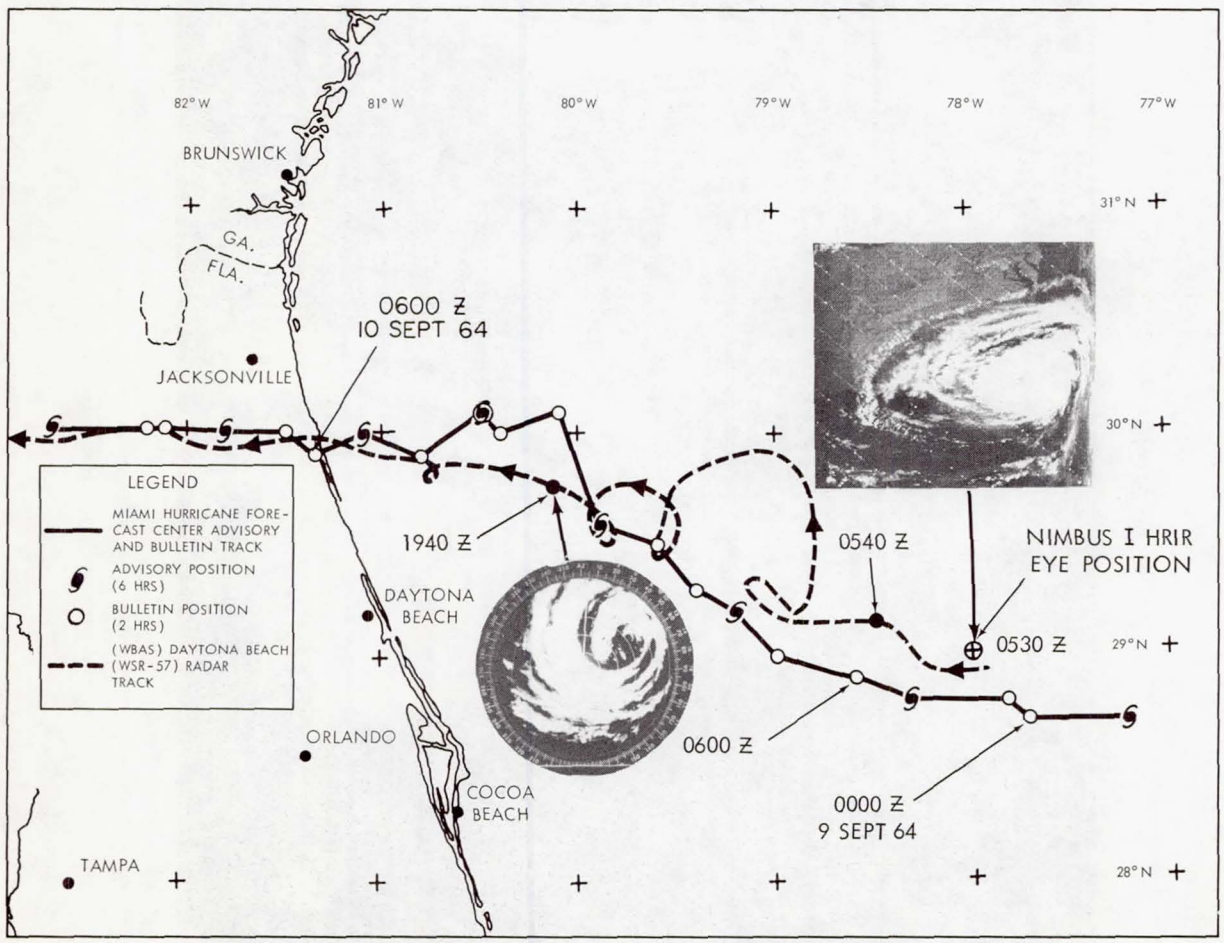

Figure 5—Path of the eye of Hurricane Dora as determined by aerial reconnaissance (solid line) and Daytona Beach WSR-57 (dashed line) for September 8-10, 1964. The position of Hurricane Dora as determined from the HRIR data is shown for 0530 U.T., September 9, 1964.

The surface synoptic chart for 0600 U.T., September 9, Figure 6 shows Dora approaching an area dominated by an anticyclone centered in northern Virginia. Low cloudiness is confined to eastern Florida and the Atlantic coast, northward to Myrtle Beach, South Carolina. Widespread cirrus is confined to the area south and east of a line connecting Norfolk, Virginia, Athens, Georgia, and Pensacola, Florida. To the north and west of this line, the skies are generally clear with a few scattered reports of cirrus, northward to the vicinity of the front along the Great Lakes. The front is shown as a cold front east of Detroit, Michigan and stationary to the west. The point where the front becomes stationary is approximately where the dense, high-altitude cloudiness, observed by the HRIR in Figure 4, ceases.

The 200 mb chart (Figure 7) for 0000 U.T. September 9, 1964, shows a very flat pattern over the southeast United States. The only height variation is due to the warm anticyclone associated with Dora. To the north, there is a weak to moderate jet stream associated with the surface front, with maximum winds of about 95 knots.

For the analysis of T_{BB}, temperature values were extracted from every fifth scan trace, hand plotted and analyzed. The result is shown in Figure 8. Comparing the analysis with the

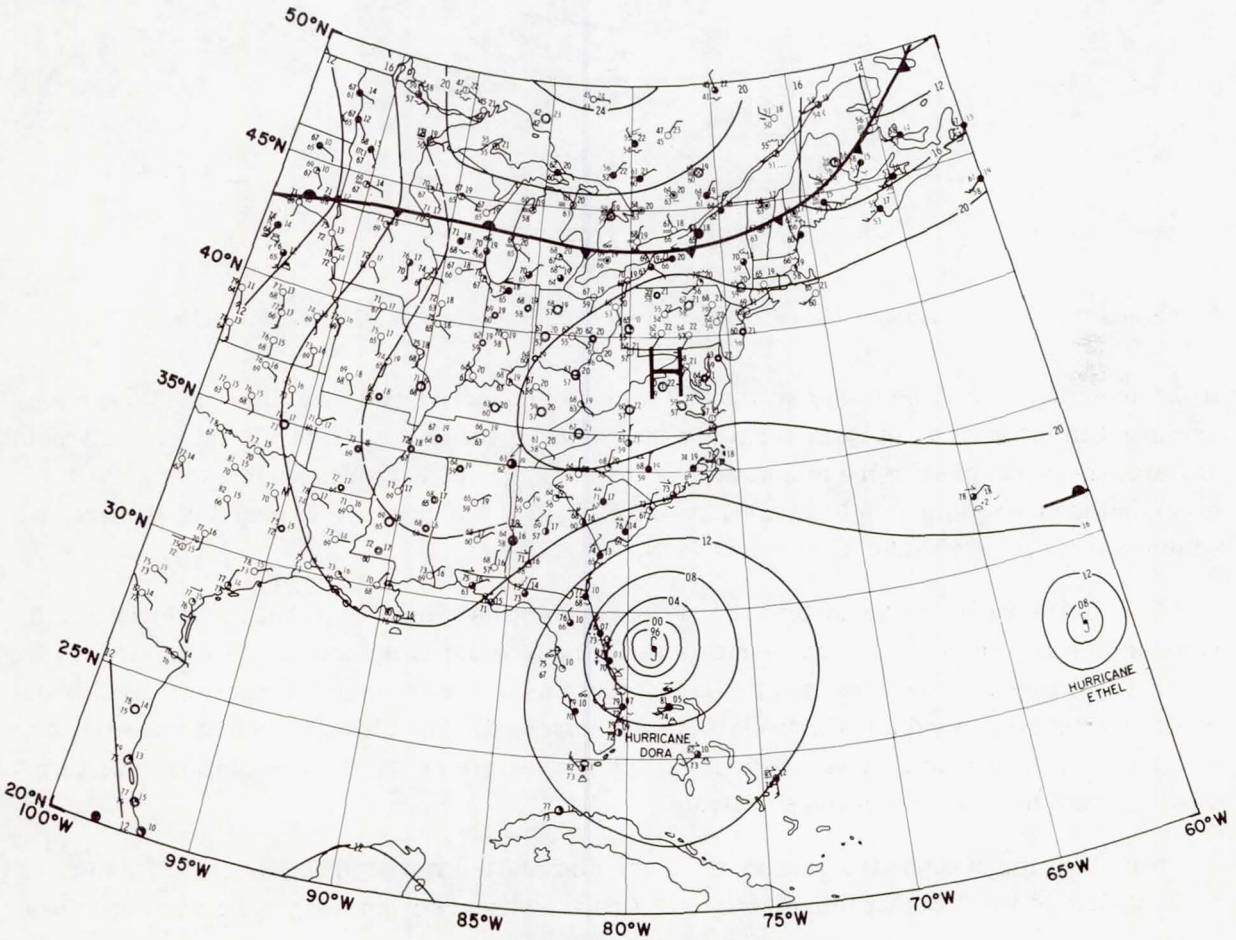

Figure 6—Surface synoptic chart of eastern North America, 0600 U.T., September 9, 1964.

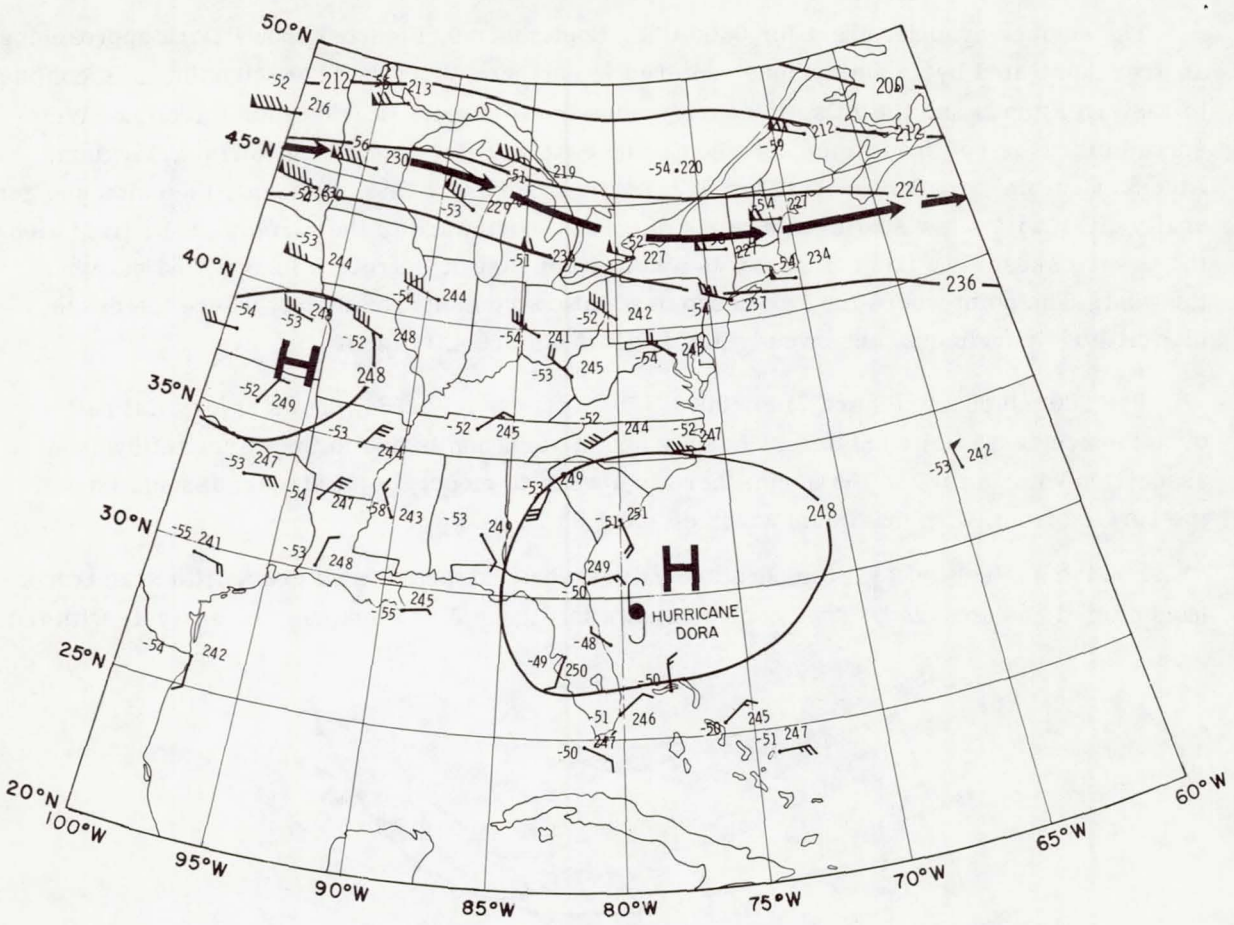

Figure 7—200 mb constant-pressure chart of eastern North America, 0000 U.T., September 9, 1964.

HRIR depiction, it may be seen that the 280°K isotherm served well as a cloud/no cloud discriminant in the vicinity of Dora and along the southern edge of the front. In the central region of Dora, the warm area in the temperature range of 260°-280°K corresponding to the dark break in the cloud picture is located near 30.5°N, 79°W. The true eye is near the smaller and colder warm spot (240°-260°K) shown at 29°N, 78°W.

The cirrus bands in the northwest quadrant are outlined quite well, but the temperatures found in this region are much warmer than temperatures normally associated with cirrus. The warm T_{BB} values may be attributed to the fact that the cirrus is semi-transparent and that the patchy cirrus probably did not entirely fill each scan spot. The identification of thin cirrus will probably depend on its characteristic shape and texture on the HRIR depiction for future cases, rather than on temperature analysis.

Not all of the stations lying under the outer cirrus band reported cloudiness. This is probably due to the fact that thin cirrus is difficult to observe from the ground on a moonless night.

Between the outer cirrus band and the frontal cloudiness, the isotherm analysis shows a very homogeneous area. Temperatures in this cloud-free region are generally above 280°K.

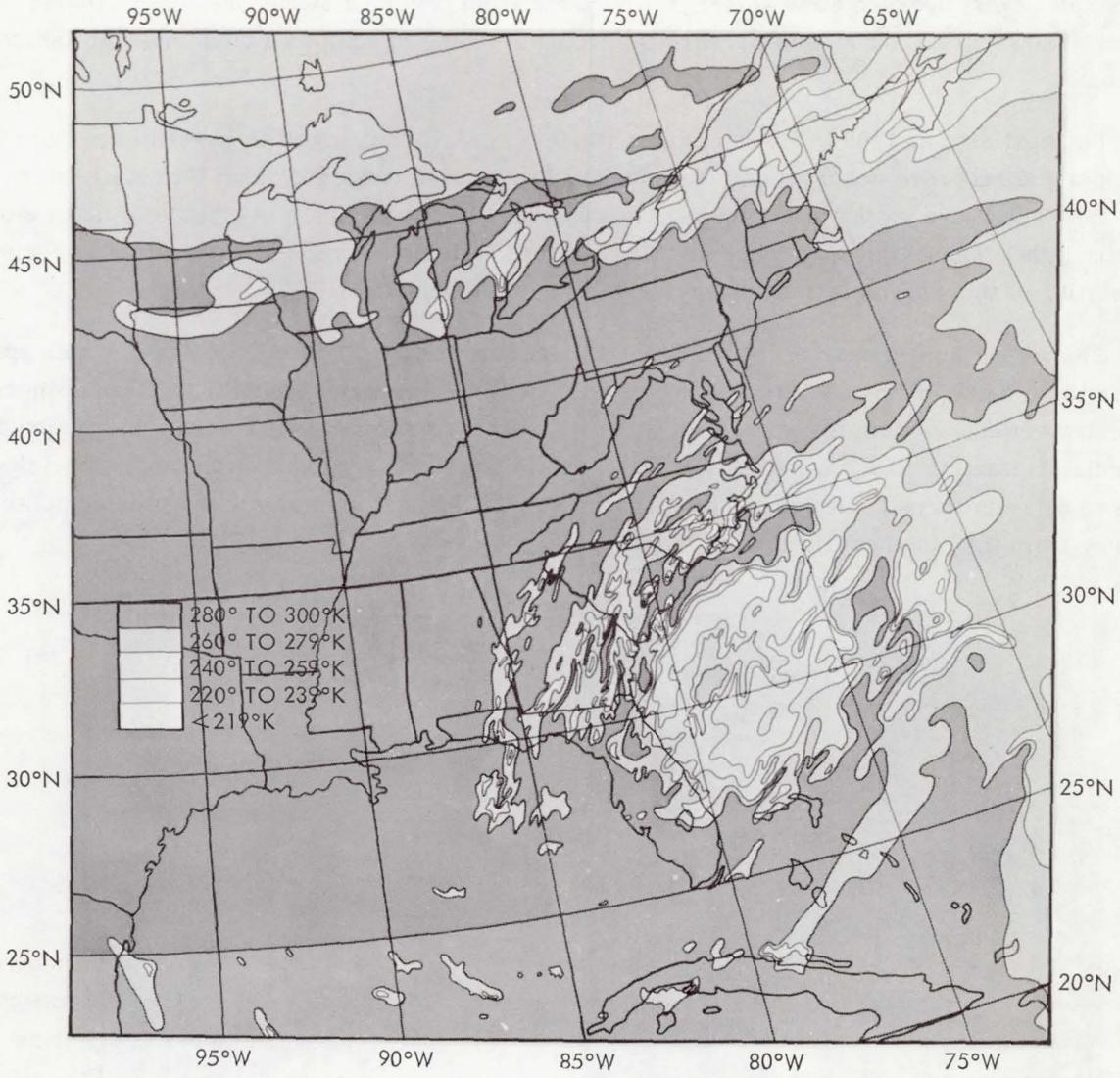

Figure 8—Analysis of T_{BB} values over Hurricane Dora for 20°K intervals from orbit 174, 0530 U.T., September 9, 1964.

The satellite-observed isotherm pattern does not show any indications of the cloudiness over Louisville, Kentucky or Chattanooga, Tennessee, as reported in the conventional meteorological observation. This is probably due to gaps in the temperature analysis or possibly due to small gaps in the earth coverage of the HRIR due to the low altitude of the satellite at that time.

Air-shelter temperatures for about forty stations, which reported clear skies, were compared with the satellite-observed T_{BB} values. The results showed that the blackbody temperatures derived from the satellite radiation measurements averaged 5°K colder than the air shelter temperatures. This was to be expected, since the Nimbus radiometer responds primarily to ground surface temperature, which is generally lower than air shelter temperature on clear nights with light wind.

The isotherm analysis of the frontal region shows a smoother pattern than that of Hurricane Dora. However, between 80°W and 85°W where the front becomes stationary, the isotherm pattern shows a distinct loss of organization corresponding to scattered cloudiness of the frontal system.

The next day, at 1700 U.T., September 10, 1964, the Nimbus satellite passed over Dora in daylight and recorded observations with the HRIR and the Advanced Vidicon Camera System (AVCS). These are shown in Figure 9. The daylight HRIR depiction was printed to make clouds appear light. Thus, lighter regions are those from which higher values of energy are received, consisting of thermal emission but primarily of reflected sunlight.

Clouds and land appear to have a large diffuse reflectivity. The reflectivity of water appears to be much less except for the bright strip near the center of the HRIR depiction where specular reflection from the water was received by the radiometer. Apart from the region of specular reflection, cloud patterns are rather well defined over water. Over land, some clouds tend to be indistinguishable from land when the sum of thermal emission and reflected solar energy from the cloud equals that from the land.

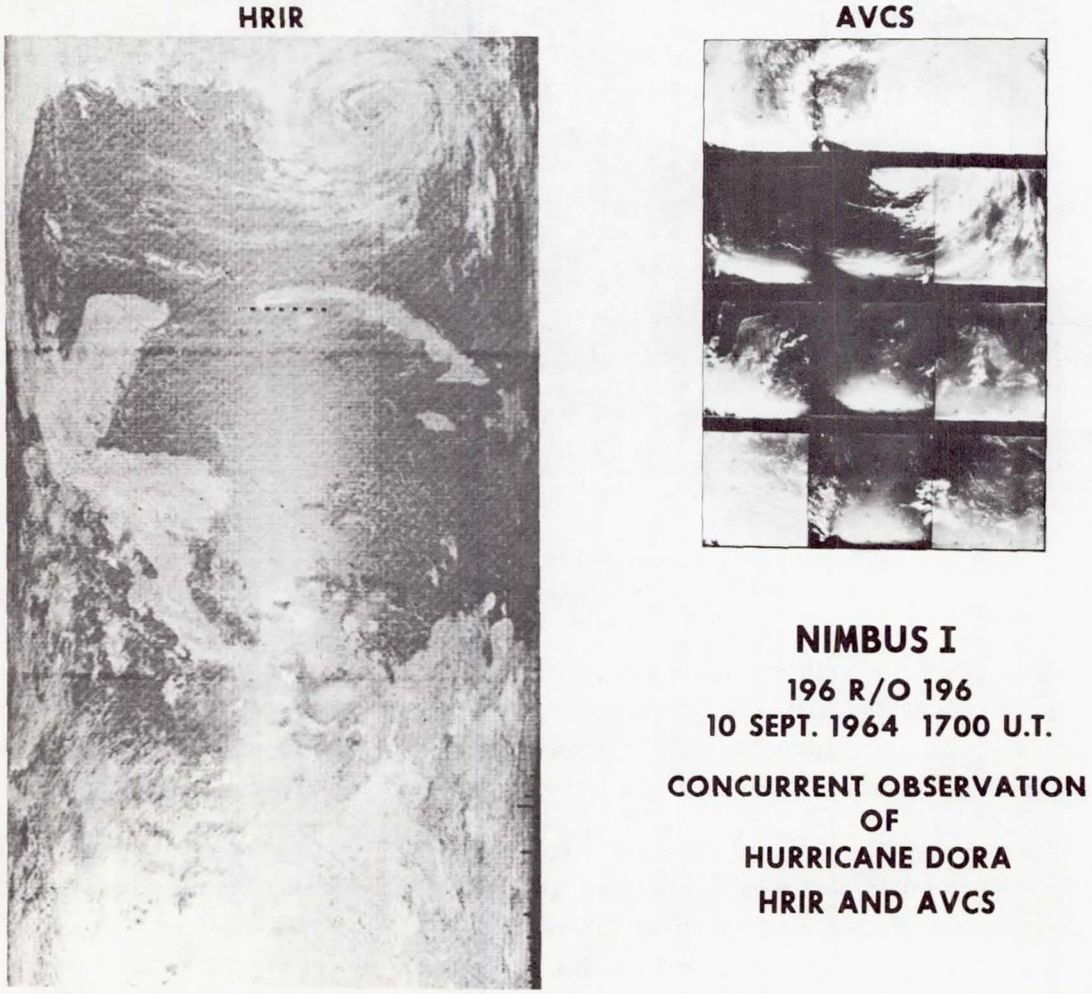

Figure 9—Comparison of concurrent observations of Hurricane Dora by HRIR in daylight and AVCS on orbit 196, 1700 U.T., September 10, 1964.

On the AVCS photo over eastern Cuba there appears thin scattered cloudiness. The HRIR apparently did not resolve this thin cloudiness since, in the HRIR picture, the coastline of Cuba appears to be free of clouds.

While HRIR observations in daylight are useful in defining gross patterns of cloudiness, meaningful estimates of cloud-top temperature and, therefore, of cloud heights cannot easily be derived. However, in clear skies, the angular variation of the reflectivity of water can be studied by subtracting the thermal emission component based upon climatological sea surface temperatures from the total energy measured by the radiometer.

Indian Ocean and West Pacific Ocean Area

With the Nimbus HRIR data, it is now possible to analyze the vertical extent of clouds over large inaccessible areas such as the Indian Ocean, on a routine nightly basis.

Figures 10 and 11 illustrate the HRIR mesoscale coverage over the Indian Ocean on August 30 and September 10, 1964 at approximately 1800 U.T. Two synoptic features which are common to both figures are the high-altitude clouds along the equator and over the Tibetan Plateau, and the clearer skies over the Bay of Bengal and Arabian Sea. A heavy cloud shield occurs over India, centered at 15°N, 80°E on September 10, (Figure 11) while a less intense cloud region is shown over India on August 30, in Figure 10.

The period August 30 to September 10, 1964 occurs at the beginning of the season of the retreating monsoon over India (September to December). As the low over Northern India loses

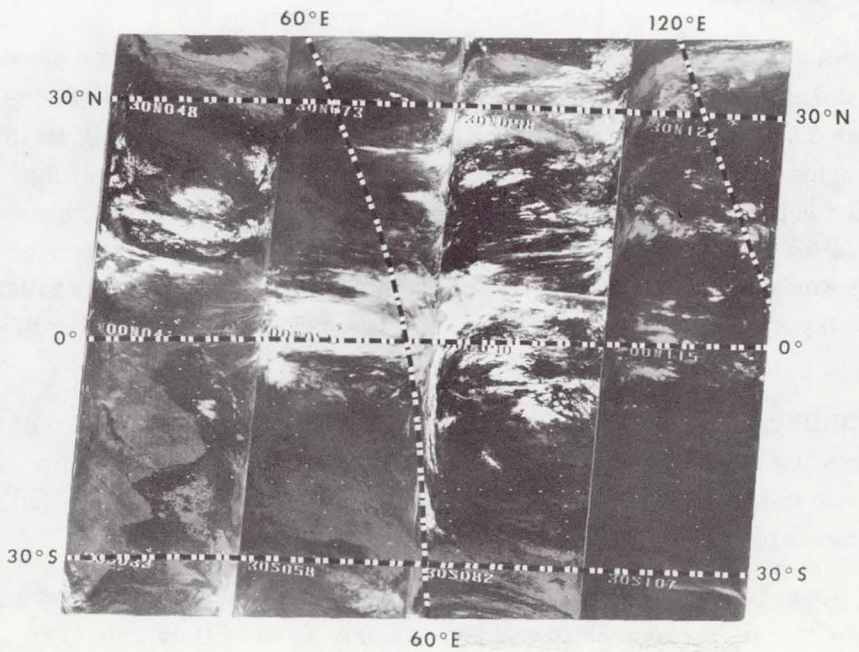

Figure 10—Composite of HRIR photofacsimile depictions for four adjacent orbits over the Indian and Western Pacific Oceans on orbits 34, 35, 36, and 37 on August 30, 1964.

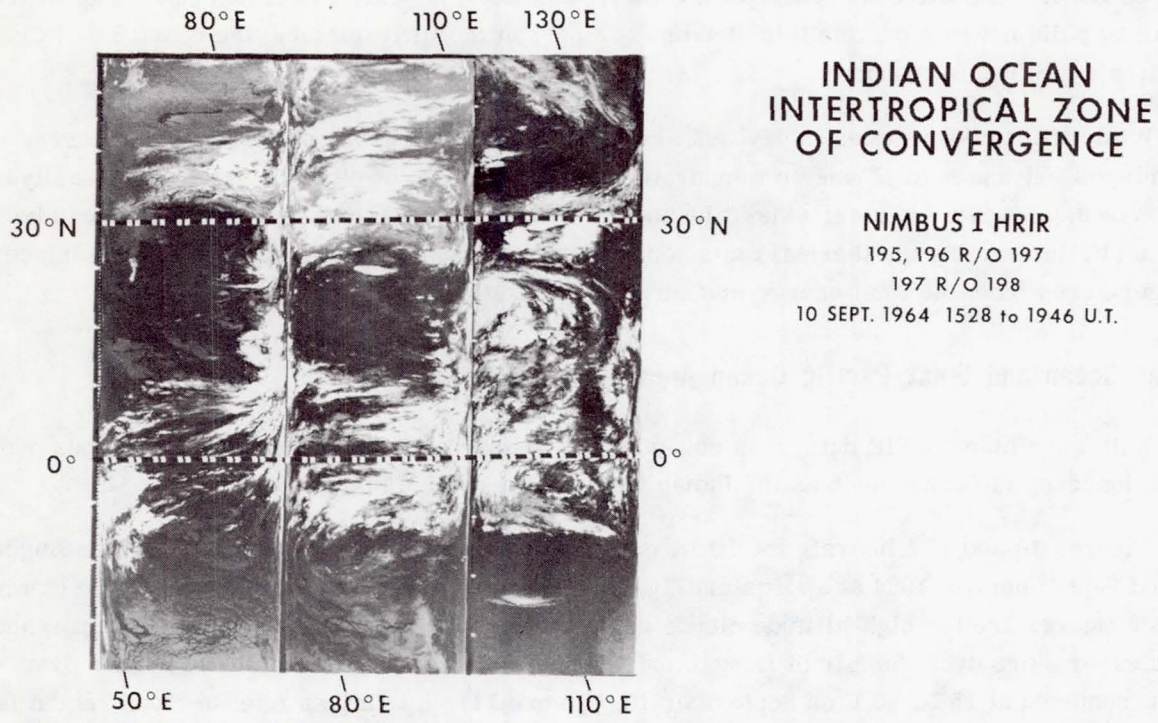

Figure 11—Composite of HRIR photofacsimile depictions for three adjacent orbits over the Indian and Western Pacific Oceans on orbits 195, 196, and 197 on September 10, 1964.

its intensity, the southwesterly flow of maritime tropical air across India decreases and cloudiness and rainfall diminish in the north.

The high dense cloudiness across the equator occurred in a region of wind shear as shown by the limited wind data on the above dates in that area. In the region from 65°E to 100°E, the prevailing wind direction was SW through NW from 0° to 10°N, and E through SE from 0° to 15°S. The synoptic data for this period were provided by the International Indian Ocean Expedition, International Meteorological Center, Bombay, India. On the basis of climatological data, wind circulation cells can occur in this cloudy convergence zone between the equatorial westerlies and zonal easterlies and various kinds of perturbations ranging from monsoonal depressions to hurricanes can develop. One such perturbation, Typhoon Sally, can be seen in the right center of Figure 11.

Digital analysis of the HRIR data resulted in the computer-produced map (Figure 12a) of blackbody temperature ranges for orbit 195, September 10, 1964 over the typhoon. By comparing the digital analysis with the photofacsimile depiction for the same region (Figure 12b), one may assign accurate temperature values to the cloud features of the storm.

Figure 13 presents the Guam Weather Central surface analysis for 1200 U.T., September 10, 1964 and indicates the position of Typhoon Sally and two easterly waves. Only four gray tones were selected to display the computer analysis in order to simplify the visual presentation of the 100 temperature intervals resolvable in the digital analysis. The edge of picture distortion, usually shown on the photofacsimile strips, has been rectified in the equatorial

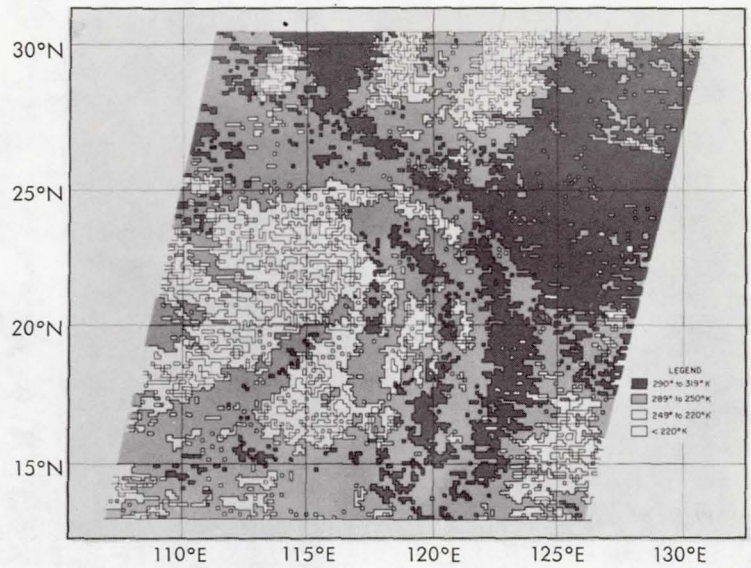

(a)

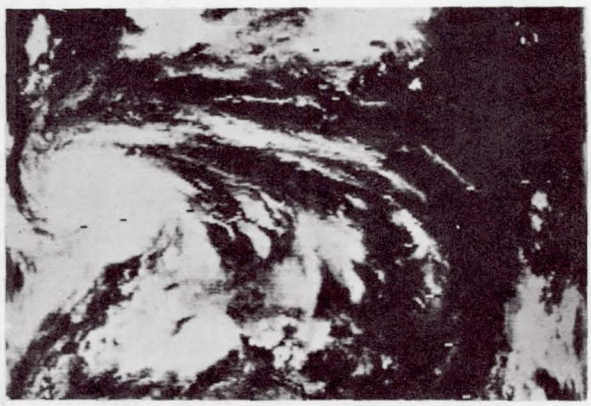

(b)

Figure 12—An HRIR view of Typhoon Sally at 1528 U.T. on September 10, 1964: (a) an analysis of computer produced blackbody temperatures, (b) photofacsimile depiction.

mercator projection. Blackbody temperature values can be readily assigned to the cirrus canopy streamers from Typhoon Sally, the easterly wave cloudiness, and the relatively clear ocean regions.

Cross-Section along 140°E

The following case study was selected because it depicted a cloudy frontal zone in the Western Pacific Ocean, a strong polar jet stream aloft, an active typhoon, and a clear oceanic region of warm convergent currents.

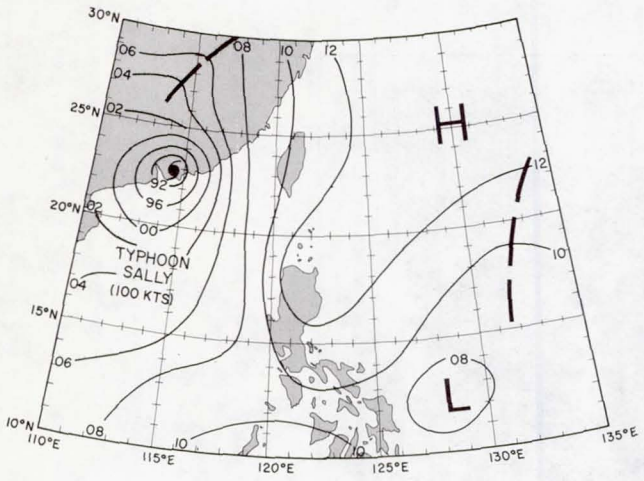

Figure 13—Surface synoptic chart of the Western Pacific Ocean, 1200 U.T., September 10, 1964.

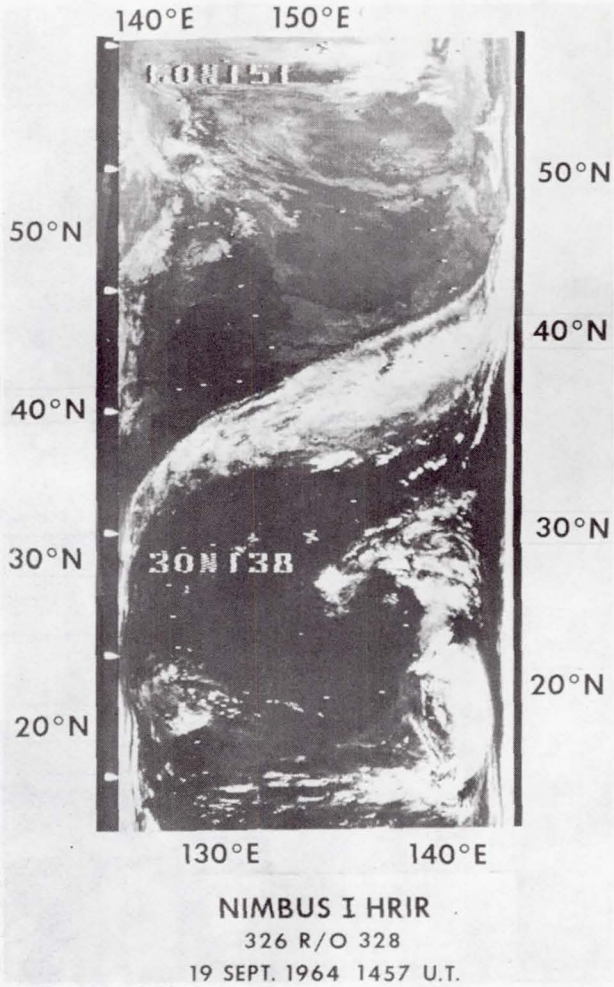

Figure 14—An HRIR photofacsimile depiction of the Western Pacific Ocean showing Typhoon Wilda near 18°N, 144°E and a band of frontal cloudiness in the vicinity of Japan on orbit 326 at 1457 U.T., September 19, 1964.

Figure 14 shows Typhoon Wilda in the lower right, at 20°N, 142°E approximately, and a stationary front across southern Japan in the center on September 19, 1964 at 1457 U.T. Hokkaido and portions of Sakhalin and E. Siberia are clearly visible to the north and west of the front.

A 1200U.T. surface weather chart and 300, 250, and 200 mb charts for September 19, 1964 were analyzed to show details of surface frontal cloudiness and to demarcate the jet stream position aloft (Figures 15 and 16). Good agreement was found between the Nimbus HRIR data in Figure 14 and the extensive cloudiness over the surface front and Typhoon Wilda, shown in Figure 15.

Two cross-sections, Figures 17 and 18, based upon 1200 U.T., September 19, 1964 conventional radiosonde data (Reference 6), were drawn along 140°E in order to compare the Nimbus HRIR data with temperature, humidity, and isotachs in the vertical. The HRIR data used were obtained from a computer-produced digital analysis of blackbody temperatures on a scale of 1:5 million, over the same area.

The temperature and temperature-dewpoint difference data in Figure 17 suggested the placement of the Japanese stationary front near 35°N, in good agreement with the 130-knot jet stream core in Figure 18.

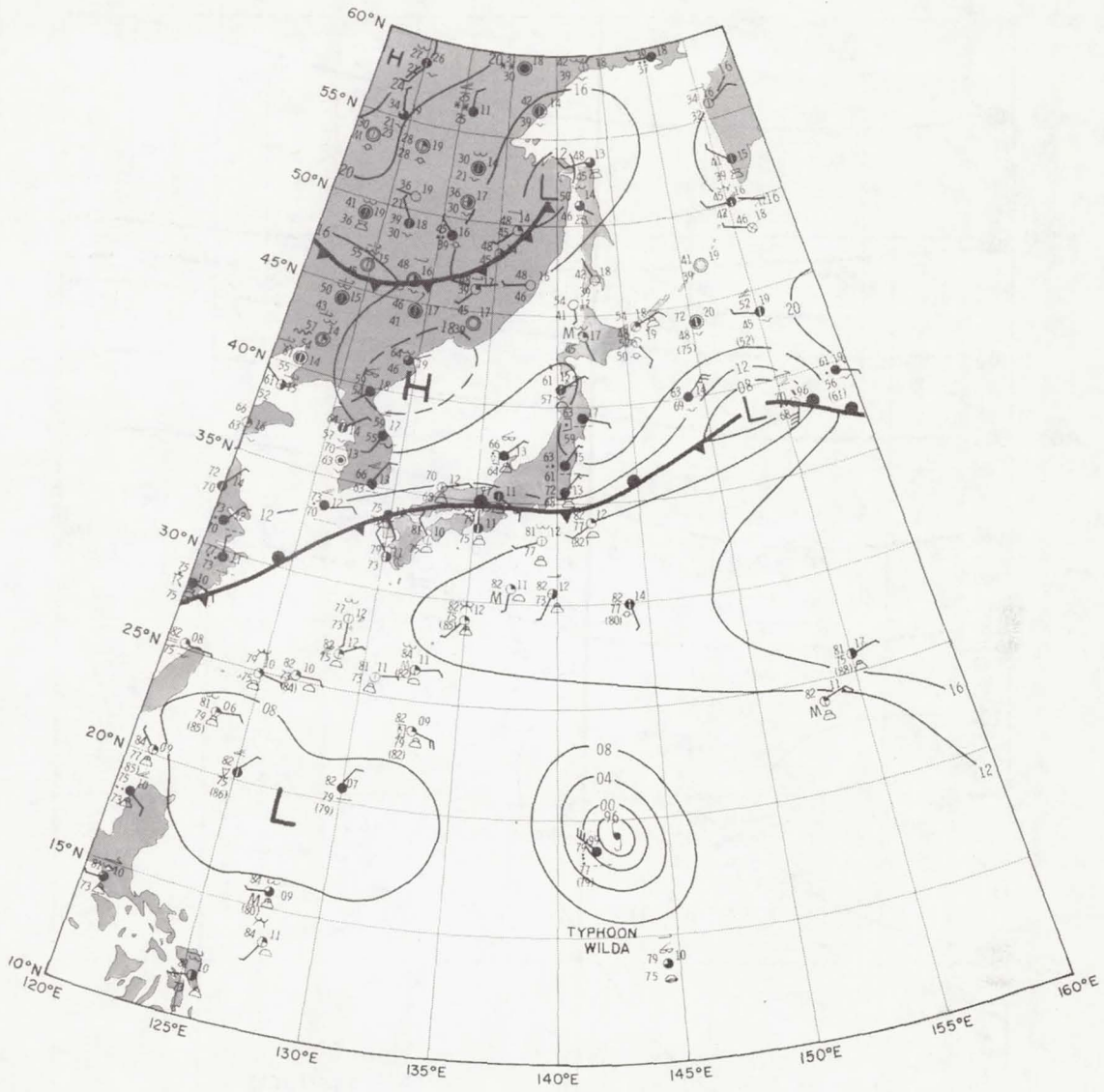

SURFACE ANALYSIS
19 SEPT. 1964 1200U.T.

Figure 15—Surface synoptic chart of the Western Pacific Ocean, 1200 U.T., September 19, 1964.

The HRIR T_{BB} data along 140°E were converted to effective radiation height by use of the radiosonde temperature-height data and are shown as the heavy solid line in Figures 17 and 18.

The HRIR T_{BB} trace (inferred cloud top altitudes) drops sharply in the relatively dry, clearer air over Hachijojima (33°N), rises sharply over the moist multi-layered frontal clouds from 34°N to 39°N, and drops again in the dry clearer air over Hokkaido (45°N). The T_{BB} trace continues to rise steadily northward over the moist middle and high clouds associated with a weak low over eastern Siberia and Sakhalin.

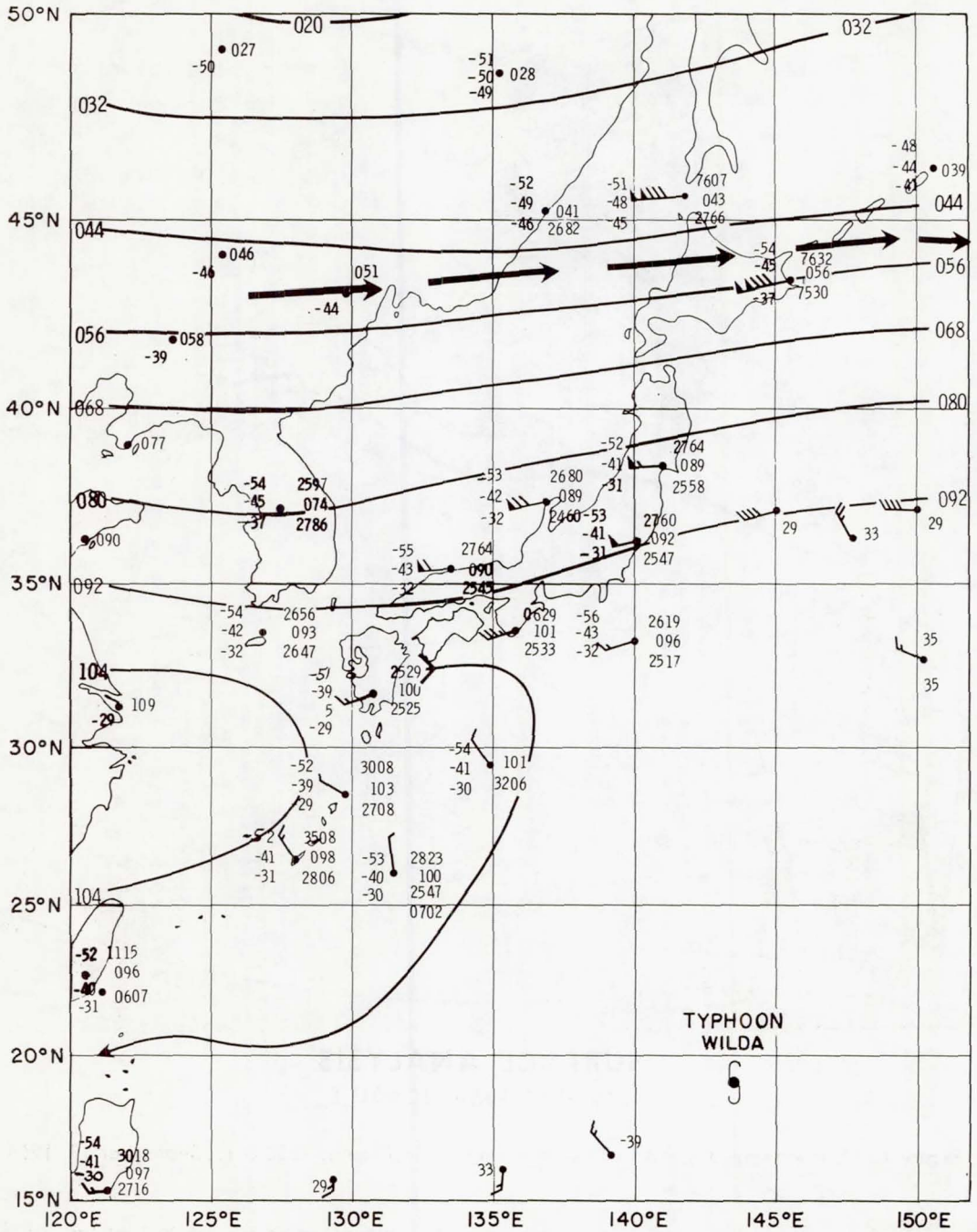

Figure 16—Constant pressure chart (300, 250, and 200 mb) of the Western Pacific Ocean, 1200 U.T., September 19, 1964. A station model for this three-level chart is explained as follows:

200 mb Temp (°C) - 53°
250 mb Temp (°C) - 41°
300 mb Temp (°C) - 31°

2760 (200 mb wind direction and speed (270°, 60 knots)
092 (250 mb height (10,920 meters)
257 (300 mb wind direction and speed (250°, 47 knots)

250 mb wind (270°, 50 knots)

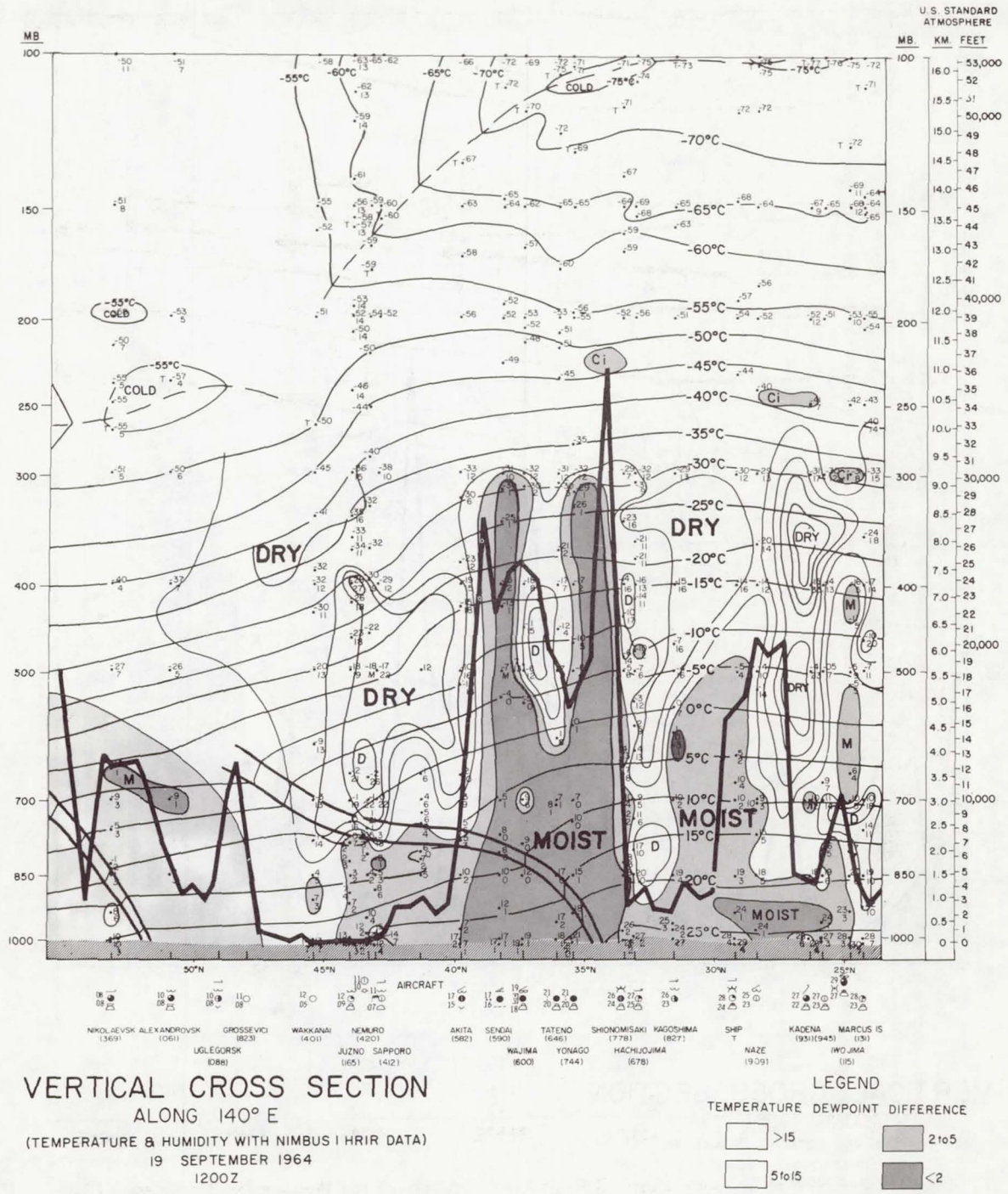

Figure 17—Cross-sectional analysis of temperature (°C) and temperature-dew point difference (°C) along longitude 140°E for 1200 U.T., September 19, 1964. Equivalent blackbody temperatures (heavy line) along 140°E were derived from a digital analysis based on a 1:5 million grid print map from orbit 326 at 1457 U.T., September 19, 1964.

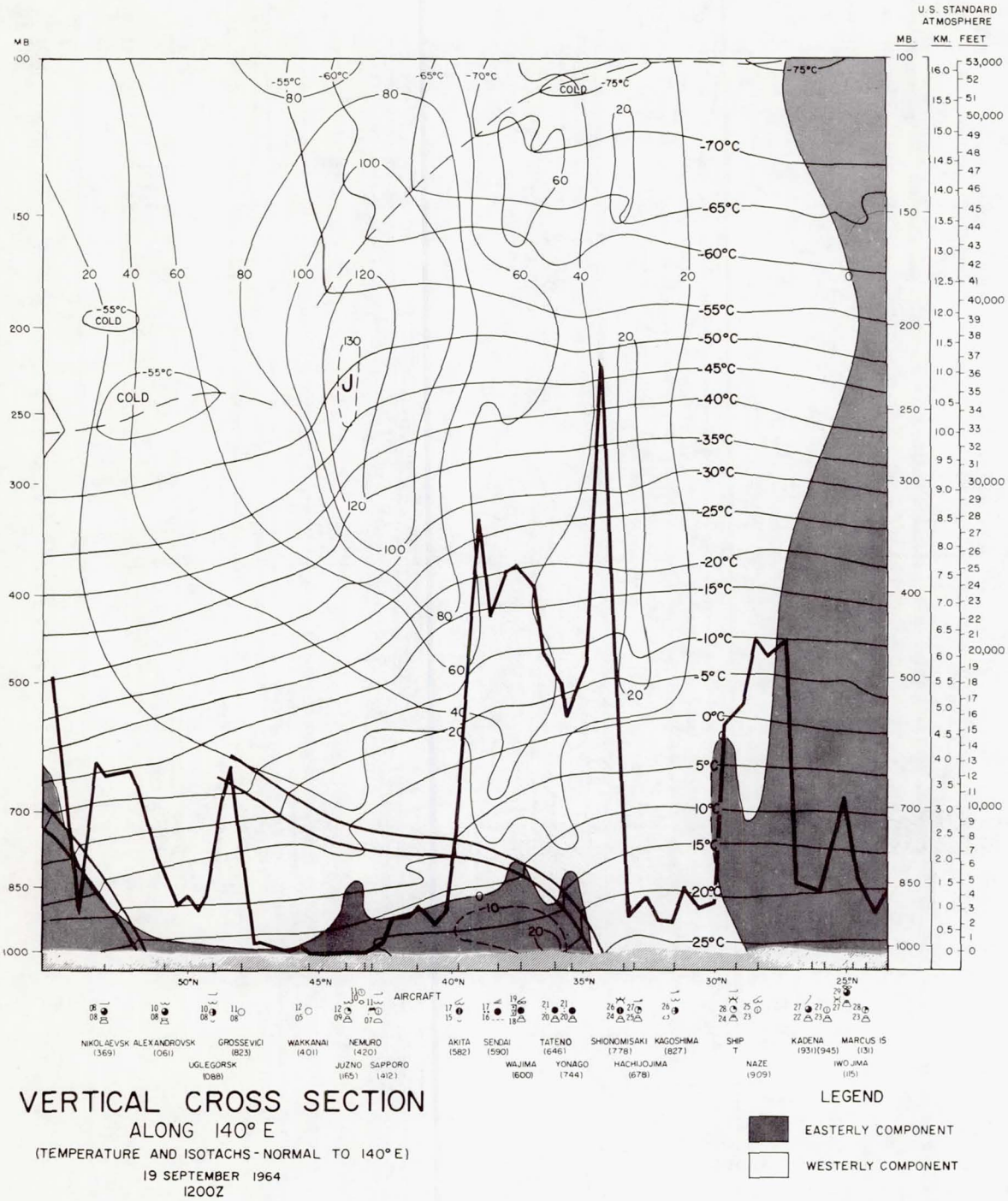

Figure 18—Cross-sectional analysis of east-west wind speed components along longitude 140°E for 1200 U.T., September 19, 1964. Equivalent blackbody temperatures (heavy line) along 140°E were derived from a digital analysis based on a 1:5 million scale grid print map from orbit 326, 1457 U.T., September 19, 1964.

Since the radiosonde humidity element is unreliable when the air temperatures are colder than -40°C, determination of cirroform clouds was made subjectively from the peaks in the HRIR data, which presumably responded to the radiant emission from high level clouds.

A detailed digital analysis of blackbody temperatures on a 1:1 million scale was made over the Kuroshio current in the region from 125°E to 130°E and 25°N to 30°N. Generally the T_{BB} values were in the 290° to 300°K range which compares well with the climatological sea temperatures of that region in September. This was in an area of scattered cumulus and altocumulus cloud reports and showed up fairly dark on the Nimbus photofacsimile picture (Figure 14).

Also appearing in Figure 14 is a diamond-shaped, intense cloud mass at 26°N and 138°E. Although there were no surface or upper air observations in the vicinity of this cloud mass to confirm severe storm activity, the cloud mass has the characteristics of the severe storm-cloud patterns discussed by Whitney (References 7, 8, and 9). These characteristics include: medium scale size; unbroken, uniform appearance, either separated or completely isolated from other cloud cover; and intense brightness. Even though the HRIR data do not delineate clouds by brightness (reflected solar radiation) but rather by temperature (emitted thermal radiation), one would expect the same result, since the clouds are associated with intense convective activity. On the one hand, the cloud mass is high, and therefore cold, to give the HRIR a photofacsimile picture the appearance of an intense cloud mass. Also, the cloud mass is thick, and therefore it reflects the solar radiation quite well to make the cloud mass appear bright in a TV picture. This is one example of the possibility of tracking severe weather systems with both HRIR and TV.

Typhoon Ruby

The most important operational benefits to be derived from weather satellites thus far probably lie in the detection of severe storms over remote areas. Many tropical storms have been initially located and identified by satellites. The Nimbus satellite is well suited in this regard, for it can detect and track storms both day and night.

Tropical Storm Ruby was initially detected at night by the Nimbus HRIR during orbit 48 at 1500 U.T., August 31, 1964, almost 21 hours before aerial reconnaissance located the storm (Reference 3 and Figure 19). The next two HRIR views of Ruby, on September 2-4, 1964, show Ruby at the edge of the photofacsimile film strip where there is great distortion but the characteristic shape is unmistakable. The depiction of Ruby on September 2 shows a good example of strong outflow from the upper levels of the storm as indicated by the cirroform cloud canopy and streamers.

The Nimbus HRIR next detected Ruby at 1600 U.T. September 5, 1964, a few hours after Ruby had passed directly over Hong Kong, becoming the first typhoon to do so in 20 years. The maximum winds in Hong Kong were estimated at 140 knots.

The HRIR depiction of Ruby on September 5 shows it after it had passed inland and had begun to weaken. The final HRIR view, at 1700 U.T. September 6, 1964, shows that Ruby had dissipated but still exhibited disorganized widespread cloudiness.

The HRIR depictions in this section were used to demonstrate the capability of the Nimbus HRIR to detect and track tropical cyclones. There is sufficient overlap between adjacent orbits such that a feature the size of a tropical storm will not go undetected, provided readout is

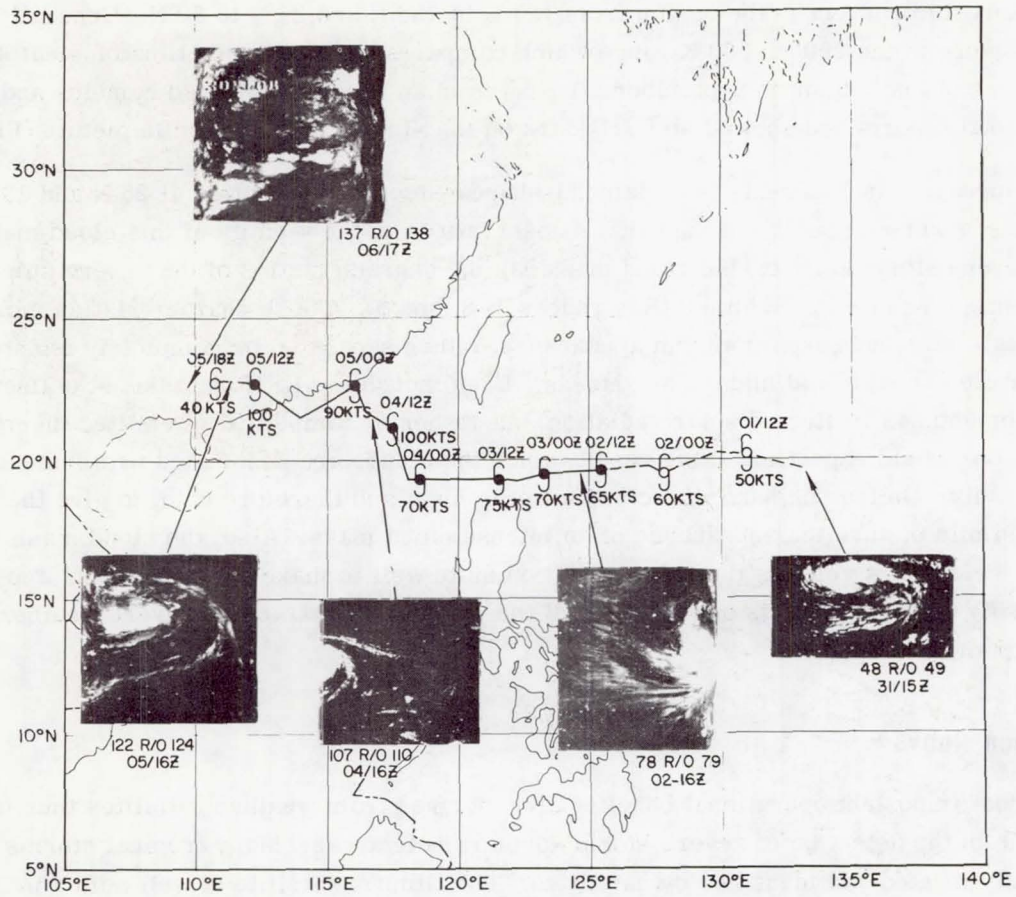

Figure 19—Track of Typhoon Ruby from August 31 to September 6, 1964 with inserts of five HRIR photofacsimile depictions of Ruby in the Western Pacific Ocean.

achieved. The Nimbus I HRIR system did not operate continuously but was programmed off periodically for engineering purposes. As a result, the HRIR system was not operating before August 31 or on September 1 and 3, 1964, when the satellite passed over Typhoon Ruby. Otherwise, the storm would have been detected earlier and tracked continuously until its dissipation.

Siberian Frontal System

An interesting example of large mesoscale synoptic weather systems is shown in Figure 20. The gridded photofacsimile picture contains three consecutive Nimbus orbits during which, three extra-tropical vortices and frontal zones, in various stages of development, were observed by the HRIR.

The northernmost occlusion extends well into the polar regions (80°N) while the other vortices lying along 55°N to 65°N are connected by an elongated polar frontal system from

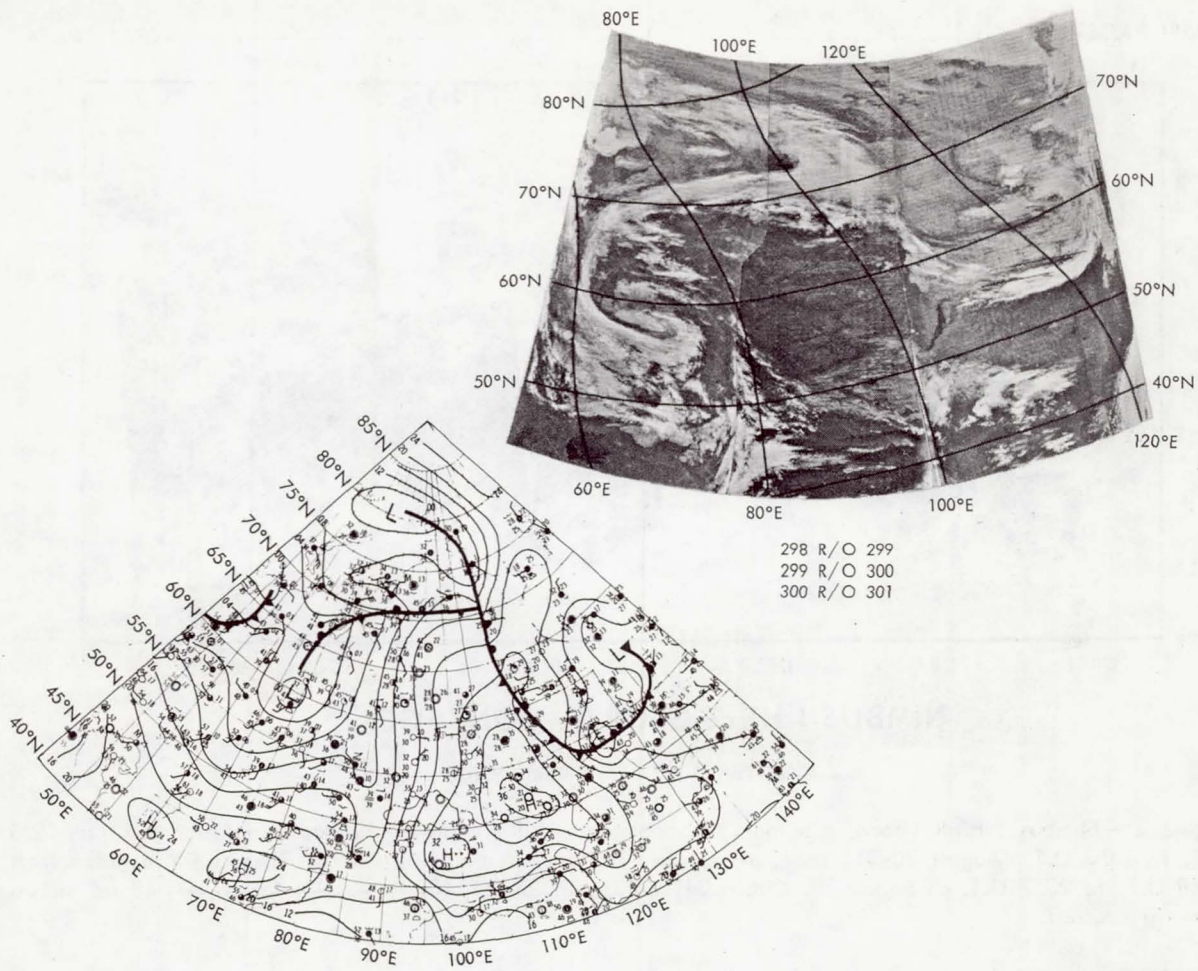

Figure 20—An extensive frontal system over Central Asia: (a) surface synoptic chart for 0000 U.T., on September 18, 1964, (b) composite of HRIR photofacsimile depictions for three adjacent orbits 298, 299, and 300 from approximately 1700 to 2000 U.T., on September 17, 1964.

central Russia to eastern Siberia. The Aral Sea is clearly visible at 45°N, 60°E. The 0000 U.T., September 18, 1964 synoptic weather analysis was provided by the National Meteorological Center, U. S. Weather Bureau, Washington, D. C.

Global Montage and Southern Hemisphere Analysis

Figure 21 is a global montage of fourteen Nimbus I HRIR orbits recorded within a 24 hour period (August 30-31, 1964), with the exception of two photofacsimile strips labelled minus 24 hours. The gaps in the HRIR coverage are largely due to the ellipticity of the satellite's orbit, resulting in the reduced read out times over the Rosman, North Carolina and Gilmore Creek, Alaska acquisition stations. The variable curvature of the meridians is due to distortions near the edges of the film strips.

There are several characteristic synoptic weather features present in this global picture. The Intertropical Zone of Convergence (ITC) is shown as a thin cloud band in the Eastern

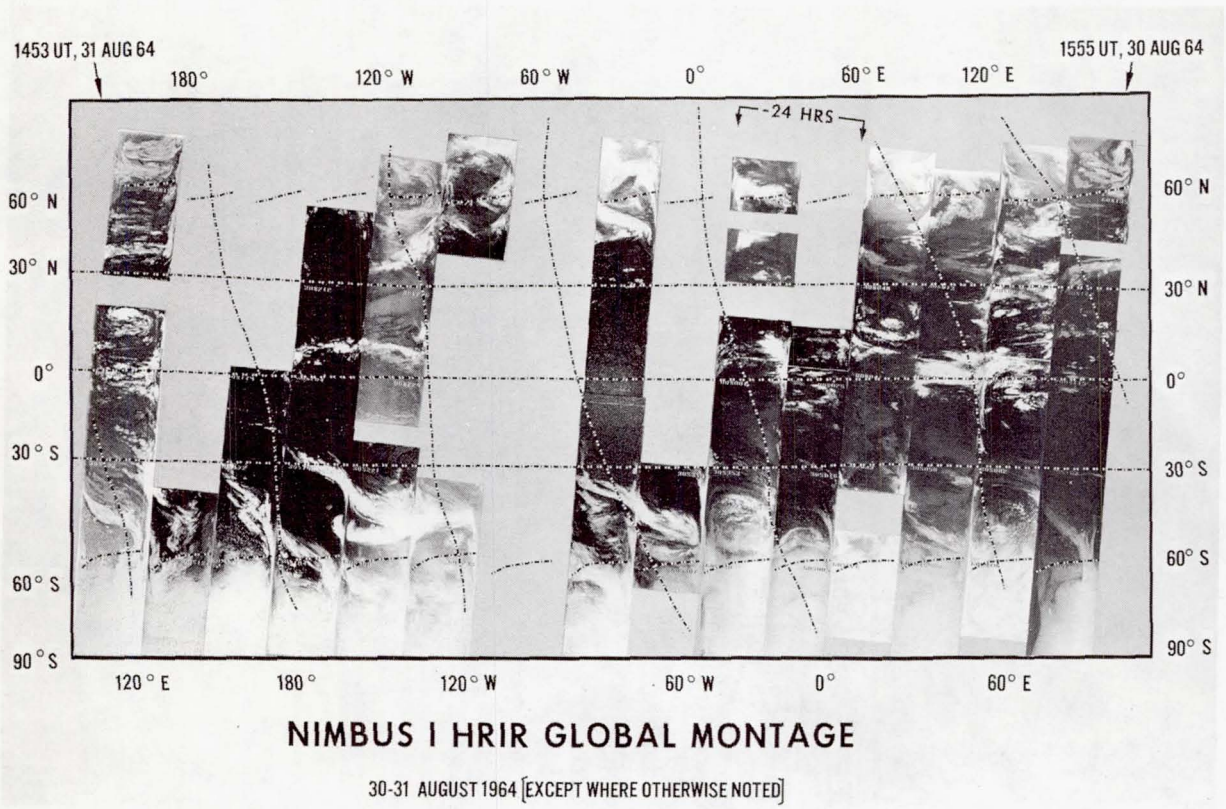

Figure 21—Nimbus I HRIR Global Montage. Composite of HRIR photofacsimile depictions recorded from 1555 U.T. to 1453 U.T., August 30-31, 1964, except two orbits labeled minus 24 hours. These were recorded from 2148 U.T. to 2357 U.T. on August 29. Orbits 34, 35, 36, 37, 23, 24, 40, 41, 43, 44, 45, 46, 47, 48 are shown from right to left.

Pacific Ocean while the equatorial region through the Indian Ocean contains a broad chaotic cloudy region. In the mid-latitudes in both hemispheres, networks of cloudy frontal zones are shown. It must be noted that the HRIR photofacsimile strips begin to overlap strongly beyond 60° latitude so that in this montage, the edge of a front in one HRIR strip tends to be repeated in the next consecutive orbit. No attempt was made to crop the data to remove this overlapping effect.

For an analysis near the poles, a polar stereographic presentation of HRIR data is more suitable. Figure 22 shows photofacsimile strips of orbits 40 and 51 for August 31, 1964, with the exception that two earlier orbits 23 and 24 on August 29, 1964 were added for completeness. In this case, the overlapping cloud data were carefully matched as the orbital strips were arranged radially about the South Pole.

Oliver has discussed the fact that there is a definite lack of warm frontal cloudiness in the HRIR observations in the Southern Hemisphere (Reference 10, Figure 21). Because of the lack of strong vertical motion and air mass discontinuity between the essentially warm and cool sectors of Southern Hemisphere extratropical cyclones, extensive warm-frontal cloudiness seem to appear less frequently, except in the vicinity of well developed vorticity centers.

In this presentation, one can better appreciate the intense weather activity along the circumpolar frontal zone. Far reaching frontal systems are shown extending 30° to 45° from the

0200 Z TO 2000 Z
31 AUG 1964

2200 Z TO 2330 Z
29 AUG 1964

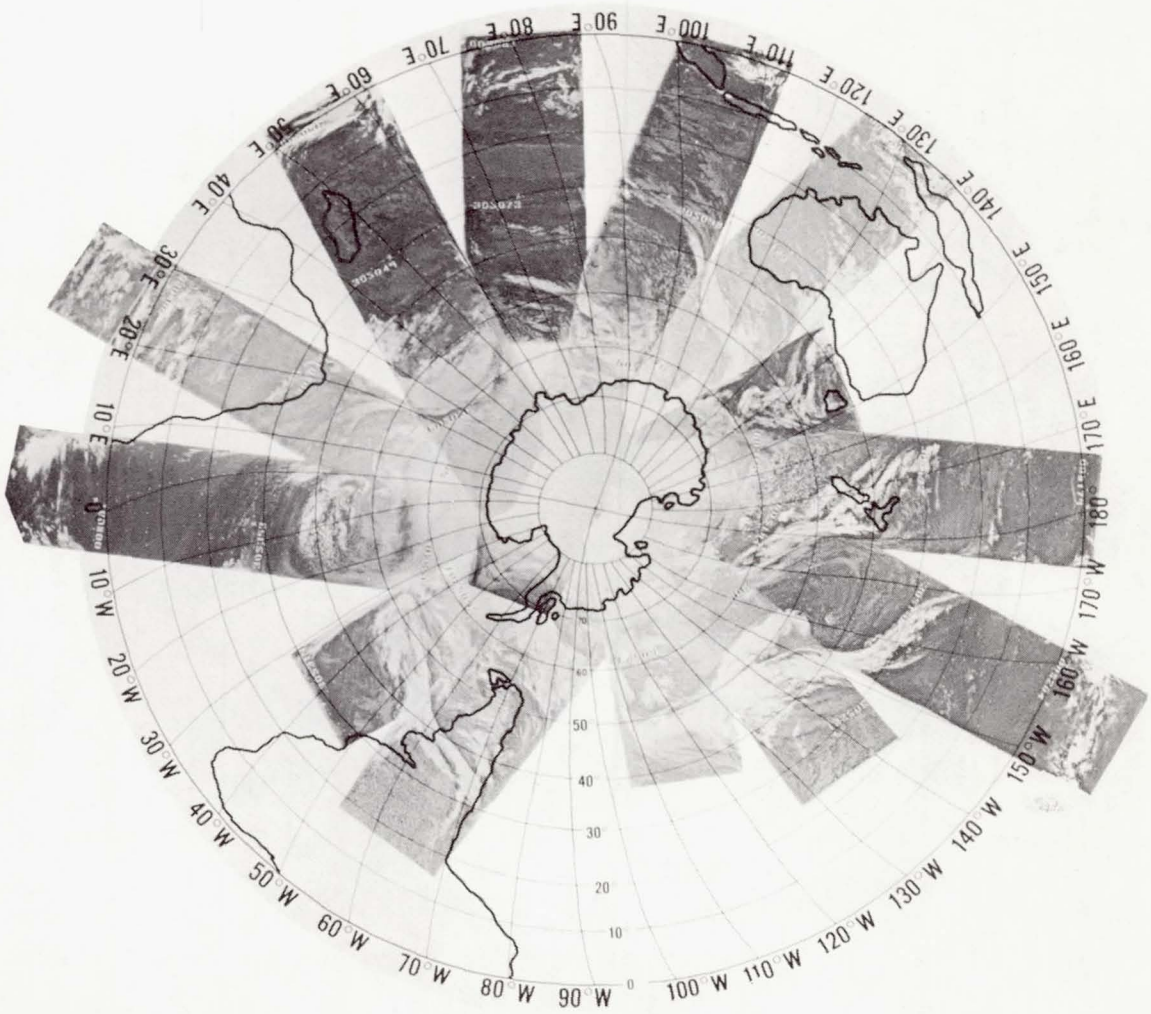

Figure 22—Polar stereographic presentation of Nimbus HRIR photofacsimile depictions for the Southern Hemisphere. Orbits 40 through 51 on August 31, 1964 and orbits 23 and 24 on August 29, 1964 are shown.

Antarctic ice shelf almost to the subtropics. The figure probably represents the most detailed three-dimensional cloud cover presentation ever shown over the Southern Hemisphere on a given day.

A revised 1000 mb chart for 1200 U.T., August 31, 1964 (Figure 23) was drawn subjectively from the air mass and frontal cloudiness shown by the Nimbus photofacsimile strips (Figure 22). This chart was then fitted to conform to the ridges and troughs of the 1200 U.T., 1000 mb and 0000 U.T., 500 mb charts for August 31, 1964 (Figures 24 and 25) drawn by the International Antarctic Analysis Center, Melbourne, Australia. Coded South African, Australian, New Zealand and South American synoptic data were also used.

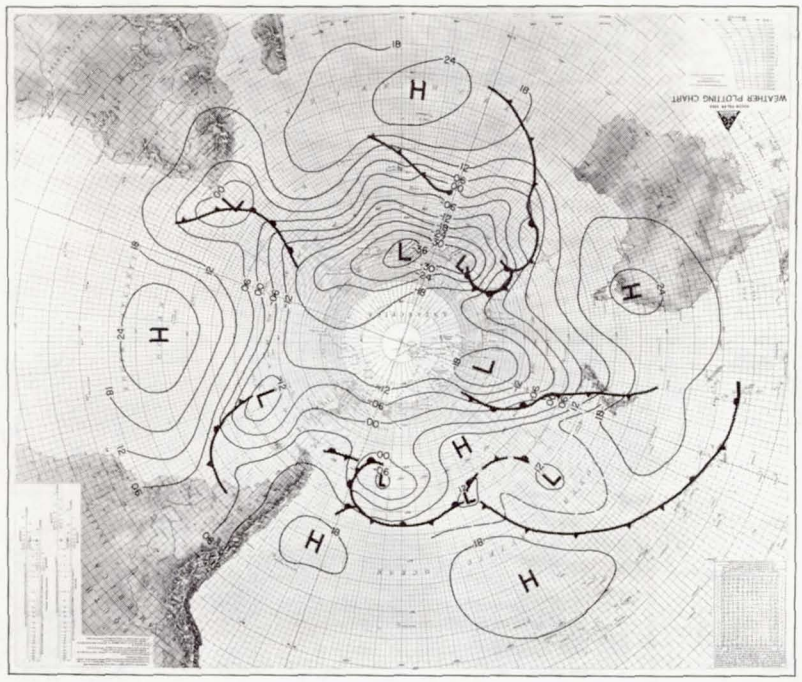

Figure 23—1000 mb analysis for the Southern Hemisphere for 1200 U.T. on August 31, 1964, based on conventional weather data and Nimbus I HRIR data, shown in Figure 22. Contours were drawn at 60 meter intervals.

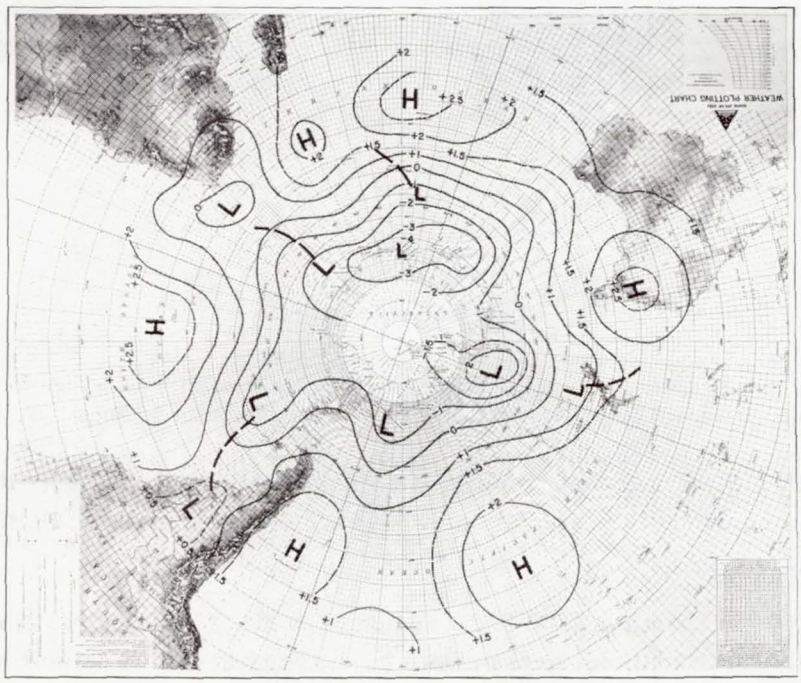

Figure 24—1000 mb analysis for the Southern Hemisphere at 1200 U.T., August 31, 1964, drawn by the International Antarctic Analysis Center, Melborne, Australia, using only conventional data. Contours were drawn at 100 meter intervals.

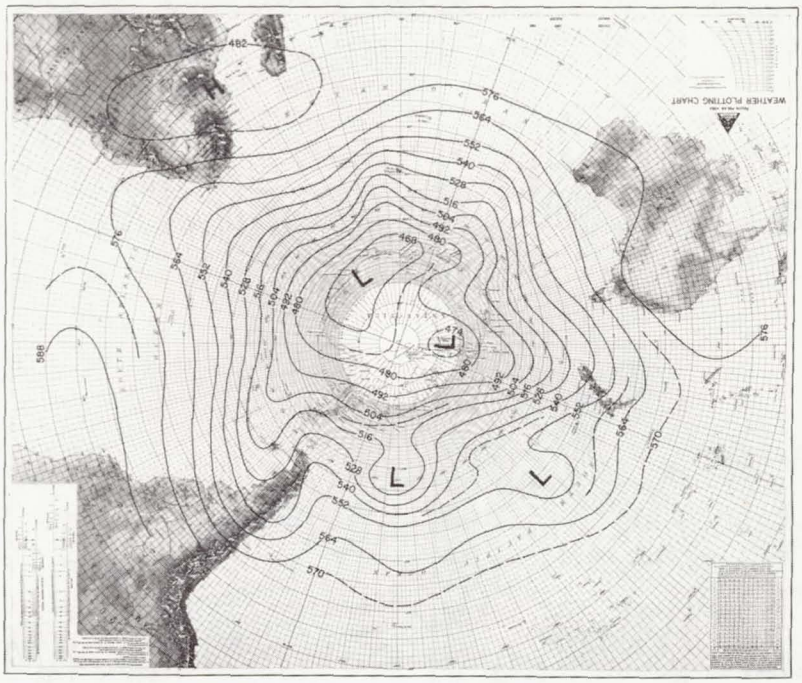

Figure 25—500 mb analysis for the Southern Hemisphere based on conventional weather data at 0000 U.T., August 31, 1964. Contours were drawn at 120 meter intervals.

Mesoscale Features

The discussion thus far has centered around some of the large scale meteorological systems depicted by the HRIR data. Such large scale features as Hurricane Dora, polar frontal systems and Indian Ocean convergence zone cloudiness have been discussed in some detail. The horizontal resolution of both the HRIR and AVCS subsystems allows the observation of much smaller scale phenomena that are normally not detected from the network of conventional meteorological observations. Three mesoscale features will be discussed in the following section.

Sierra Lee Wave

Figure 26a shows a section of a HRIR photofacsimile film strip which was acquired at approximately 0759 U.T. on August 31, 1964 when Nimbus I passed over the west coast of the United States on orbit 044. A broad shield of very high clouds is seen extending from near the center left to the upper right of the film. Between 38°N and 39°N, and 121°W and 123°W, this shield of clouds is broken up into a series of lee mountain wave clouds on the lee side of the Sierra Nevada mountain range. An examination of conventional meteorological data showed that the classical prerequisites for the formation of mountain lee waves existed at this time (References 11 and 12). Superimposed on the film strip in Figure 26a are arrows showing the wind direction, the location of the maximum wind speed, and the 50 knot isotach of the 500 mb level wind. These 500 mb wind data were taken from the 1200 U.T., August 31, 1964 chart, a section of which is shown in Figure 26b. The Oakland, California raob showed that the wind

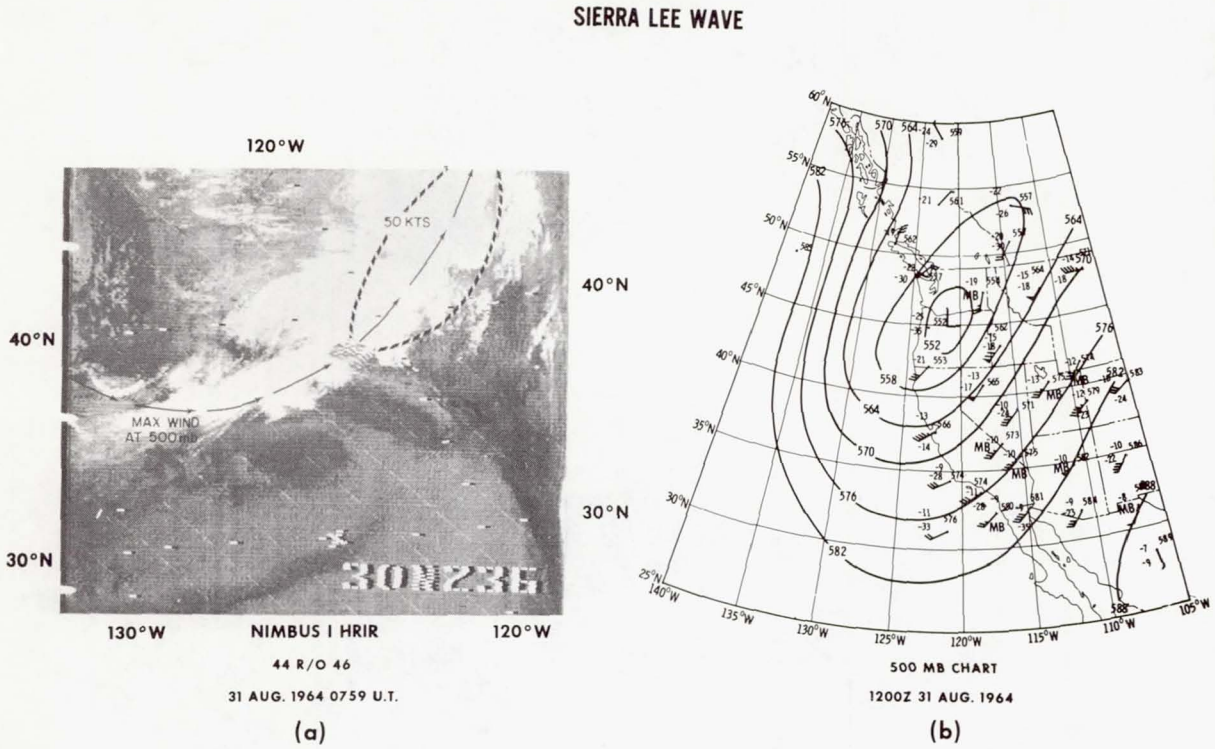

Figure 26—An HRIR view of mountain lee waves: (a) HRIR photofacsimile depiction over California of orbit 44 at 0759 U.T., August 31, 1964. Sierra lee wave clouds shown near 38°N, 121°W (239°E) with streamline of maximum wind speed at 500 mb superimposed, (b) 500 mb chart of western United States for 1200 U.T., August 31, 1964.

direction was essentially constant from the surface to the tropopause height of 53,000 ft and normal to the mountain range. The wind speed increased from 15 knots at 1,000 ft to a maximum of 84 knots at 37,000 ft with a 24 knot wind at 12,000 ft near mountain top height. The Oakland raob also showed a temperature increase of nearly 3°K from 3,000 ft to 6,500 ft. Thus the three basic meteorological conditions for the existence of lee waves are present: the wind direction is normal to the mountain range and changes little in direction from the top of the range to the tropopause, vertical wind shear is large through the level of the range and for several thousand feet above, and a temperature inversion exists at the mountain top on the upwind side (Reference 12). The importance of the HRIR data to reveal the existence of lee waves and the associated turbulence, especially in remote areas, at night, and when lower-level clouds obscure the wave clouds, need not be emphasized here, since it is well known that the safety and comfort of air travel depends heavily on avoiding these regions of mountain lee waves.

Guadalupe Vortices

The Advanced Vidicon Camera System (AVCS), which has a spatial resolution of the order of one kilometer, has provided pictures showing many mesoscale atmospheric phenomena. We will not try to include all of these mesoscale features seen in the AVCS pictures, but will show two examples of very interesting features to demonstrate the system's capabilities.

One of these examples is seen in Figure 27, showing eddy patterns in the clouds down wind from Guadaloupe Island, off the coast of Baja, California. This picture was taken at 1851 U.T. on September 13, 1964. This type of cloud eddy has been recorded on a number of occasions by satellite photography (References 13, 14, 15 and 16). The pattern downstream from the island has the appearance of vortices being alternately formed from either side of the island. The nearest raob, at San Diego, California, showed a very strong inversion with a base at 650 meters and a temperature increase of 9°K in the next 500 meters. The surface wind at Guadalupe Island was northerly at 14 knots. On the next day, September 14, 1964, the wind speed dropped to 10 knots and the vortices became larger and arranged in a single row as seen in Figure 28. Three vortices are present and become progressively weaker downstream. While the observational network is perhaps too sparse to explain the flow patterns depicted by these clouds, the clarity and high resolution of the AVCS suggest applications in detailed aerodynamics of the atmosphere.

Antinoform Clouds

An example of mesoscale features in the AVCS pictures is shown in Figure 29. This set of four pictures was taken at approximately 1813 U.T., on September 15, 1964, when Nimbus I passed over the South Pacific during orbit 269. The clouds in these pictures have been called actinoform clouds; and, as the name suggests, they are arranged in a spine-like structure with the rays converging to either a common line or point. Little is known about these low-level clouds other than that they have only been observed at low latitudes under a strong low-level inversion (Reference 17).

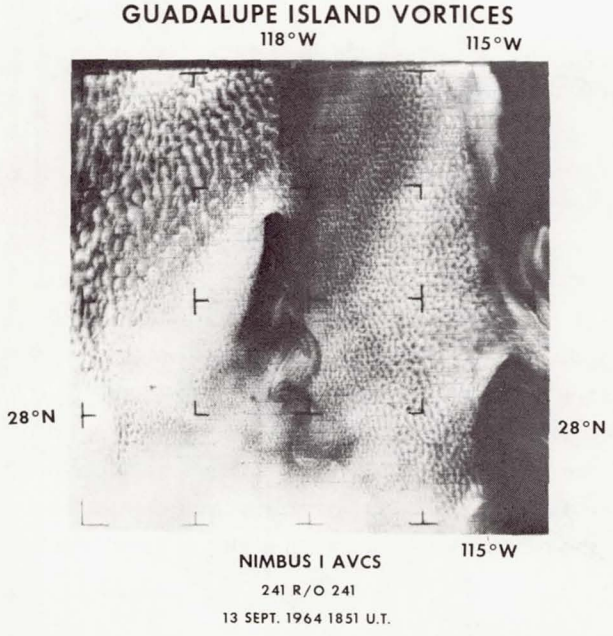

Figure 27—AVCS photograph of Guadalupe Island showing cloud wake formation downstream from the island. Guadalupe is located near the tip of the V-shaped wake. Orbit 241 at 1861 U.T., September 13, 1964.

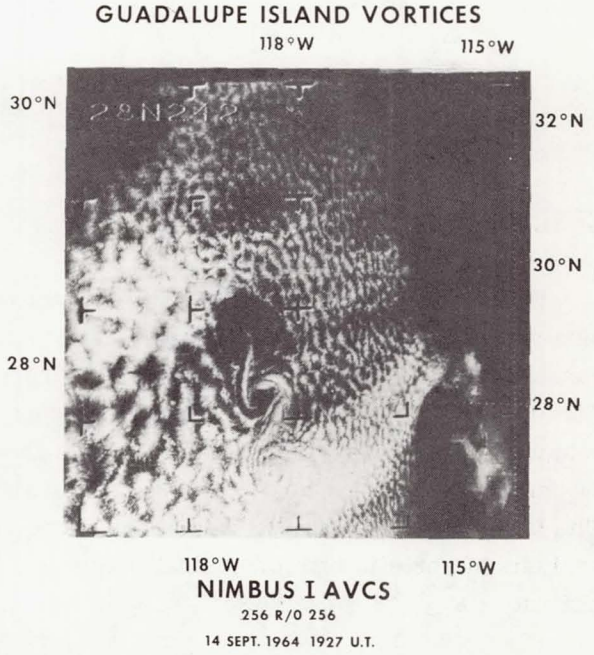

Figure 28—AVCS photograph near Guadalupe Island showing tail of vortices downstream from the island. Orbit 256 at 1927 U.T., September 14, 1964.

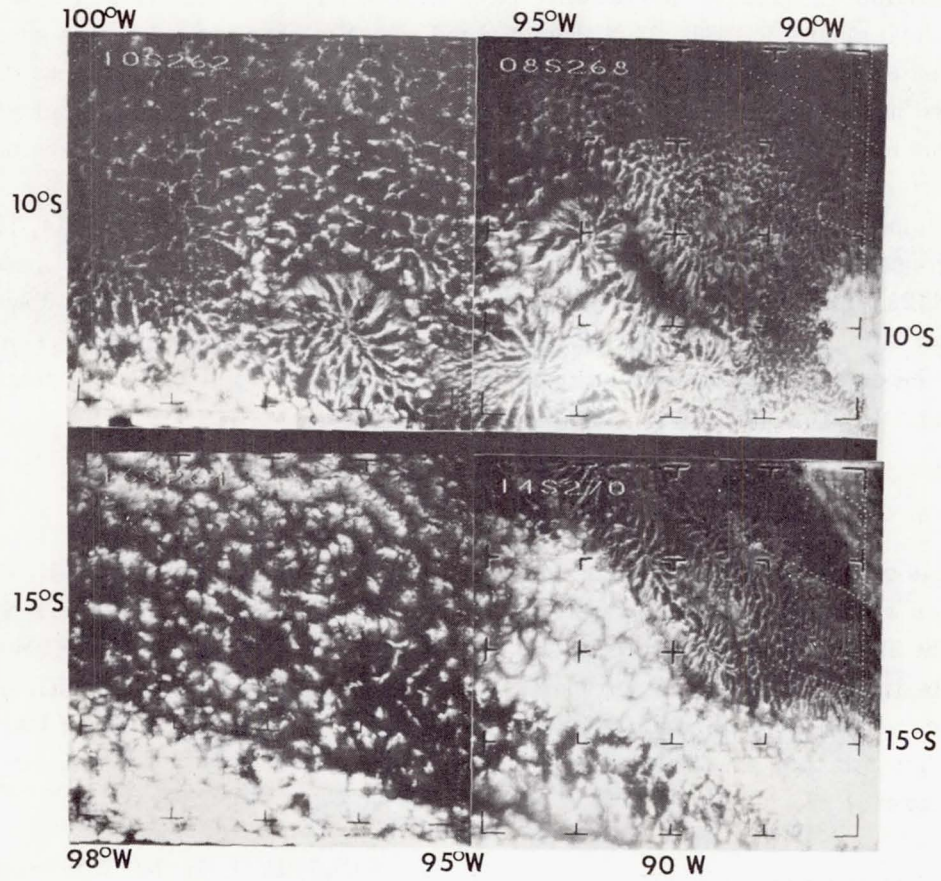

Figure 29—AVCS photograph of Eastern Pacific Ocean off the coast of Peru. Actinoform clouds are shown in northeast half of photograph. Orbit 269 at 1813 U.T., September 15, 1964.

CONCLUSIONS

During the lifetime of the Nimbus I satellite, approximately 6200 minutes of radiometric data were recorded between August 28 and September 22, 1964. The HRIR experiment proved capable of providing detailed cloud information in both the horizontal and vertical dimension. The broad areal radiation coverage made possible the study of atmospheric disturbances ranging from mesoscale to planetary scale in all climatic regions, and the use of photofacsimile techniques to depict synoptic information in real time is well suited for operational applications. The fact that numerical T_{BB} values are associated with the HRIR data, permits the quantitative analysis of specific meteorological features, e.g., the amount of cloudiness above a specified altitude.

A satellite in a circular orbit must perforce spend half of its life over the dark side of the earth; therefore, the use of the HRIR in conjunction with television systems essentially doubles the usefulness of a meteorological satellite which carries only television systems. The utilization of the HRIR, as well as enhancement of the television data was largely dependent on the

three-axis earth orientation of the Nimbus I satellite which was successfully achieved during the active lifetime of the spacecraft.

ACKNOWLEDGEMENTS

The authors are grateful to Messrs. V. J. Oliver and R. K. Anderson of the Meteorological Satellite Laboratory, U. S. Weather Bureau, for preparing the Southern Hemisphere mosaic and associated synoptic charts. Mr. Carl O. Erickson, U.S.W.B., provided thoughtful advice on photointerpretation of Nimbus HRIR products, and J. C. Sadler, Lt. Col., USAF, enlightened the authors on modern developments in tropical meteorology which were interpreted in this study.

The authors wish to thank Mr. Wm. R. Bandeen, Goddard Space Flight Center, for reviewing the manuscript and providing helpful comments and suggestions.

REFERENCES

1. Bandeen, W. R., Kunde, V., Nordberg, W., and Thompson, H. P., "TIROS III Meteorological Satellite Radiation Observation of a Tropical Hurricane," *Tellus* 16(4):481-502, November 1964.

2. Allison, L. J., Gray, T. I., and Warnecke, G., "A Quasi-Global Presentation of TIROS III Radiation Data," NASA Special Publication No. 53, 1964

3. Cry, G. W., "North Atlantic Tropical Cyclones, 1964, " *Mariners Weather Log* 9(1):1-9, Washington, D. C.: U. S. Weather Bureau, January 1965.

4. Riehl, H., "On the Origin and Possible Modification of Hurricanes," *Science* 141(3585):1001-1010, September 1963.

5. Yanai, M., "Formation of Tropical Cyclones," *Rev. Geophys.* 2(2):367-414, May 1964.

6. U. S. Weather Bureau. "Daily Series, Northern Hemisphere, Sea Level, 500 Millibar Charts with Data Tabulation," July 1938 (Continuing Series).

7. Whitney, L. F., Jr., and Fritz, S., "A Tornado-Producing Cloud Pattern Seen from TIROS I," *Amer. Meteor. Soc. Bull.* 42(9):603-614, September 1961.

8. Whitney, L. F., Jr., "Another View from TIROS I of a Severe Weather Situation," *Mont. Weath. Rev.* 89(11):447-460, November 1961.

9. Whitney, L. F., Jr., "Severe Storm Clouds as Seen from TIROS," *J. App. Meteor.* 2(4):501-507, August 1963.

10. Fugita, T., "Mesometeorological Interpretation of Satellite Data Text for Sessions N-Q," Proceedings of the Interregional World Meteorological Organization. Seminar on Interpretation and use of Meteorological Satellite Data, Tokyo, Japan, 1964.

11. Scorer, R. S., "Lee Waves in the Atmosphere," *Sci. Amer.* 204(3):124-134, March 1961.

12. "An Introduction to Atmospheric Turbulence," Norfolk, Virginia: U. S. Navy Weather Research Facility, U. S. Naval Air Station, Navaer 50-IP-546, May 1958.

13. Copra, K. P., and Hubert, L. F., "Karman Vortex-Streets in Earth's Atmosphere," *Nature,* 203(4952):1341-1343, September 1964.

14. Hubert, L. F., "Picture of the Month," *Month. Weath. Rev.* 91(10/12):633-634, October-December 1963.

15. Hubert, L. F., and Krueger, A. F., "Satellite Pictures of Mesoscale Eddies," *Month. Weath. Rev.* 90(11):457-463, November 1962.

16. Alaka, M. A., "The Occurrence of Anamalous Winds and Their Significance," *Month. Weath. Rev.* 89(11):482-494, November 1961.

17. Singer, F. S., "Introduction to the Picture of the Month Series," *Month. Weath. Rev.* 91(1): 1-2, January 1963.

NASA-Langley, 1965